2006

Development of corrugated thin metal structures for a MEMS-based fiber optic aligner

Jason Todd Iceman
Lehigh University

Iceman, Jason Todd

Development of Corrugated Thin Metal Structures for a MEMS-based Fiber Optic Aligner

May 2006

Development of Corrugated Thin Metal Structures for a MEMS-based Fiber Optic Aligner

Jason Todd Iceman

Presented to the Graduate and Research Committee

of Lehigh University

in fulfillment of the

thesis requirement for the degree of

Master of Science

in

Materials Science and Engineering

Lehigh University

April 28th, 2006

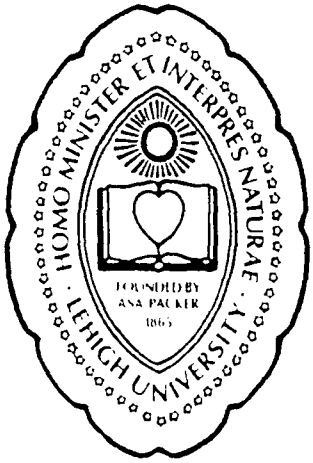

This thesis is accepted and approved in partial fulfillment of the requirements for the Master of Science.

April 26, 2006

Date

Raymond A. Pearson, Ph.D.

Thesis Advisor

Richard P. Vinci, Ph.D.

Co-Advisor

G. Slade Cargill, Ph.D.

Chair, Materials Science and Engineering

Acknowledgements

I am indebted to Professor Ray Pearson for allowing me the opportunity to work on this project. Several other faculty and staff have been a part of the research team investigating the fiberoptic aligner. Their help has been invaluable. Professors Rick Vinci, Svetlana Tatic-Lucic and Walter Brown have provided guidance and constructive advice throughout the course of this work. Seungmin Hyun and Weisong Wang provided assistance with SEM imagery and modeling. Mehmet Sahin, Murat Ozturk and Professor Herman Nied developed the closed form solution for the bucking of a corrugated thin film structure. Mike Rogosky and John McIntosh at the Penn State University Nanofab were instrumental in the development of the grayscale lithography work described in this thesis. Dr. Amir A. Saghiri of Heideberg Instuments provided greyscale lithography samples and development time to this project.

On a more personal note, I would also like to thank W. Jeffrey Shakespeare, Ph.D. for his unflagging support and enthusiasm without which I would not have had the courage to begin the journey toward an advanced degree. My spouse, Lena Marie Iceman, and children Benjamin Ryan Iceman and Sarah Elizabeth Iceman gave willingly of their time and love throughout the research and writing required to complete this thesis.

Table of Contents

List of Tables

List of Figures

Abstract

Aligning a fiber (or lens) to a waveguide of a laser or photodiode die is one of the most time- and yield-consuming steps in optoelectronic packaging. Alignment processes traditionally require three elements: expensive capital equipment, a skilled technical staff and significant factory floorspace. With advances in MEMS technology, it is possible to miniaturize the aligner and place it inside of the optoelectronic package as a component, affording the ability to align "on the fly", as well as significantly reducing the development cycle time and cost of optoelectronic packages. This investigation characterizes the behavior of a prototype MEMS aligner, and then suggests ways to push the technology forward to reduce the cost of the device, simplify the manufacturing process and increase functionality.

Considerable attention is given to methods of fabricating and testing corrugated thin film structures. These structures show the potential to replace LIGA structures in applications requiring mechanical rigidity without the hinderances of expensive mask sets and limited access to fabrication tools. Methods to fabricate and test structures with section stiffness in the range 1×10^{-20} m^4 are described in detail. Greyscale exposure of a thick layer of photoresist yielded structures much more uniform than those achieved by mechanical embossing. Grayscale structures achieved a maximum feature depth of 26um, as compared to 16um for parts fabricated by mechanical embossing.

Chapter 1

Introduction

1.1 Purpose of study

This work details the reverse engineering and continued development of a MEMS device used to align an optical fiber to a laser diode. The Boeing Corporation (St. Louis, Mo.) donated the intellectual property and patent rights for this MEMS device to Lehigh University. Several working devices accompanied this donation as well, but the full set of information required to replicate the devices did not. The objective of this work is to determine the detailed processing steps and performance characteristics of the existing device, and then to improve the design by adding functionality and reducing the cost of fabrication. One method of cost reduction is explored in detail: replacing the LIGA structures in the existing device with corrugated thin film structures.

A MEMS-based fiber aligner is a novel approach to active fiber alignment. Our device is based on a silicon platform that can leverage the vast array of well-developed silicon processing tools. As a packaging material, silicon has been widely used in optoelectronics for many years. Silicon substrates with v-grooves have been used to passively align fibers to laser die. This passive alignment requires a large, expensive die bonder capable of aligning the waveguide of a die to submicron tolerances. Traditionally, active alignment also requires a large amount of both floorspace and capital. As an example, the Newport Corp. (Irvine, CA) offers turnkey alignment and

laserweld systems for several hundred thousand dollars. Developing and characterizing the laser welding process is time consuming and expensive; skilled operators are required, and hundreds of devices are needed to characterize the process to the point where yield and cycle times are optimized. In single-mode devices, a one-micron shift of the lens or fiber during the welding process can cause significant coupling loss. It is possible to attempt to "hammer" the fiber back into position. This process is more art than science and requires the time and attention of skilled engineers. Beyond hammering, the options for recovering power lost during welding are grim. Reworking a device by removing the lens and re-welding is nearly impossible without damaging the optical chip.

The MEMS-based fiber aligner solves many of these problems. It is small enough to be used as a component inside the optoelectronic package. It can be fabricated using standard MEMS processes. It affords the ability to align easily and repeatedly. This technology has the potential to dramatically reduce the difficulties of fiber to waveguide alignment, significantly reducing development time and cost.

1.2 Target Problem Description

To date, MEMS technology has been used in several attempts to create a device capable of replicating the alignments achieved with macro scale tools. A thorough investigation of the background literature shows that the In Package Micro Aligner (IPMA, henceforth) developed by the Boeing Corporation has achieved the widest range

of motion in X, Y and Z of all devices attempted to date. This device uses embedded heaters to cause a thermal expansion of thick metal structures to achieve a wide range of motion and high alignment forces, but even this device has limitations.

The first limitation is driven by the choice of the specific MEMS technology used in the device. The LIGA process used to create the mechanical structures on the die is both costly and of limited accessibility; mask sets can cost upwards of $10k and there are but three locations in the United States which have access to a synchrotron x-ray radiation source required by this technology. There is significant value in developing an alternative method for `achieving metal MEMS structures that exhibit all of the stiffness of LIGA structures, but with lower barriers to implementation.

1.3 The Solution

With the long-term goal of creating an improved device in mind, the work has been divided into three portions. First, the tasks of measuring the dimensions of the existing devices, creating CAD data for masks, and development of process instructions were contracted out to the MEMS and Nanotechnology Exchange (Reston, VA). Second, force and displacement characterization of the existing devices was performed at Lehigh University. These data were compared to an ANSYS (Canonsburg, PA) Finite Element Analysis (FEA) model to develop a fundamental understanding of the mechanics involved in the operation of the actuators. Finally, the team at Lehigh has developed

several concepts to refine the design. In this document, a particular emphasis is placed on replacing the potential to replace LIGA elements with thin film structures.

1.4 Overview of the Thesis

A significant amount of background research is required to understand how MEMS technology has been used to aid fiberoptic alignment, and provide a context for understanding the workings and capabilities of the Boeing IPMA device. Included in this work is a survey of the literature related to MEMS and optical alignment.

With the overview of MEMS optical alignment technologies complete, the road is paved to understand the inner workings of the IPMA device. This will include detailed operation sequences, fabrication steps, as well as force and displacement data. A careful analysis will yield areas where the IPMA device can be improved.

An effort to develop and fabricate low cost mechanical elements as replacements for LIGA structures will be reviewed in some detail and the results of stiffness testing will be discussed.

Chapter 2
Background

2.1 Electrical versus optical interconnects

The year 2006 marks the 300th birthday of Benjamin Franklin, who left us quite a fine legacy. Good Dr. Franklin was famous during his own time as a visionary statesman and a prolific inventor. His most fundamental discovery, electricity, has revolutionized the entire globe, promoting commerce and raising the quality of life for all of humanity.[1]

In most of the civilized world access to electricity is taken for granted. We wake to electric alarm clocks, cook our food on electric ranges and use electric lights to illuminate the dark. Billions of dollars have been spent developing the electricity infrastructure. Electrical interconnects have been engineered to a degree where simple connections are absurdly straightforward and complex high speed / high density interconnects can be made at a staggering rate.

We connect our tools and appliances to the electric grid with ease. No special skills or instructions are required, just an available wall plug. The processors inside personal computers require thousands of electrical connections. The ultimate dense electrical interconnect is represented by high speed wirebonding machines capable of making sixty thousands of electric connections per hour on a pitch of 35 microns[2]. Such a machine is shown in Figure 1.

Figure 1 - A wirebonding machine making high density interconnects[3]

Optical interconnects are not as refined as electrical interconnects. Such interconnects are a bit more finicky and require a higher level of care and attention to ensure a good connection than their electrical cousins. Consider the polished endface connectors that are commonly used to connect one glass fiber to another. Endface connectors are not easy to use; they require careful cleaning and handling to ensure a minimum of optical power loss. These are not significant barriers for scientific or industrial use, but the speed at which an interconnect can be made is slow when compared to electrical interconnects. As one potential solution discrete connectors between glass fibers can be eliminated using splicing equipment. The connection is intended to be permanent; akin to soldering together two copper wires. Unfortunately, fiber splicing equipment is expensive and requires considerable training and practice

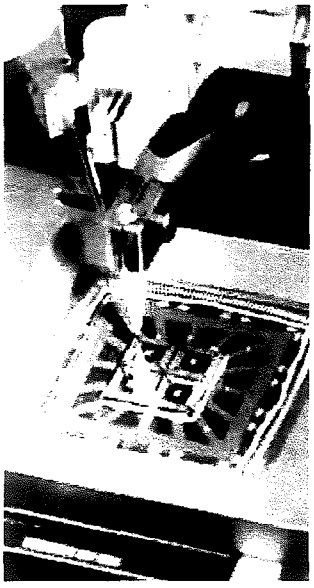

Figure 1 - A wirebonding machine making high density interconnects[3]

Optical interconnects are not as refined as electrical interconnects. Such interconnects are a bit more finicky and require a higher level of care and attention to ensure a good connection than their electrical cousins. Consider the polished endface connectors that are commonly used to connect one glass fiber to another. Endface connectors are not easy to use; they require careful cleaning and handling to ensure a minimum of optical power loss. These are not significant barriers for scientific or industrial use, but the speed at which an interconnect can be made is slow when compared to electrical interconnects. As one potential solution discrete connectors between glass fibers can be eliminated using splicing equipment. The connection is intended to be permanent; akin to soldering together two copper wires. Unfortunately, fiber splicing equipment is expensive and requires considerable training and practice

before it can be used successfully, far different than the ubiquitous soldering iron and tin lead solder used to make an untold number of electrical connections.

2.2 Macroscopic Alignment Technologies

Free space optical connections between flat cleaved fibers are commonly achieved by fixing one fiber to a stationary platform and attaching the other to a platform capable of motion in the X, Y and Z axes. Optical convention holds that the Z axis is oriented along the axis of the light beam, the X axis points in the horizontal direction normal to the path of the light and the Y axis points in a direction perpendicular to both the X and Z axes. The figure below from the seminal work on optical alignment by Joyce and DeLoach[4] illustrates the alignment of two optical waveguides.

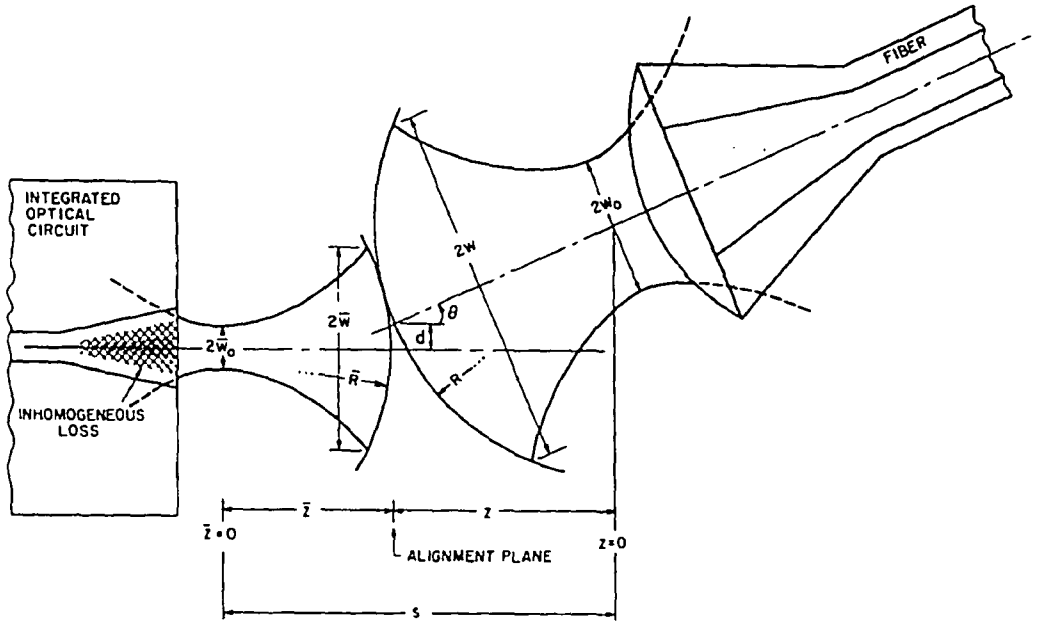

Figure 2 - Alignment of two optical waveguides[4]

Optically joining two flat cleaved fibers requires tight tolerances to minimize optical power loss. SMF-28 is a single-mode 5um core fiber manufactured by Corning, and is common in telecommunication applications. Firsthand experience in the lab aligning two such fibers yielded a tolerance of less than 0.5 microns in the X and Y directions to maintain a power loss of less than 0.5 dB. The Z axis is a bit more forgiving due to the length of the beam waist. If alignment in the X and Y directions is maintained, then a tolerance of 2um in the Z direction will hold power loss to 0.5 dB or less.

In general, connections between optoelectronic components and light carrying fiber are obtained by carefully aligning the fiber to the waveguide of the component and then fixing the fiber in place.

The physical design of optoelectronic packages in a large way revolves around creating stable optical coupling between the die and the fiber. One example of an optoelectronic package is shown in Figure 3.

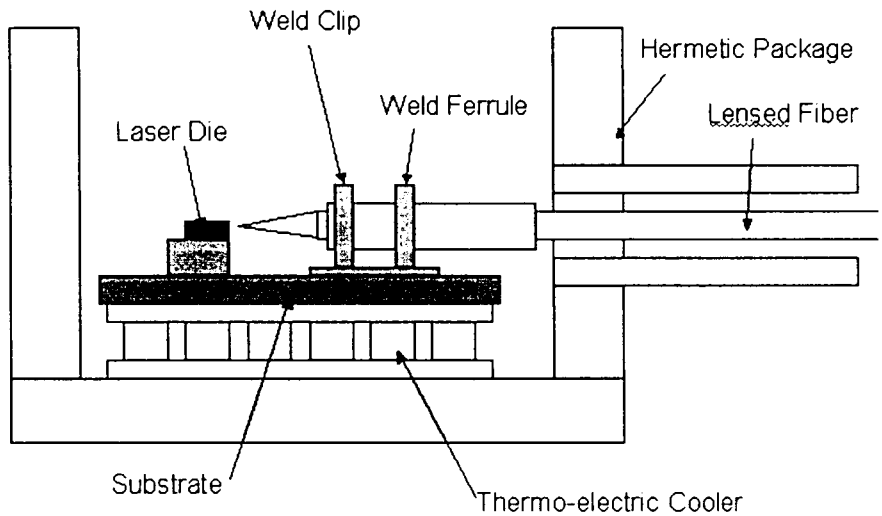

Figure 3 - Cross section of conceptual optoelectronic transmitter package

Laser welding is one common method of fixing the fiber in place. In this particular figure a lensed optical fiber is fed through the sidewall of a hermetic package and aligned in X, Y and Z to a cone of light emanating from a laser die. Laserwelding is just one of many alignment solutions in use today – it is generally regarded as the most reliable. It is this type of alignment and fixing mechanism that is used to join communication modules that are deployed at the bottom of the Atlantic Ocean, where serviceability is virtually impossible. Solder and epoxy alignment solutions have also been deployed in optoelectronics, but to a lesser extent, and primarily where reliability is

of secondary concern to manufacturing cost, such as the intra-office and datacomm markets.

The alignment tolerances involved in fiberoptic waveguide alignment are not easy to achieve. Peters and Fischer[5] report that for a lensed fiber an in-the-optical plane tolerance of 2um is required to hold 0.5db of peak power. These tolerances are on the forgiving side for optical alignment. The location requirements for a flat cleaved fiber or lensed system can be even tighter. Figure 4 and Figure 5 below show an optical fiber with a lens polished on the endface and the associated alignment tolerances, respectively.

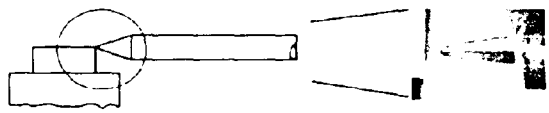

Figure 4 - A lensed fiber[5]

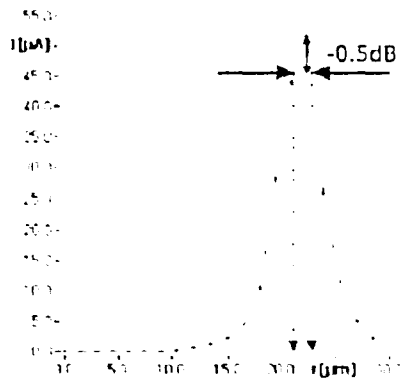

Figure 5 - Power loss due to misalignment[5]

He and Juan[6] report that a microlens can be used to significantly loosen the lateral tolerances to +/- 3um from 1um for a butt joint, but at the expense of the angular misalignment which decreases from more than 2 degrees for a 1db loss of power to less than 1 degree. Figure 6 illustrates the microlens aligned to an optical fiber, and Figure 7 and Figure 8 show the associated tolerances.

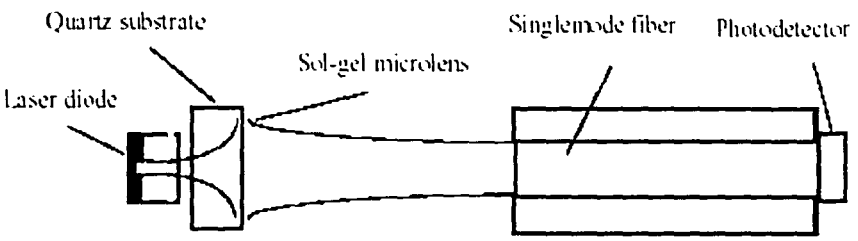

Figure 6 - Microlens aligned to optical fiber

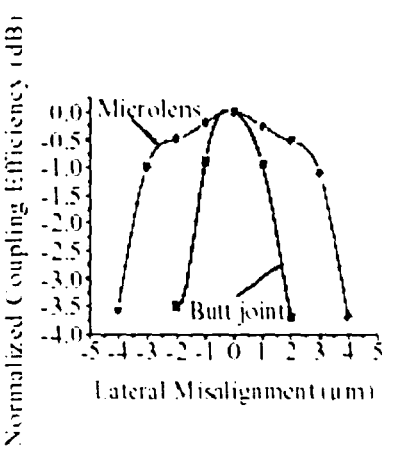

Figure 7 - Lateral tolerance of microlens alignment

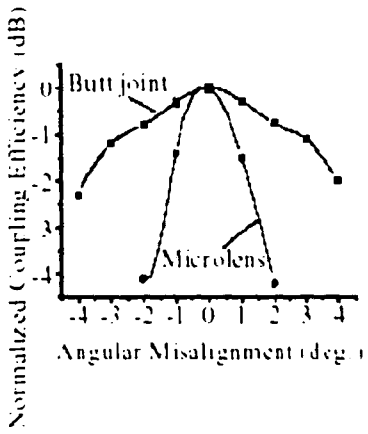

Figure 8 - Angular tolerance of microlens alignment

2.3 MEMS-based Alignment Technologies

In full-scale manufacturing, a MEMS solution to the fiber-to-fiber or fiber-to-waveguide optical alignment problem has yet to be implemented. Certainly there have been a good number of journal articles and prototype devices demonstrated. Even within the MEMS field, many different technologies have been used to achieve optical alignment. A brief survey of the literature in the field has turned up a number of articles, summarized in Table 1 on the following page.

Table 1 - Overview of MEMS optical alignment technologies[29]

Object	Principle	Method	DOF	Range	Fabr.	Reference
Fiber	E-static	Metallized Fiber	2 T	XY 25um	Bulk	Hockaday[7], Jebens et al. [8], Kikuya et al.[910], 1992
Fiber	E-magnetic	Electroplated FeNi	1 T	150um	N/A	Nagaoka[11], 1997
Fiber	E-magnetic	Permanent Magnet	2 T	XY 100um	Bulk	Gerlach et al.[12], 1997
Fiber	Thermal	Arch Beam (XZ) & Bimorph (Y)	3 T	XZ 30um, Y 120um	Bulk	Haake, Wood et al.[1314], 1998
Fiber	Thermal	Folded buckling mode	1 T	X 12um	Bulk	Syms et al.[15], 2004
Fiber	Thermal	Thick arm / thin arm	1 T	X 125um	Bulk	Field et al.[16]1996
Fiber	Thermal	Selective Current	1 T	X 400um	Bulk	Kopka et al.[17], 2000
Fiber	SMA	Bending arc	1 T	Y 125um	N/A	Jebens et al.[18]1993
Fiber	Piezoelectric	Mono- and bimorph cantilever	2 T	XY 100um	Bulk	Gerlach et al.[19], 1997
Fiber	Thermal	Chevron Actuator	1 T	X 24um	Bulk	Unamuno et al., 2002
Lens (int.)	E-static	Comb drive	2 T	XZ 48um	Bulk	Kim et al.[20], 1999
Lens (int.)	E-static	Scratch drive	3 T	XZ 110um, Y 250um	Surface	Fan et al.[21], 1997
Lens (int.)	E-static	Scratch drive	2 T (1 R)	XZ 110um, Y 250um	Surface	Fan et al.[22], 1998
Lens (ext.)	E-static	Comb drive	1 T	X 72um	Bulk	Grade et al.[23], 2004
Mirrors & Lens	E-static	Scratch drive	2 R, 1 T	90 deg, 80um	Surface	Lin et al.[24], 1997
Mirrors	Thermal	Hot arm/cold arm	2 R (2 T)	2.5 deg	Surface	Ishikawa et al.[25], 2003
Mirrors	E-static	Vibromotor	2 R, 1 T	2 deg, 80 um	Surface	Solgaard et al.[26], 1995
Mirrors	E-static	Parallel plate	1 R	1 deg	Surface	Zhang et al.[27], 2003
Platform	Thermal	Buckling mode	1 T	X 110um	Bulk	Syms et al.[28]2004
Platform	Thermal	V-shaped actuator	1 T	X 40um	Bulk	Haasl[29], 2005
Platform	Thermal	V-shaped actuator	1 T	Y 9um	Bulk	Haasl[29], 2005

The headings of Table 1 are defined by Haasl[29]. "Object" refers to the object that is moved. "DOF" represents the Degrees Of Freedom of the system. DOF is given by number and type; T for translational and R for rotational. "Range" defines the orientation and distance through which motion occurs. Y is the axis out of plane, and Z is the direction along the optical axis. "Fabrication" gives the method of fabrication of the actuator- surface or bulk micromachining.

Space does not permit a comprehensive examination all of the papers listed in Table 1; a review of a few selected concepts must suffice.

Haake, Wood et al.[13] developed a thermal actuator. This device is the subject of considerable study in this work, and will be explored in depth in another chapter. In brief, the device consists of three thermal actuators allowing full X, Y and Z motion. The XY capability is approximately 25um in each axis, and in the Z axis the maximum displacement has been reported as 120um. The thermal expansion of high aspect ratio LIGA structures drives the displacement of this device. The locking mechanism to affix the fiber is not an intrinsic part of this device. This device is shown in Figure 9 - IPMA Aligner concept. While critics contend that this device takes up a lot of space, note that none of the other devices surveyed in this work provide three independent axes of motion in a smaller footprint.

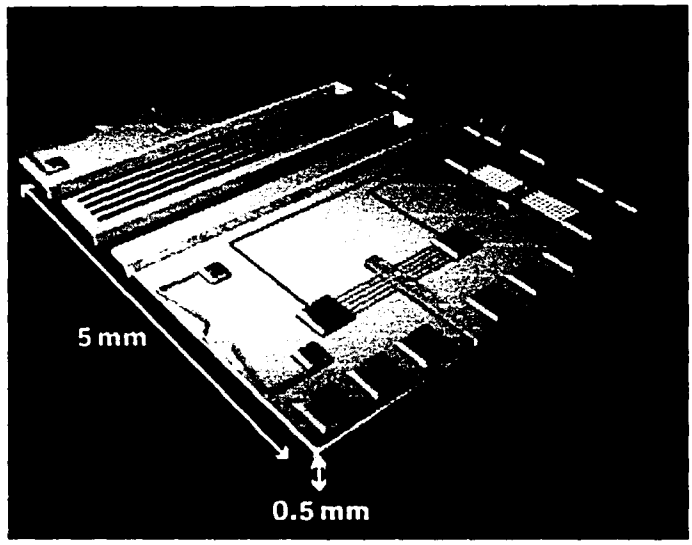

Figure 9 - IPMA Aligner concept[13]

Kiyka et al.[9] developed an electrostatic actuator. This device translates the end of a metallized fiber in the XY plane to a maximum of 25um in each direction. The metallized fiber is attached to ground and a voltage potential is selectively applied between the fiber and one or both of the aluminum electrodes. A maximum of 40V is required to move the fiber tip. This technology is well adapted to existing MEMS fabrication technologies. Self-limiting wet etched v-grooves are well understood, and the electrodes are created using a standard lift-off process. The length of the fiber in the trench is approximately 10mm, making this solution a bit ungainly for a standard optoelectronic package. No intrinsic locking mechanism is included in this concept, but the authors recommend that a UV curable epoxy is used to permanently affix the fiber in place once optimal alignment is achieved. There is no Z axis motion in this scheme. Figure 10 shows a conceptual view of this device.

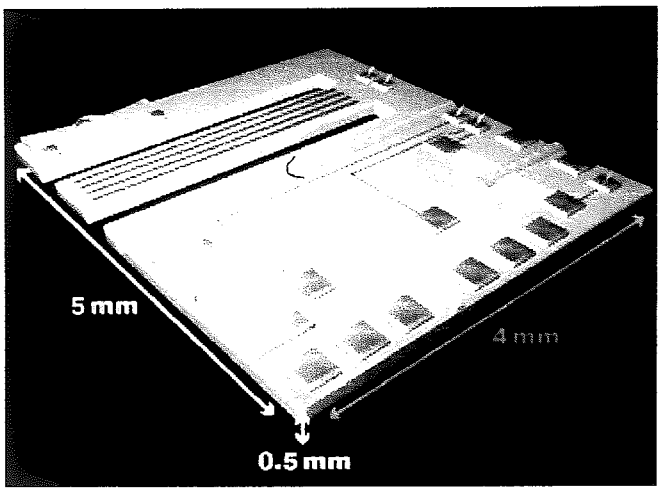

Figure 9 - IPMA Aligner concept[13]

Kiyka et al.[9] developed an electrostatic actuator. This device translates the end of a metallized fiber in the XY plane to a maximum of 25um in each direction. The metallized fiber is attached to ground and a voltage potential is selectively applied between the fiber and one or both of the aluminum electrodes. A maximum of 40V is required to move the fiber tip. This technology is well adapted to existing MEMS fabrication technologies. Self-limiting wet etched v-grooves are well understood, and the electrodes are created using a standard lift-off process. The length of the fiber in the trench is approximately 10mm, making this solution a bit ungainly for a standard optoelectronic package. No intrinsic locking mechanism is included in this concept, but the authors recommend that a UV curable epoxy is used to permanently affix the fiber in place once optimal alignment is achieved. There is no Z axis motion in this scheme. Figure 10 shows a conceptual view of this device.

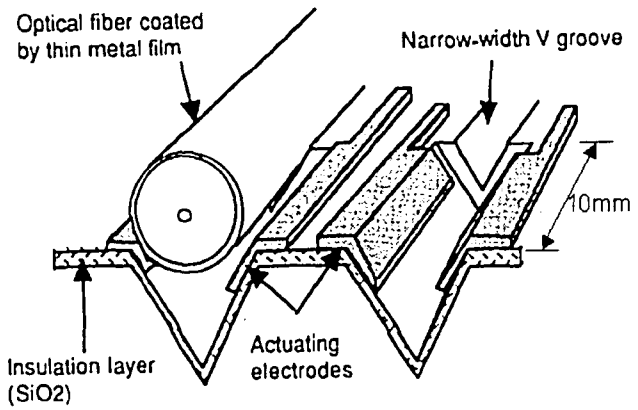

Figure 10 - Electrostatic fiber alignment device[9]

Gerlach et al.[12] developed piezoelectric actuators. As with Kiyka et al.[9], this device also provides only XY motion. An optical fiber or lens is attached to the end of a piezoelectric bimorph. A piezoelectric monomorph is affixed to a hinge point on a piezoelectric bimorph. Actuation of the monomorph will cause a rotation, which due to the long beam length of 10mm can be treated as a translation in X. Actuation of the bimorph will cause a second rotation that can be interpreted as a translation in Y. This device is reported as having an actuation range of 100um in each of the X and Y directions. Actuation voltages are not reported, and there is no mention of how the fiber would be permanently affixed. An illustration of the device is shown in Figure 11.

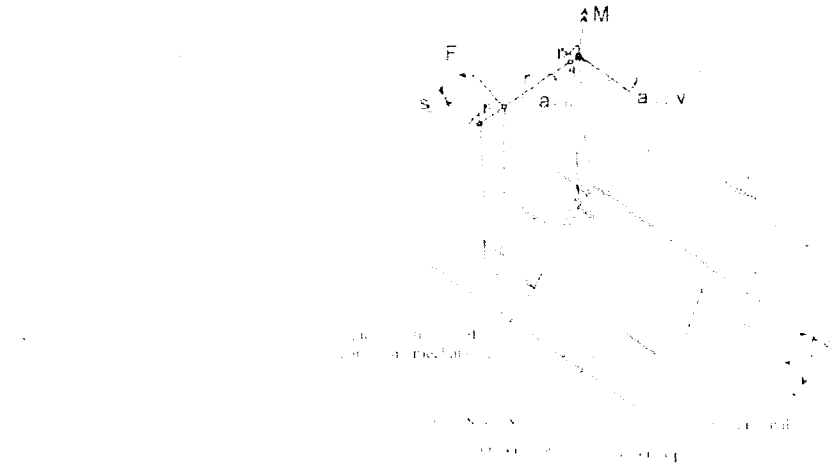

Figure 11 - Piezoelectric actuator concept[12]

Syms et al.[15] developed thermoelectric actuators. At first glance, the structures shown in this concept are similar in nature to the actuators developed by Haake et al. [13] Note that the expensive LIGA photolithography structures have been substituted here with DRIE etched silicon members on an SOI (Silicon-On-Insulator) wafer. Silicon is a less attractive material than electroplated nickel for electrothermal actuators because of its reduced expansion coefficient and higher thermal conductivity, but it is far easier and less costly to use in the fabrication of high aspect ratio structures. The use of silicon rather than metal does mean that larger structures are required to achieve comparable forces, and in this case the actuators are 4mm long, as compared to 1mm in the device by Haake et al. The force achieved is significantly lower as well at only 0.4mN. This device is demonstrated in only the X direction. A method to expand this concept to three-dimensional motion is not presented. As with all the previous concepts, no method is mentioned for locking the fiber in place as an intrinsic part of device functionality. A conceptual illustration of the device is presented as Figure 12 – Thermoelectric actuators.

Figure 11 - Piezoelectric actuator concept[12]

Syms et al.[15] developed thermoelectric actuators. At first glance, the structures shown in this concept are similar in nature to the actuators developed by Haake et al. [13] Note that the expensive LIGA photolithography structures have been substituted here with DRIE etched silicon members on an SOI (Silicon-On-Insulator) wafer. Silicon is a less attractive material than electroplated nickel for electrothermal actuators because of its reduced expansion coefficient and higher thermal conductivity, but it is far easier and less costly to use in the fabrication of high aspect ratio structures. The use of silicon rather than metal does mean that larger structures are required to achieve comparable forces, and in this case the actuators are 4mm long, as compared to 1mm in the device by Haake et al. The force achieved is significantly lower as well at only 0.4mN. This device is demonstrated in only the X direction. A method to expand this concept to three-dimensional motion is not presented. As with all the previous concepts, no method is mentioned for locking the fiber in place as an intrinsic part of device functionality. A conceptual illustration of the device is presented as Figure 12 – Thermoelectric actuators.

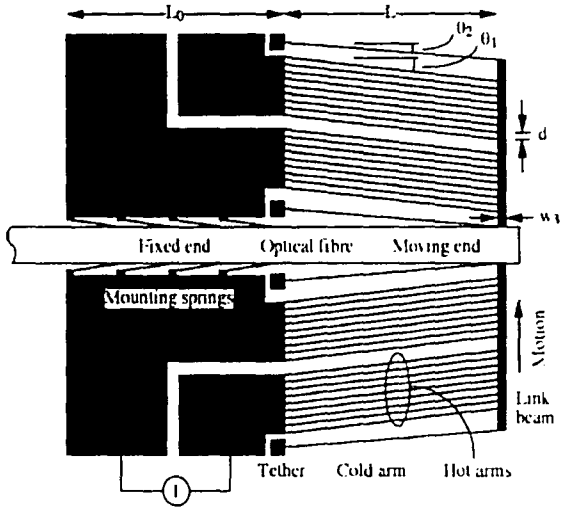

Figure 12 – Thermoelectric actuators[15]

Kopka et al.[17] developed U-shaped cantilever actuators. These devices are intended to translate and align one optical fiber to any of four other fibers in an optical switch application. This research team is particularly interested in minimizing any angular motion of the fiber. As seen in the piezoelectric concept by Gerlach et al. [12], an angular motion can be treated as a translation, but it is true that even small angles of 1.5° can adversely affect optical coupling. Kopka et al. [17] have placed two thermoelectric actuators in tandem in a fixed-fixed beam configuration, allowing for fiber translation without rotation. As this technology is intended for a switching application, it is implemented in only one dimension, with a total translation range of 400um. A mechanical clamp in the form of a silicon V-groove substrate is used to ensure that the fiber is firmly located in one of four possible configurations. This is a robust solution, but offers locking resolution of 125um – several orders of magnitude coarser than that required for a fiber to waveguide alignment. The silicon cantilevers are activated by joule

heating, and are an ungainly 20mm long. Power required for 200um of motion in either the positive or negative direction is 1.2W. The concept is illustrated by Figure 13 - U-Shaped cantilever actuators.

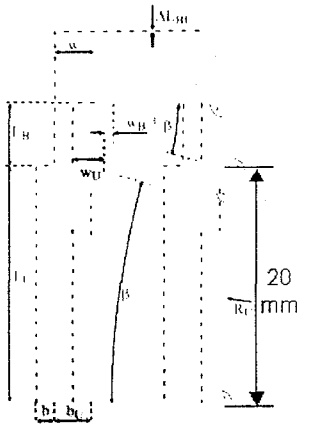

Figure 13 - U-Shaped cantilever actuators[17]

Kim et al.[20] develped a silicon micro XY stage. This project takes an approach similar to Haake et al. [13] Instead of directly handling the optical lens or fiber, an entire platform to which the optical elements can be attached is translated in the XY plane. This device is a bit unique in that it is using comb drives for the driving mechanisms. As with Syms et al. [15] the structural elements are silicon rather than LIGA metal. Motion of 50um is reported in both the X and Y-axes, at a 20V applied potential. It is worth noting that this system has direct position feedback on each of the four groups of comb drives. One of the combs is used as a position feedback sensor- a feature that is not included in any of the other concepts reviewed in this thesis. No method of locking is demonstrated for this concept. A CAD model of the device with critical features labeled is shown in Figure 14.

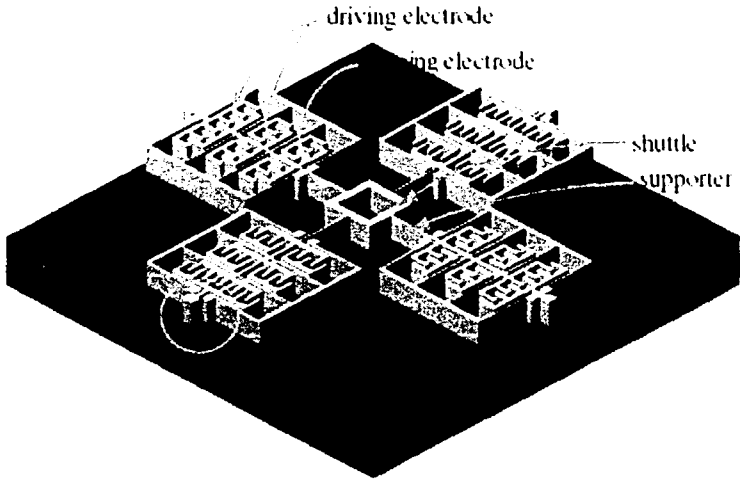

Figure 14 - Silicon Micro XY stage[20]

Syms et al. have contributed a second device design to the literature[15], a latching translation stage. As with Haake and Kim, the device moves an entire optical platform. As seen in the first Syms device, the buckling mode electrothermal actuators are realized in silicon. There is a novel twist on the first in that it includes a discrete latching mechanism to hold the device in place. The latching accuracy at 10um is better than that exhibited by Kopka, but is still insufficient for the submicron placement demanded by waveguide devices. The device exhibits a satisfactory 110um of translation, but only in one direction. 2.2W of power are required to achieve maximum alignment, but no power is required to hold this position. An overall illustration of the device and a SEM picture of the latching mechanism are shown in Figure 15 and Figure 16, respectively.

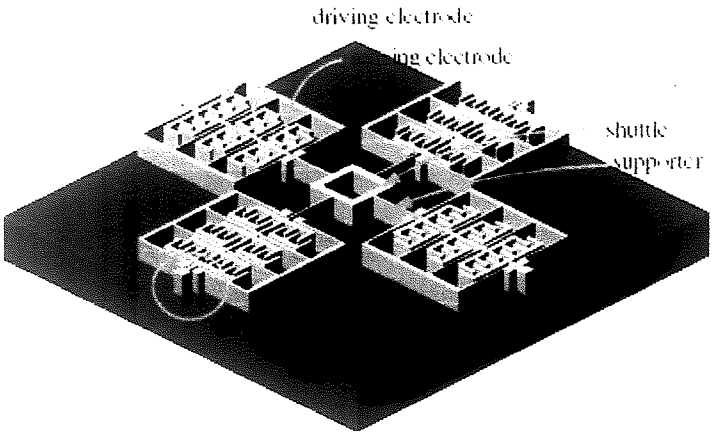

Figure 14 - Silicon Micro XY stage[20]

Syms et al. have contributed a second device design to the literature[15], a latching translation stage. As with Haake and Kim, the device moves an entire optical platform. As seen in the first Syms device, the buckling mode electrothermal actuators are realized in silicon. There is a novel twist on the first in that it includes a discrete latching mechanism to hold the device in place. The latching accuracy at 10um is better than that exhibited by Kopka, but is still insufficient for the submicron placement demanded by waveguide devices. The device exhibits a satisfactory 110um of translation, but only in one direction. 2.2W of power are required to achieve maximum alignment, but no power is required to hold this position. An overall illustration of the device and a SEM picture of the latching mechanism are shown in Figure 15 and Figure 16, respectively.

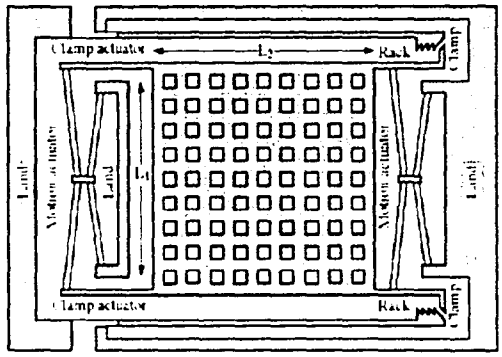

Figure 15 - Illustration of latching optical platform[15]

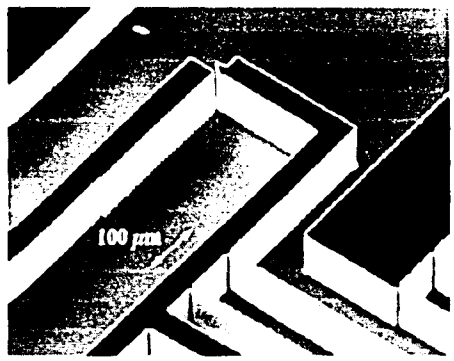

Figure 16 - Detail of latching mechanism[15]

Haasl et al.[29] developed polymer V-shaped actuators. All of the devices reported up to this point have used ceramic, silicon or metal as the basis of the actuator itself. There is emerging research in the field of polymer actuators, as described by Haasl et al. A polymer called bis-cyclobutene (BCB) is used to fill an angled joint, which could be fabricated in and XY or XZ configuration. As the BCB is heated, it expands more in the thick part of the joint than the thin part, causing a rotation. This concept is shown in Figure 17 below. Figure 18 illustrates how this rotational motion can be combined with

other joints to produce translational motion of an XY stage, to which a fiber or optics can be affixed. Motion of 35um was achieved in X and Y with 0.35W of applied power. No locking mechanism is included.

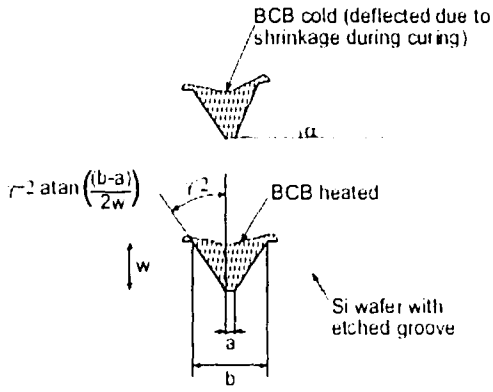

Figure 17 - Polymer actuator concept[29]

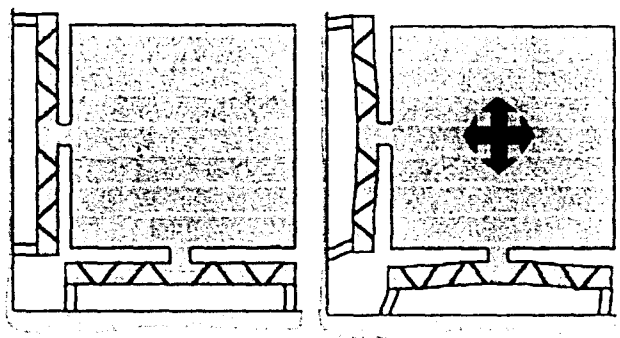

Figure 18 - XY stage driven by polymer actuators[29]

In summary, there are many methods demonstrated in the literature to move optical elements. Thermal expansion seems to be the most common method. This makes sense- it generates more force than other solutions, but is also the most power hungry.

Not all of the literature shows devices that can obtain translation in the X, Y and Z-axes. Some of the devices are certainly too large to fit in established optoelectronic packages, to say nothing of the shrinking package sizes associated with new applications. Clearly, there is room for further refinement and research in these areas.

More strikingly, what seems to be missing is a way to fix this motion in place with the submicron level accuracy demanded of fiber-to-fiber or fiber-to-waveguide alignment. Only a scant few of the reviewed technologies demonstrated any locking at all. Of those that did, none approached the required resolution. Any successful deployment of the technology needs to address not just the amount of the motion and magnitude of the force, but the amount of shock and vibration that a device can withstand without losing alignment. Few end users of the device will tolerate the additional power required to actively maintain the alignment. Alignment must be maintained under no power conditions.

One element critical to the success of a design is completely unaddressed in the literature- Reliability. None of the research reviewed tested a device under load to the failure point. It would be interesting to know how many cumulative meters of alignment can be achieved over the life of a single device. How does this life change over temperature cycling, or in a high temperature environment?

In comparing the devices created to date, the most mature technology appears to be the In Package Micro Aligner concept by Haake et al.[13] This device is the topic of the next chapter.

Chapter 3
Engineering of the In-Package-Micro-Aligner

3.1 Device dimensions and materials

Dimensions and material analysis were characterized by the MEMS Exchange of Reston, VA using Scanning Electron Microscopy (SEM) and Energy Dispersive X-ray Analysis (EDX). Several SEM pictures of the IPMA device were also taken locally at Lehigh University to better understand the workings and design of the device. Figure 19 is a macroscopic view of the IPMA device. This particular device is missing the cantilever structure for y axis motion which was broken during the dicing procedure.

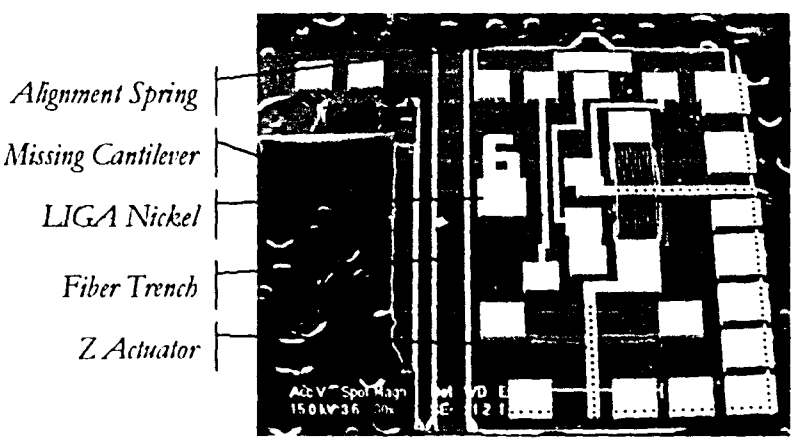

Figure 19 - SEM Picture of an IPMA device

Figure 20 is a closer view of the X actuator. Of interest is the slight bow to the rib structures attached to the pusher, as well as an integrated back stop. Both of these

Chapter 3
Engineering of the In-Package-Micro-Aligner

3.1 Device dimensions and materials

Dimensions and material analysis were characterized by the MEMS Exchange of Reston, VA using Scanning Electron Microscopy (SEM) and Energy Dispersive X-ray Analysis (EDX). Several SEM pictures of the IPMA device were also taken locally at Lehigh University to better understand the workings and design of the device. Figure 19 is a macroscopic view of the IPMA device. This particular device is missing the cantilever structure for y axis motion which was broken during the dicing procedure.

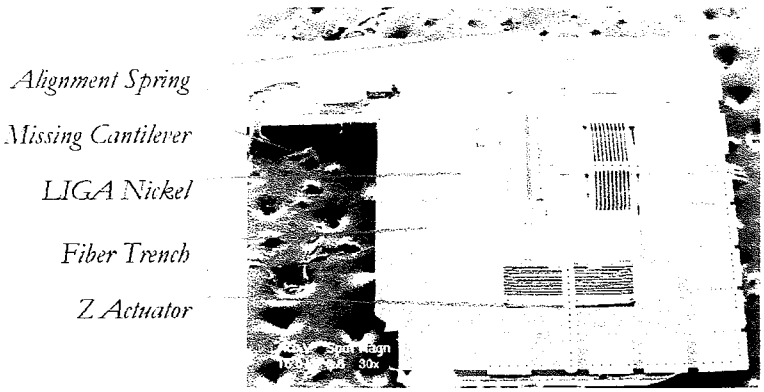

Figure 19 - SEM Picture of an IPMA device

Figure 20 is a closer view of the X actuator. Of interest is the slight bow to the rib structures attached to the pusher, as well as an integrated back stop. Both of these

features allow for motion in only one direction along the axis from the initial unbiased condition.

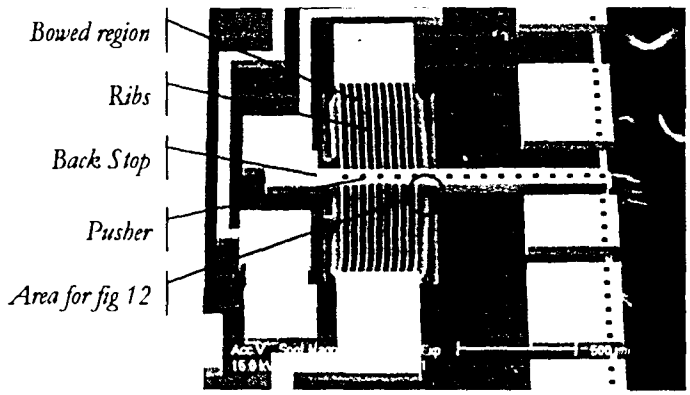

Figure 20 - X-axis actuator

Figure 21 shows a high magnification view of the pusher. The gap between the pusher and the substrate is approximately 1 micron.

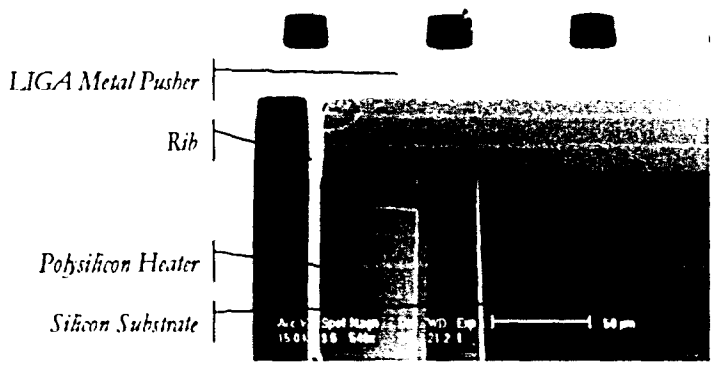

Figure 21 - Actuator detail

features allow for motion in only one direction along the axis from the initial unbiased condition.

Figure 20 - X-axis actuator

Figure 21 shows a high magnification view of the pusher. The gap between the pusher and the substrate is approximately 1 micron.

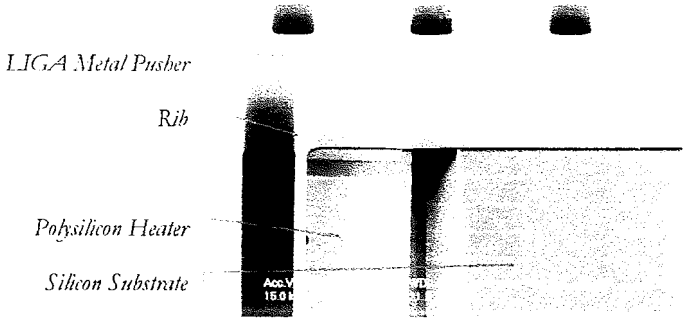

Figure 21 - Actuator detail

A plan view of half of the heater is shown in Figure 22. The heater is arranged in a serpentine pattern beneath the ribs. As the heat is radiated and convected from the polysilicon surface, the nickel ribs experience a small increase in length due to the high coefficient of thermal expansion (CTE) of nickel. This increase is amplified by the design of the ribs, and causes the pusher to deflect.

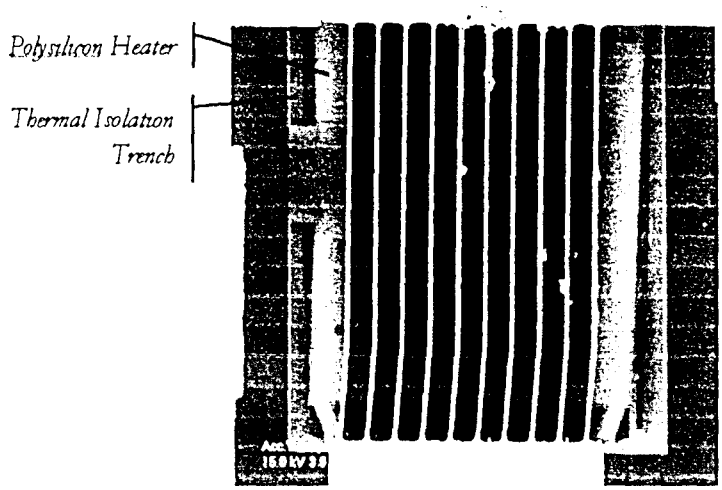

Figure 22 - Plan view of actuator

In Figure 23 the heater is shown to be thermally isolated from the silicon substrate. There is a deep etch from the back of the device (not shown), and a shallower etch which is visible from the top of the device.

A plan view of half of the heater is shown in Figure 22. The heater is arranged in a serpentine pattern beneath the ribs. As the heat is radiated and convected from the polysilicon surface, the nickel ribs experience a small increase in length due to the high coefficient of thermal expansion (CTE) of nickel. This increase is amplified by the design of the ribs, and causes the pusher to deflect.

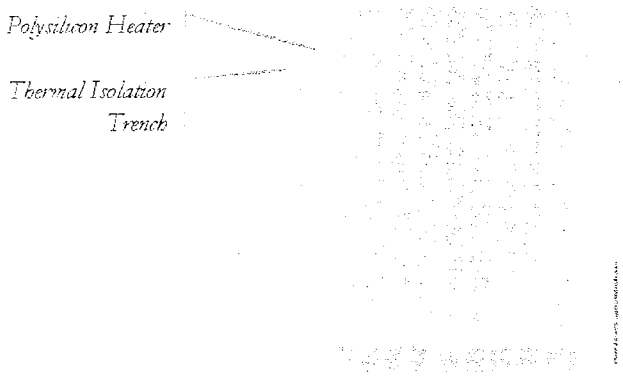

Figure 22 - Plan view of actuator

In Figure 23 the heater is shown to be thermally isolated from the silicon substrate. There is a deep etch from the back of the device (not shown), and a shallower etch which is visible from the top of the device.

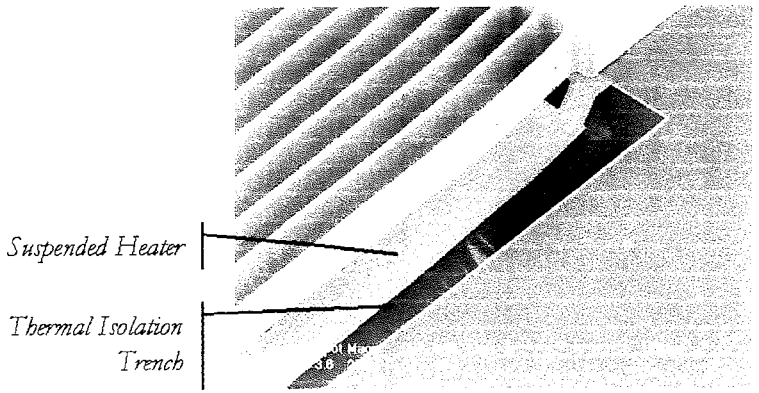

Figure 23 - Heater etch detail

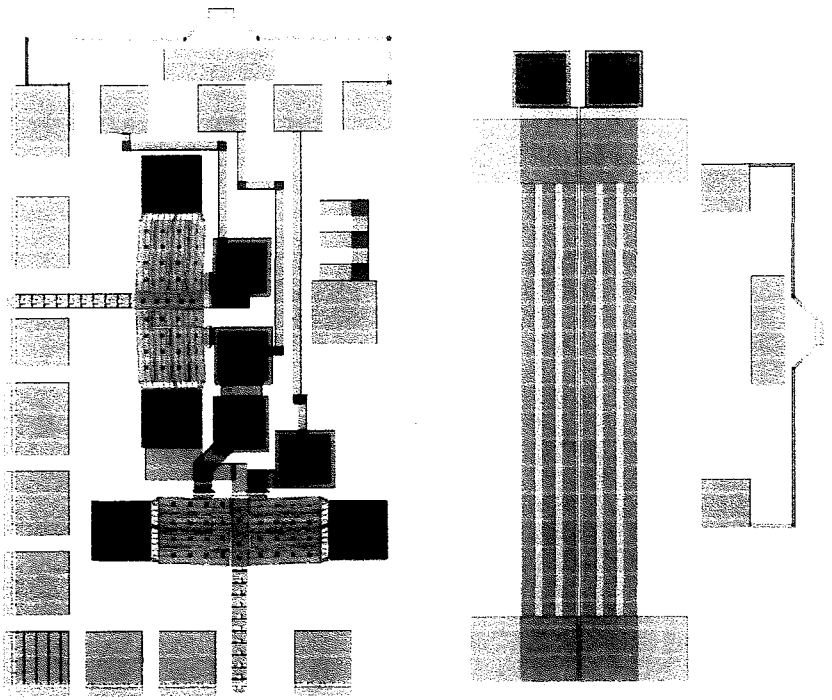

Figure 24 - Mask data

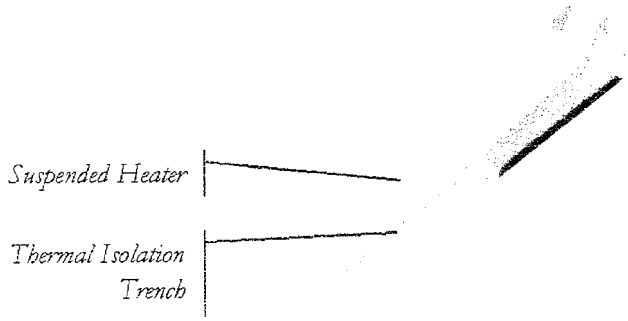

Figure 23 - Heater etch detail

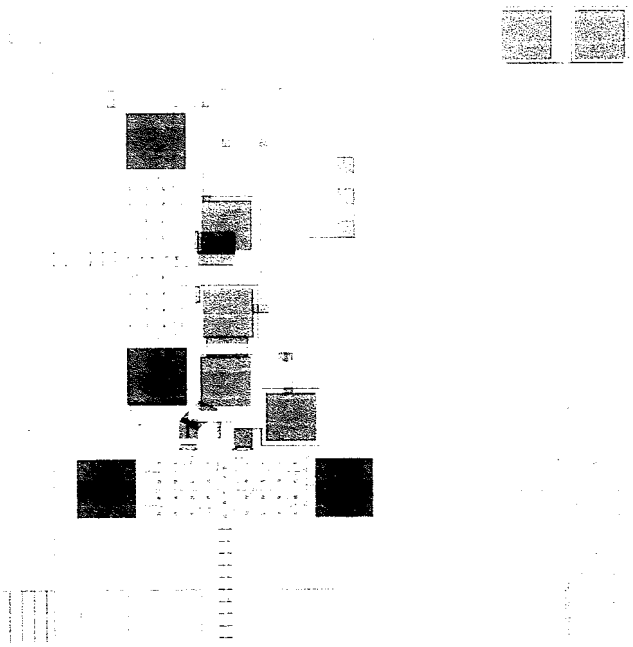

Figure 24 - Mask data

Based on similar SEM images, the MEMS-Exchange quantitatively measured the device dimensions and used the information to create CAD data to be used for mask fabrication. Figure 24 shows the data for the masks.

The architecture of the device is straightforward. The silicon die serves as a carrier for three elements: the fiber, a series of resistive heaters and a thick layer of nickel fabricated using a technique known as LIGA.

The acronym LIGA is German and stands for "**LI**thographie, **G**alvanoformung, und **A**bformung". In English this translates as Lithography-Electroplating-Molding. In the LIGA process, deep x-ray lithography is used to create a patterned mask in a thick layer (100 microns is typical) of polymethylmethacrylate (PMMA) photoresist. This mask sits on top of a thin film of metal to be used as a base layer for plating. Where the PMMA has been selectively removed to reveal the plating base, additional metal may be plated up. This process is very useful for fabricating features with large height-to-width aspect ratios and vertical sides.

3.2 Device Operation

The In Package Micro Aligner (IPMA, henceforth) developed by Haake and Wood translates an attached optical fiber in the X, Y and Z axes inside a sealed hermetic package. This eliminates the need for large and costly laser welders or other external fiber alignment hardware, and also allows for re-alignment of the fiber while the unit is deployed in the field. A series of illustrations will show how the device operates.

Each direction of motion (X, Y and Z) has an associated actuator. An electrical current applied to one of the heaters causes a thermal expansion of the nickel and translation of the entire die along one of the three axes.

Figure 25 shows the MEMS aligner dropping into the package. The aligner die is located inside of a LIGA nickel frame. This framework provides a reference surface for the actuators to push against.

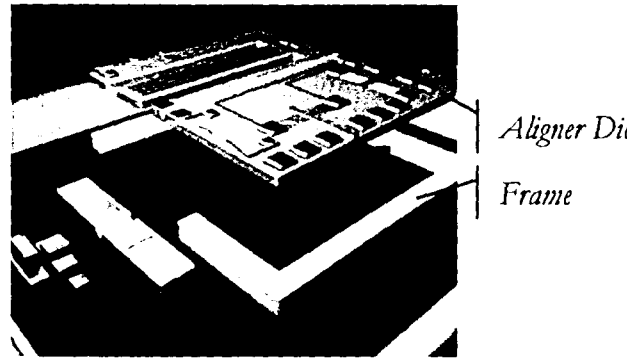

Figure 25 - IPMA and frame

Two compliant springs are shown in Figure 26. These springs allow the device to move inside the frame when the actuators are extended.

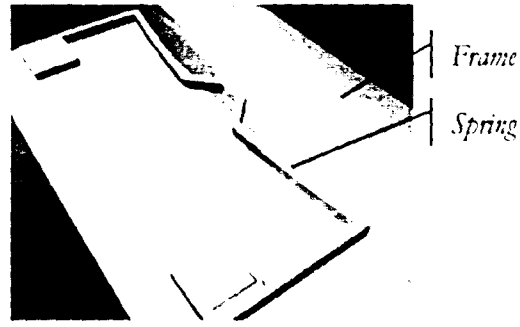

Figure 26 - IMPA compliant spring

Figure 27 illustrates the device ready to begin the alignment sequence. All wirebonding is complete, the device is secure inside the framework, and the fiber is attached to the die. The fiber-to-die attachment method could be epoxy or solder. The laser diode and a separate lock-in-place mechanism can also be seen in this view.

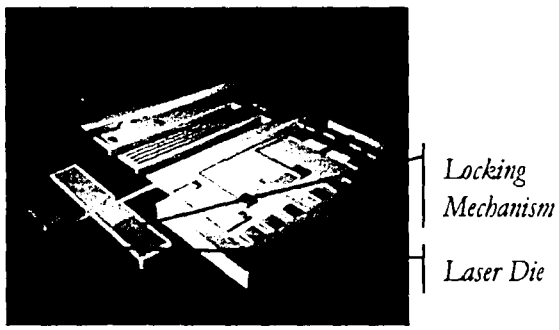

Figure 27 - Diode and locking mechanism

The actuators for the X, Y and Z axes are identified in Figure 28. The X and Z actuators are identical in design. The Y actuator is of a different architecture.

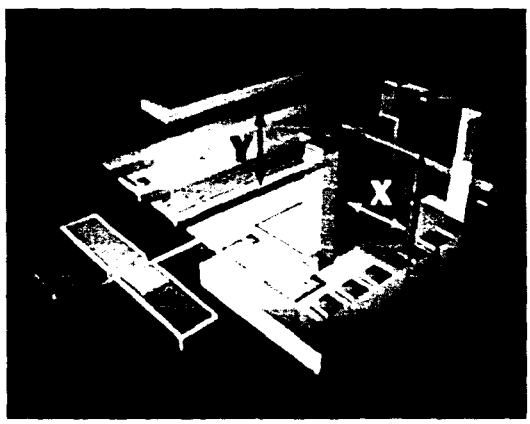

Figure 28 - X, Y and Z actuators

Figure 27 illustrates the device ready to begin the alignment sequence. All wirebonding is complete, the device is secure inside the framework, and the fiber is attached to the die. The fiber-to-die attachment method could be epoxy or solder. The laser diode and a separate lock-in-place mechanism can also be seen in this view.

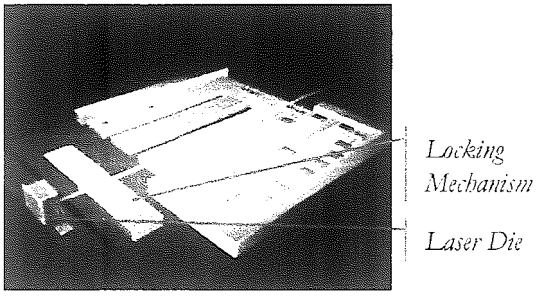

Figure 27 - Diode and locking mechanism

The actuators for the X, Y and Z axes are identified in Figure 28. The X and Z actuators are identical in design. The Y actuator is of a different architecture.

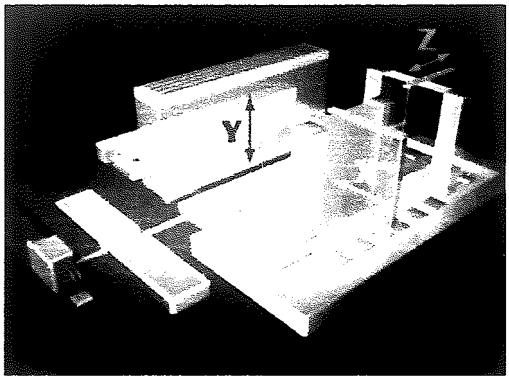

Figure 28 - X, Y and Z actuators

The X actuator is shown in an unbiased state in Figure 29. When electrical current is passed through an integrated polysilicon heater the actuator extends, translating the entire die along with the attached fiber. This is shown schematically in Figure 30.

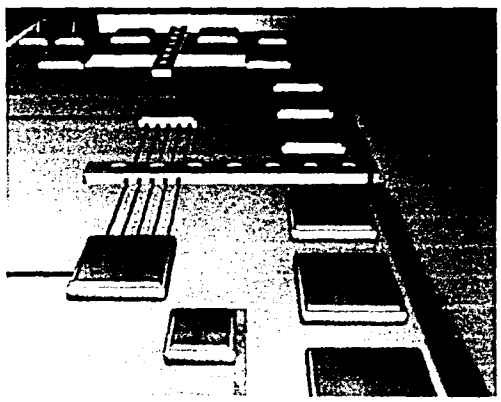

Figure 29 - Unbiased actuator

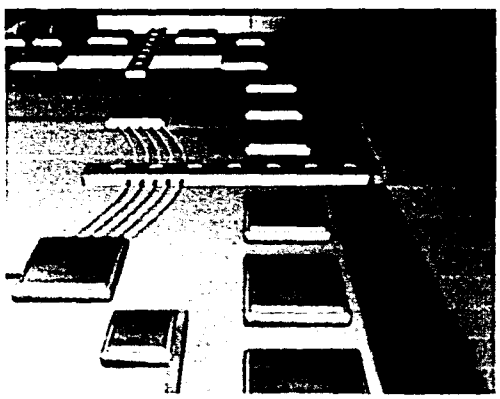

Figure 30 - Biased actuator

Figure 31 illustrates the design of the Y actuator. It is a bimorph of a silicon base layer, an integrated heater and thick LIGA nickel on the top surface. As is shown in

Figure 32, when the heater is biased the beam deflects, resulting in motion in the Y direction.

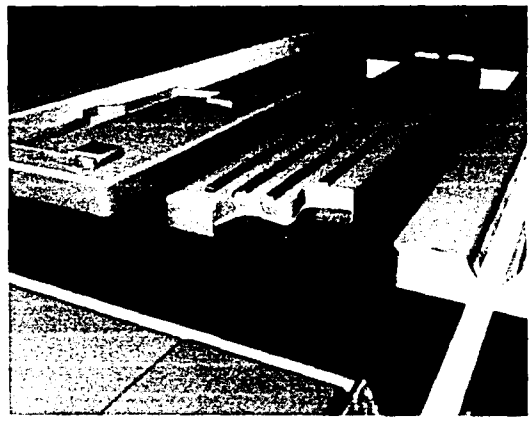

Figure 31 - Cross section of bimorph

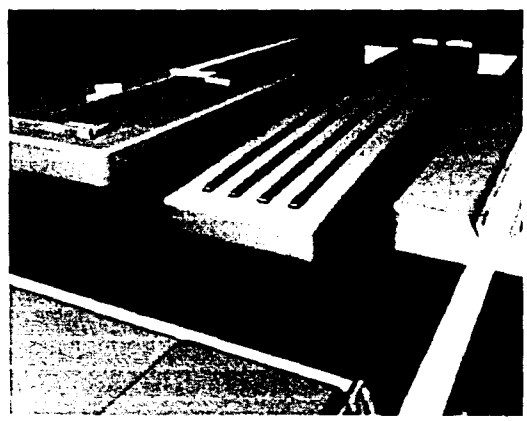

Figure 32 - Deflected bimorph

Once the fiber is aligned to the laser die, a separate locking mechanism, shown as a solder reflow pad in Figure 27, is used to fix the location of the fiber and the bias to the actuators is removed.

3.3 Possible Process Sequence

Detailed discussions with the MEMS-exchange and the original inventor of the Boeing device have yielded a possible process sequence for creating this version of the MEMS Fiber Optic Aligner. Figure 32 and Figure 34 illustrate the process sequence.

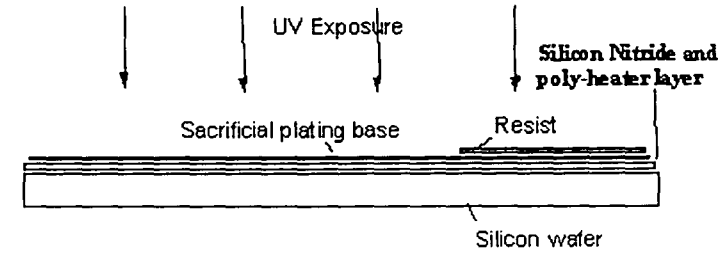

1. Sacrificial Layer Patterning

Pattern etch sacrificial plating base layer

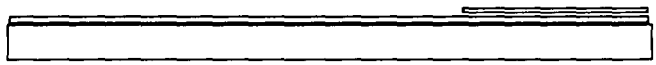

2. Pattern Etch of Sacrificial Layer

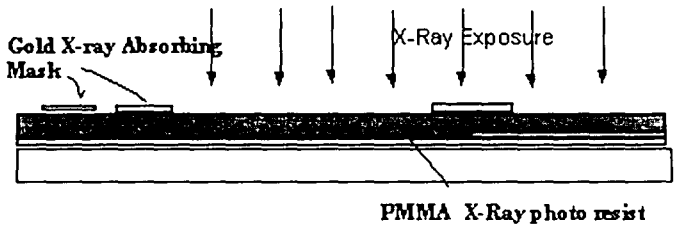

3. PMMA X-Ray Exposure

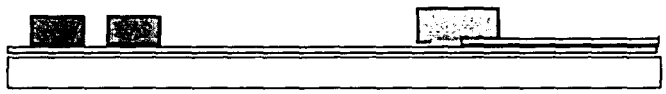

4. Develop PMMA layer

Figure 33 - Process sequence

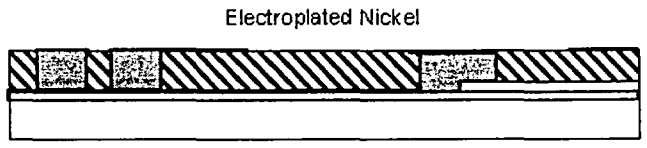

5. Electroplating the First layer of Metal

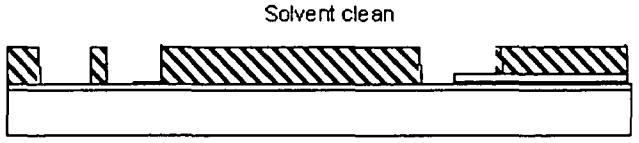

6. Dissolve PMMA

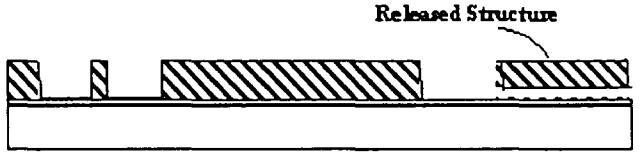

7. Etch sacrificial plating base

8. Backside etch for thermal and mechanical relief

Figure 34 - Process sequence (cont'd)

In step one the silicon wafer is patterned with the nitride and heater layers, and is then covered with a thin film of titanium as a sacrificial plating base. This titanium serves as a platable layer for the nickel to be deposited later in the process and is also etchable with hydrogen peroxide, as is shown in step two.

Steps three and four show the beginning of the LIGA process. A thick layer of PMMA has been spun on the wafer and is then patterned. Steps five and six illustrate the plating and subsequent planarization of the Nickel, followed by removal of the PMMA. Finally, the sacrificial Ti layer is removed in step six, allowing for overhanging or free moving structures. The backside of the wafer is then etched underneath the polysilicon heaters. This etch creates a window beneath and around the heater membrane that acts as a thermal choke, preventing the heat from dissipating rapidly into the silicon substrate.

The existing process sequence has been successfully employed, as is evident from the working Boeing devices. However, it presents several challenges. First, the LIGA process is available at only a few fabrication facilities, limiting options for selecting a manufacturer. Second, the cost of LIGA masks and processing is greater than for thin film methods. Finally, dicing wafers with the overhanging passive spring and the current cantilever design is difficult, and can reduce yield. All of these are issues that may be addressed by redesign of critical aspects of the structure and process sequence.

3.4 Device performance

The maximum displacements and forces available from the in-plane actuators limit the amount of misalignment the device can correct. Measuring the displacement of the in-plane actuators (X and Z axes) is fairly straightforward. The devices were attached to a current source, and viewed under a measuring microscope, as described below. It is more difficult to get accurate force measurements for these actuators.

The displacement was measured using a DC current source and a measuring microscope, model Nikon MM-60. The displacement is approximately linear with increasing heater current as shown for three devices in Figure 35 (C4-V, DEMO1-D and DEMO2-D). The maximum observed displacement of the pusher is 28 microns, which was attained at a bias of 16mA and 55V (see Figure 36). Devices biased into the 22mA range with over 70V will fail. The amount of heat generated causes the thin film heater to permanently degrade. This points to one potential path for improvement over the existing device: to refine the heater design so that lower voltages are required for full deflection.

A maximum displacement of 28 microns is adequate for correcting the alignment of most fibers, but leaves little room for unexpected process variations. A maximum displacement of 50-100 microns would be advantageous, and provides another goal for improvement. Hysteresis and resolution data for these devices was not recorded. Repeated measurements with the measuring microscope demonstrated a limit to the accuracy of the displacement measurement. The error bars in Figure 35 show the +/- 2um accuracy observed with repeated measurements of the length of a fiducial mark.

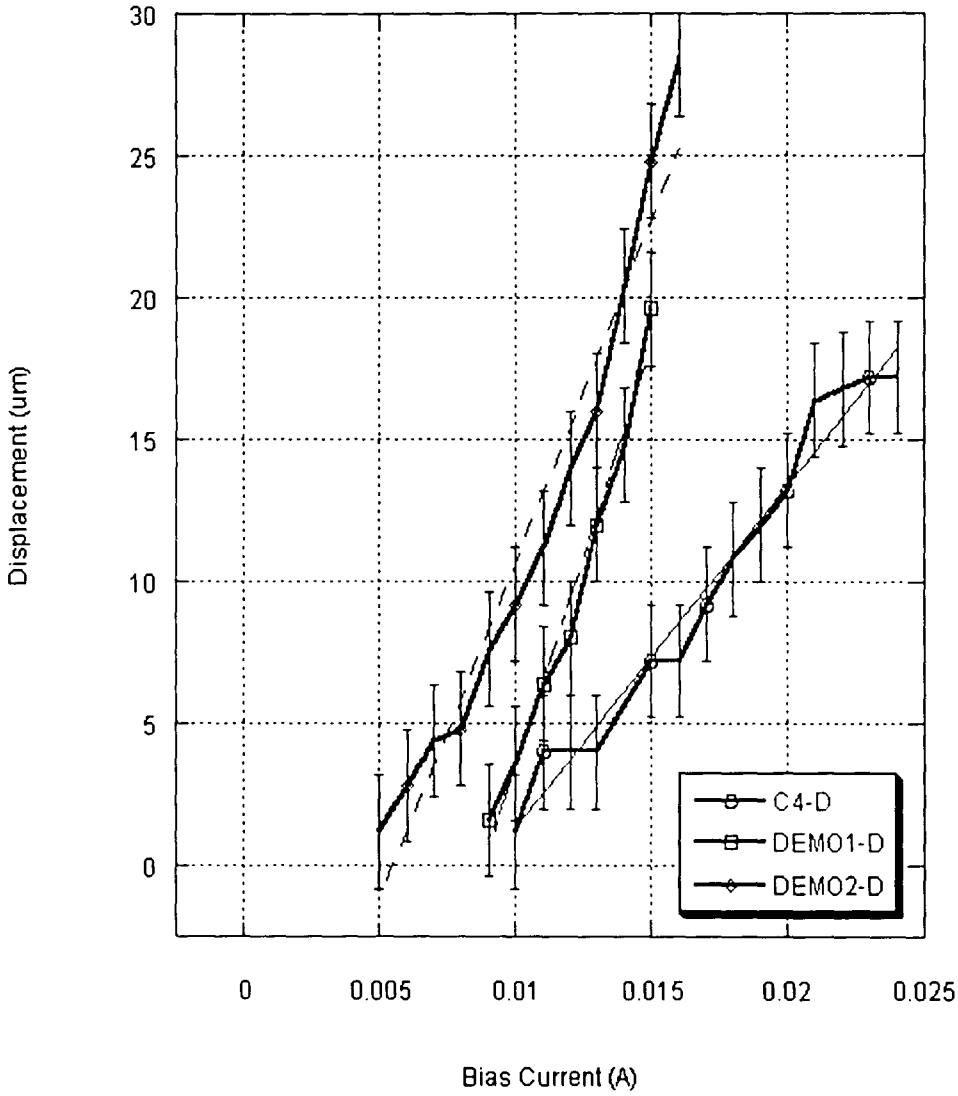

Figure 35 - Displacement response

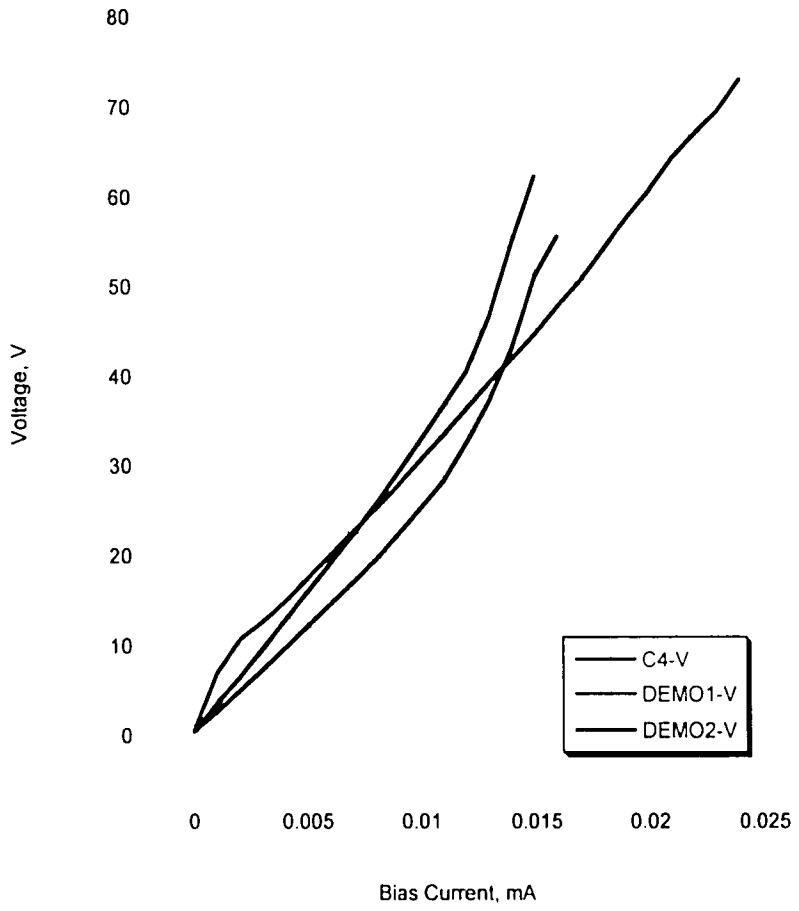

Figure 36 - Voltage response

The force capability of the in-plane actuators has been characterized as well. The method used to obtain force measurements is the same as that described by Haake et. al.[30] With the actuator biased and extended by a measurable amount, a cantilevered 0.125mm diameter glass fiber is used to push the actuator back to the zero position (i.e., the position it would be in if no bias were applied). The amount of lateral deflection in the glass fiber required to push the cantilever back into position is then measured visually using the Nikon MM-60 measuring microscope. Repeated measurements with the microscope found an accuracy of 2 microns. Bars on the plots account for this error. The

relationship between the applied force and the deflection of the cantilevered glass fiber is available in Machinery's Handbook (Industrial Press) or any standard mechanics handbook. These data are plotted in Figure 37.

The experimental data was compared to a finite element analysis (FEA) completed in ANSYS, the results of which are also shown in Figure 37. A view of the deflected actuator from ANSYS is shown as Figure 38. Error bars are included to show the accuracy of the Nikon MM-60 measuring microscope, +/- 2 microns.

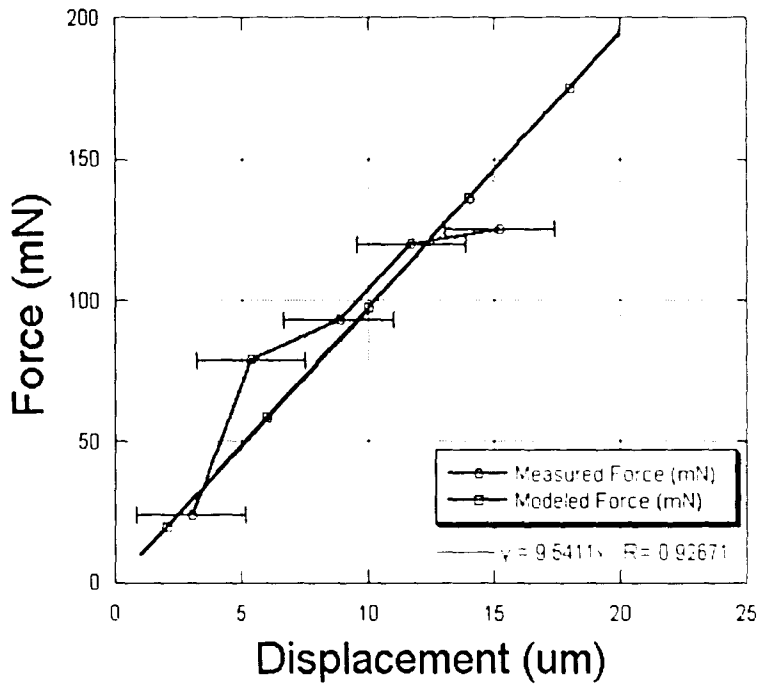

Figure 37 - Force vs. displacement, measured and modeled

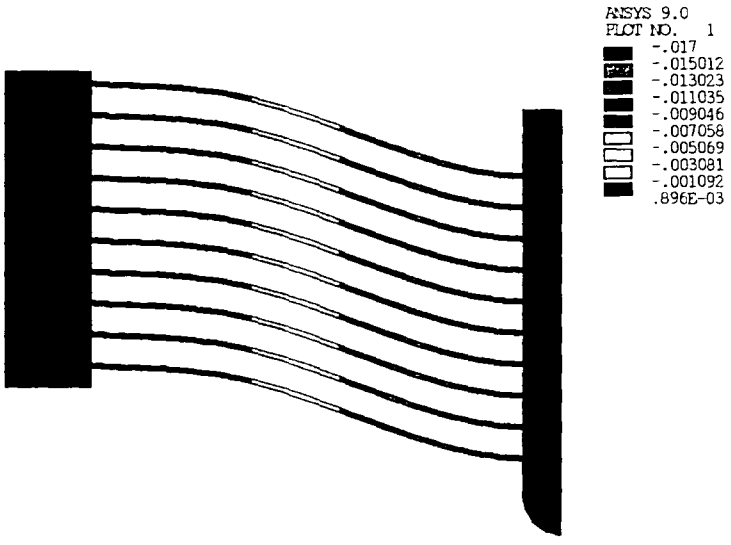

Figure 38 - Actuator modeled in ANSYS

Chapter 4
Novel design of a micro-aligner

4.1 Refining the Boeing IPMA design

Based on a review of the information presented in the previous chapters, there are many areas for improving the Boeing IPMA device. Three major areas for improvement are identified below.

A significant advantage is to be had by integrating a locking feature into an optical alignment device. As the literature review has shown, there are many different ways to use MEMS technology to achieve the small displacement, high accuracy alignment required by optical devices. Only one of these many devices, that by Syms et al.[15], demonstrates a lock-in-place mechanism as an intrinsic part of the device design. External fiber fixing mechanisms are subject to a small shift upon locking. Firsthand experience has revealed that many hours of development time and thousands of dollars of parts are spent characterizing the "post-weld-shift" of laserwelded alignments as well as the shift associated with epoxy or solder methods used to hold an aligned fiber in place. An intrinsic locking mechanism affords the opportunity to eliminate drift, and significantly decrease the time and cost of developing fiber-to-die interconnects.

Syms[15] demonstrates a minimum accuracy of alignment upon locking of 10um, certainly a long way from sub-micron tolerances required of waveguide alignment. It is

clear that there is ample room for improvement of integrated locking technology for optoelectronic applications. One of the concepts for an improved IPMA aligner includes an on-board locking mechanism, as will be discussed in a further section of this work.

The displacement range of the thermal actuators offers another opportunity to improve the Boeing IPMA device. The Y axis displacement of the cantilever beam on the IPMA is reported at 150um[30] and is probably sufficient to handle even the widest of alignment tolerance requirements. Based on the data included in this work, the X and Z axes are limited to a maximum displacement of 25um. The stack up of multiple tolerances in an optoelectronic package will likely require a minimum of 100um of displacement. If the IPMA concept could be modified to allow for a longer allowable displacement in the X and Z axes, a substantial benefit would be realized, greatly expanding the usefulness of the device. A concept for attaining this motion will be introduced in a further section of this work.

The last area considered where the IPMA design could be improved: cost and availability of manufacturing tools. The structural elements on the IPMA are fabricated using the LIGA process, as outlined in a previous section of this thesis. The LIGA process is capable of producing the high aspect ratio metal structures that give the actuators good mechanical stiffness and also a high coefficient of thermal expansion (CTE). Unfortunately, the availability of LIGA as a processing tool is limited. There are only a small handful of MEMS fabrication sites in the United States which posses the high energy Synchotron source required to create the masks used in the LIGA process.

The masks are also expensive. This researcher has been quoted mask fabrication costs in excess of $7,000 per mask.[31] An alternative fabrication technique to be described in this work has the potential to eliminate this mask, significantly lowering the development cost.

In comparison, the thermal evaporation of thin films of metal is an inexpensive and widely available tool and has been common to both the MEMS and semiconductor industries for decades. An actuator design fabricated using thin film metal deposition would significantly lower both the cost and availability barriers associated with LIGA. The author proposes that corrugated structures of thin film metal, similar in concept to the sidewall of a cardboard box, will provide adequate levels of stiffness to be used in place of the LIGA structures. A conceptual image of the cross section of a corrugated structure is seen in Figure 39. Two concepts are shown, the top concept is the simpler of the two, and lacks the top and bottom plate included on the bottom concept. Further details on the analysis, testing and development of these corrugated structures will be presented in another section of this work. Figure 40 shows a similar concept, presented in an isometric view as modeled by the author in SolidWorks.

Figure 39 - Conceptual image of cross section of corrugated structures

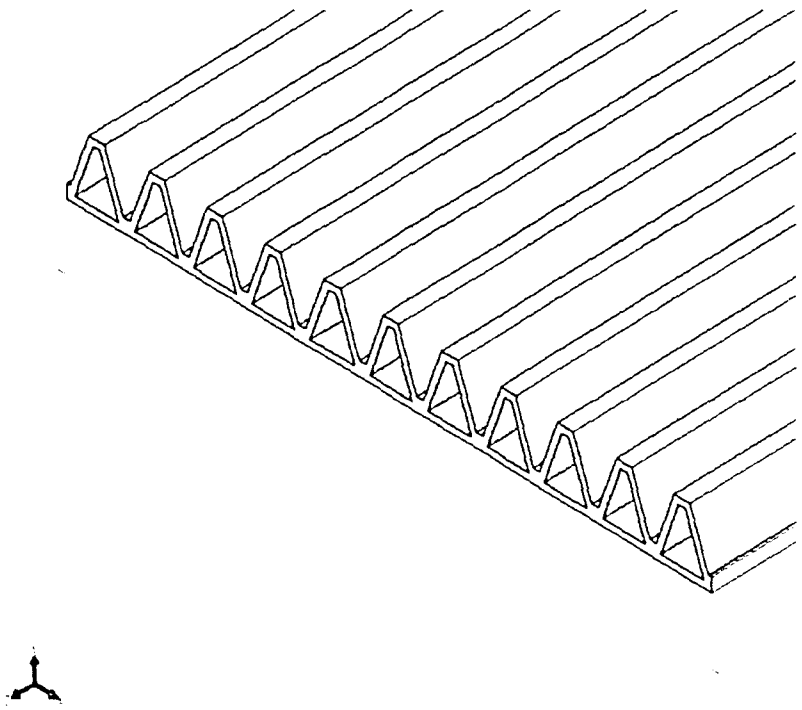

Figure 40 - Conceptual image of isometric view of a corrugated structure

4.2 Concept for thin film based aligner with integrated locking mechanism

The three improvements outlined in the previous section can be combined to realize a new actuator design for the X and Z axes of the Boeing IPMA device. This inchworm drive is fabricated from corrugated metal structures, and features an integrated locking mechanism and the potential for greater than 100um of displacement. A plan view of the inchworm drive is shown in Figure 41.

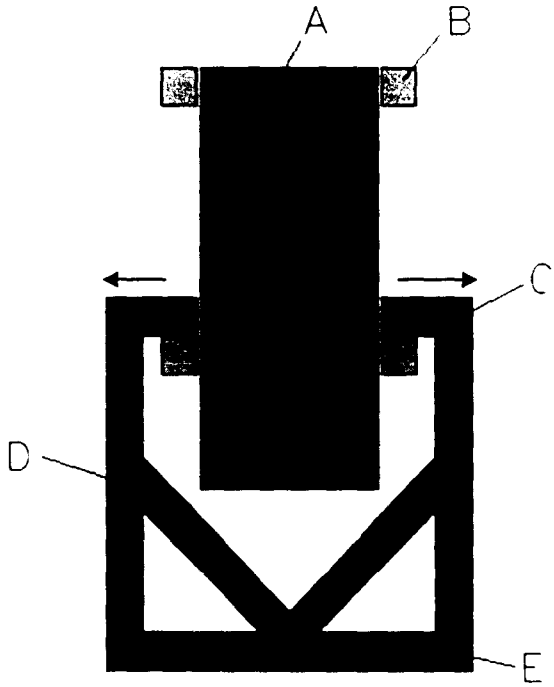

Figure 41 - Plan view of inchworm drive

The components of the inchworm drive are identified as the actuator beam (A), the beam guides (B), the actuator arms (C), the clamping arms (D) and the fixed anchor (E). The actuator beam is a completely free structure but is restricted by the beam guides which are attached to the substrate, allowing motion only in the vertical direction of the figure. The fixed anchor is also firmly attached to the substrate and serves to secure one end of both clamping beams and both actuator beams. These beams are otherwise free to move and are not attached to the underlying substrate. It is conceivable that all of the elements in the inchworm drive are made of the same corrugated thin film elements, as illustrated in Figure 42. The corrugations would be aligned with the direction of maximum stress in the beam as appropriate.

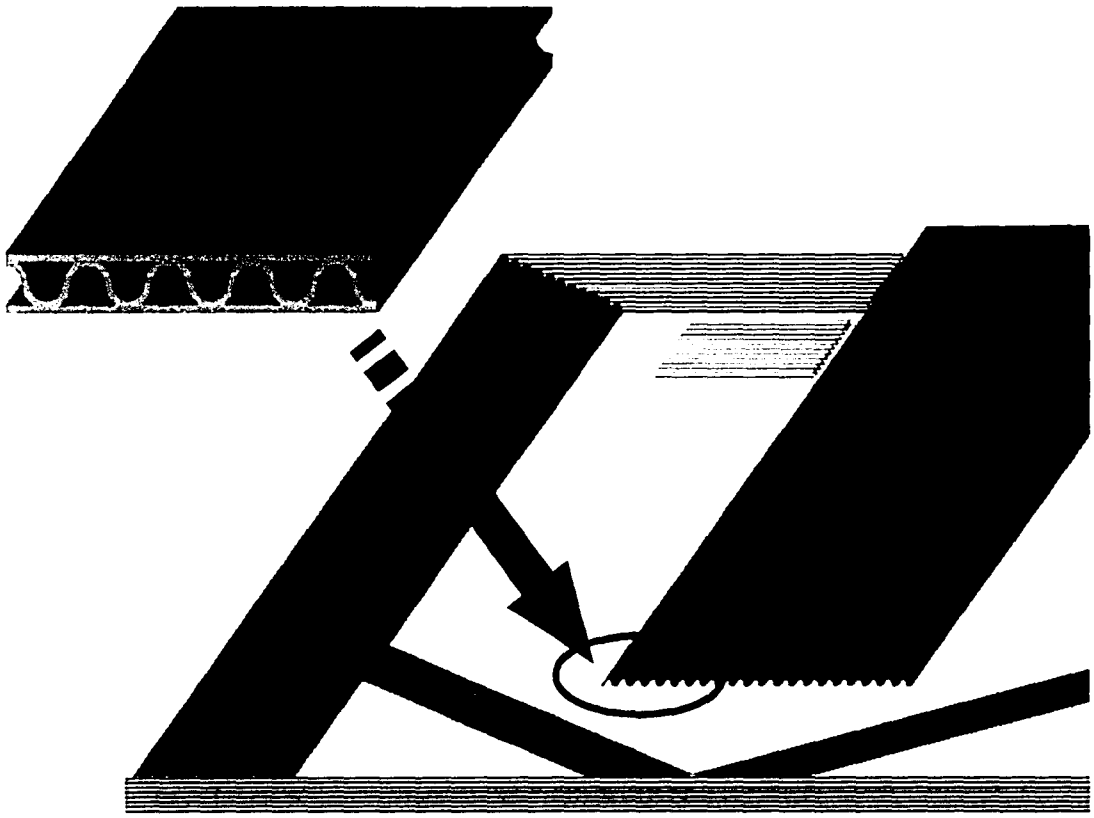

Figure 42 - The corrugated beams used in the inchworm drive

As it may not be apparent which parts of the motion engine are fixed and which move, the motion of the inchworm drive is illustrated in Figure 41, and a step-by-step description of the motion follows.

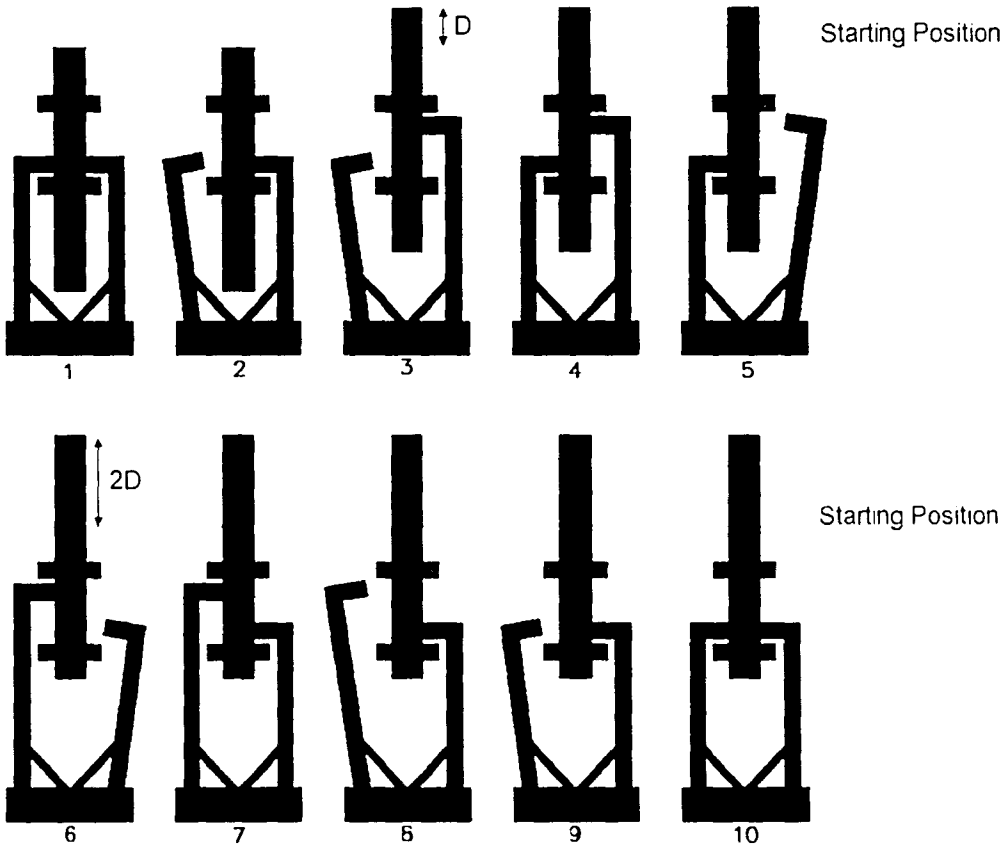

Figure 43 - Conceptual motion of inchworm drive

Both the actuator arms (C in Figure 41) and the clamping arms (D in Figure 41) are heated independently. Thermal expansion will cause these metal structures to expand when heated. Step 1 in Figure 43 shows the drive in an unpowered state. No heat is supplied to any of the arms, and the center actuator beam is locked in place by the actuator arms. In step 2, heat is applied to the left clamping arm, causing the left actuator arm to swing out and away from the actuator beam. In step 3, the right actuator arm is heated, and translates the center beam by a distance D. Step 4 shows the left actuator arm reclamping the center beam, fixing it in place while the right clamping arm is heated,

swinging the right actuator arm away in step 5. The left actuator arm is heated in step 6, causing another displacement of the center beam, for a total distance of 2D, while the right actuator arm retracts as it is no longer heated. Step 7 shows the effect of removing the heat source from the right clamping arm: the beam is fixed in position again, allowing the left actuator arm to retract as is shown in steps 8-9 as heat is supplied to the clamping arm, and then removed from the actuator arm. Finally, heat is removed from the left clamping arm in step 10. The inchworm drive is in an unpowered state after translating the center beam by a distance of 2D. The amount of deflection attainable by such a drive is limited only by the length of the actuator beam, and it is not difficult to see that deflections of 100+ microns are possible.

Further modeling of the motion of the inchworm drive beyond the conceptual level is of considerable interest to the research team, but is beyond the scope of the material presented in this work[32]. The balance of this work will focus on the modeling, fabrication and testing of corrugated thin film structures. Two methods of fabrication are described, mechanical embossing and grayscale lithography.

Chapter 5
Fabrication and Testing of Corrugated Structures

5.1 Embossing a corrugated thin film structure

The first corrugated structures were fabricated using a mechanical embossing technique. A thick coat of photoresist (more than 25 microns) was spun onto a 3" diameter silicon wafer, and then imprinted with a pattern from a mandrel. The pattern is selectively deposited with a thin film of metal, and is then carefully lifted off of the resist for testing. An illustration of the mandrel about to emboss a silicon wafer is shown below in Figure 44, where PR is an abbreviation for photoresist. This illustration is to aid understanding of the concept, and the mandrel is not shown to scale. The fabrication of the mandrel was quite a challenging task, and is the topic of the next section.

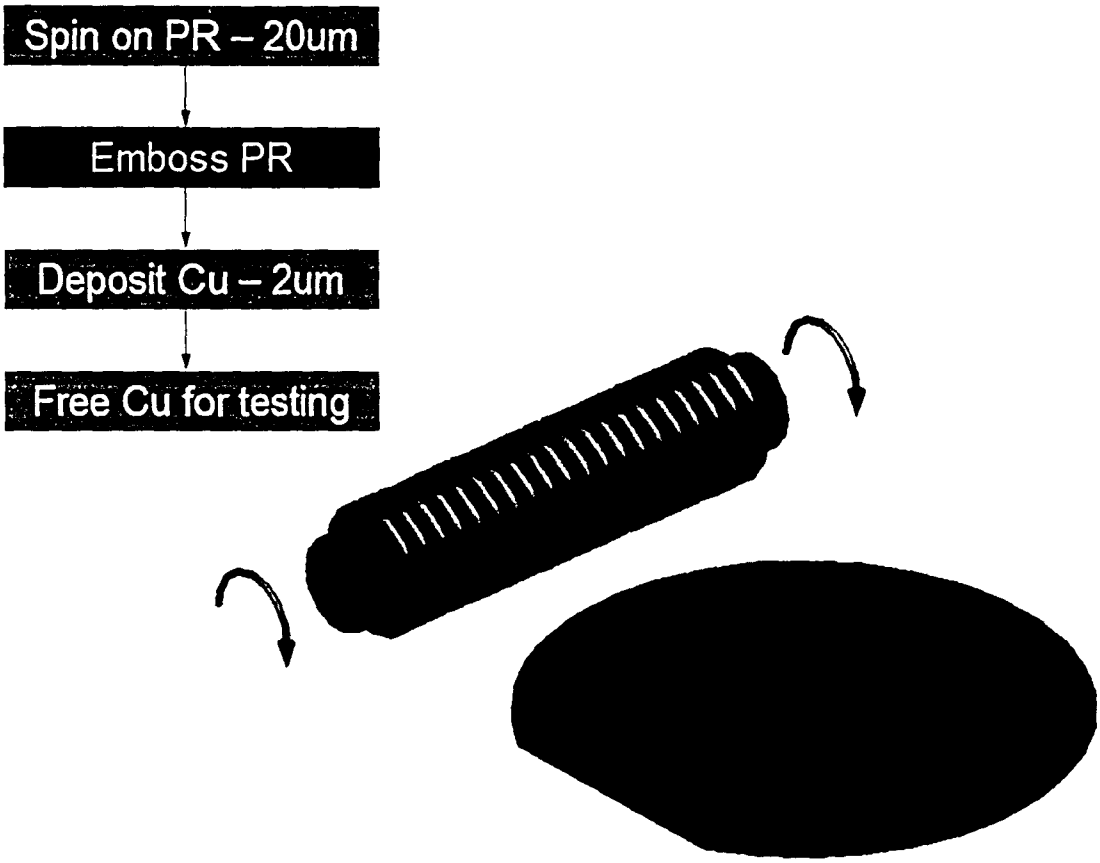

Figure 44 - Concept image of embossing process

5.1.1 Fabrication of tools

The first attempts to fabricate a mandrel were unsuccessful. The embossing surface of the mandrel machined per the print below (Figure 45) was not sharp enough to be of any use. This approach was abandoned for a more complicated but ultimately more successful embossing method.

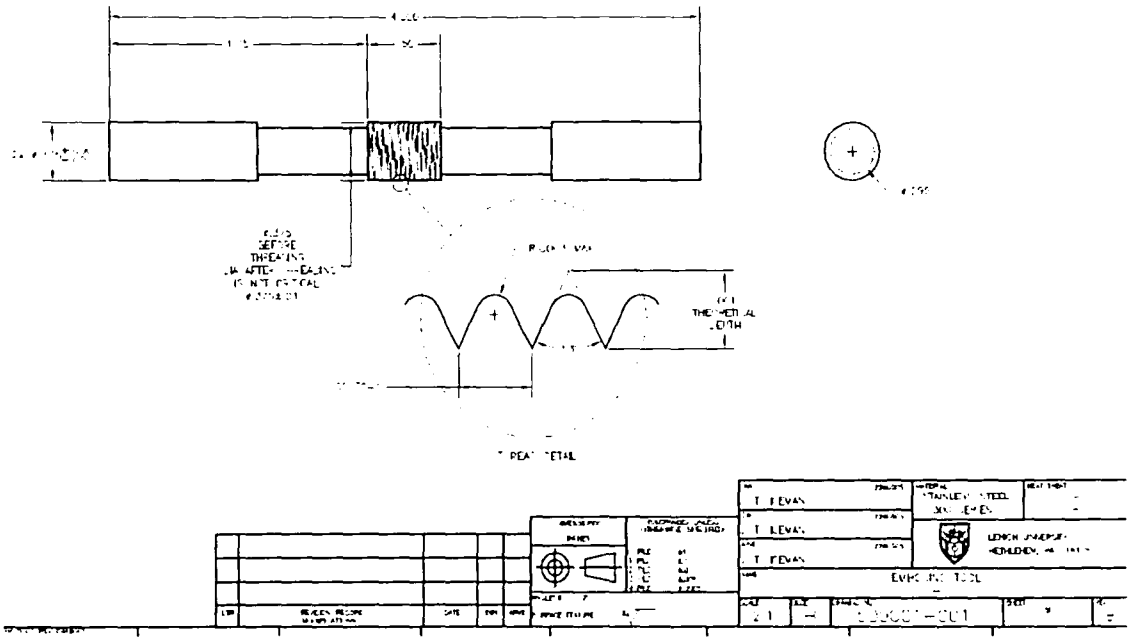

Figure 45 - Machined mandrel print

The second generation mandrel is a 0.375" diameter stainless steel rod, 4" long. It is wound with 0.0010" diameter thermocouple wire on a 0.0017" pitch. The thermocouple wire was available off the shelf from Omega Corp. in spools of 250'. Top and profile views of the mandrel follow as Figure 46 and Figure 47 respectively. In Figure 46 the vertical lines are the thermocouple wire, and the texture that runs horizontally across the picture is the surface of the stainless steel. The profile view in Figure 47 clearly shows the core of the mandrel in the upper half of the photo, and the thermocouple wire can be seen as a horizontal line of circles. Both pictures show a slight irregularity of pitch in the windings.

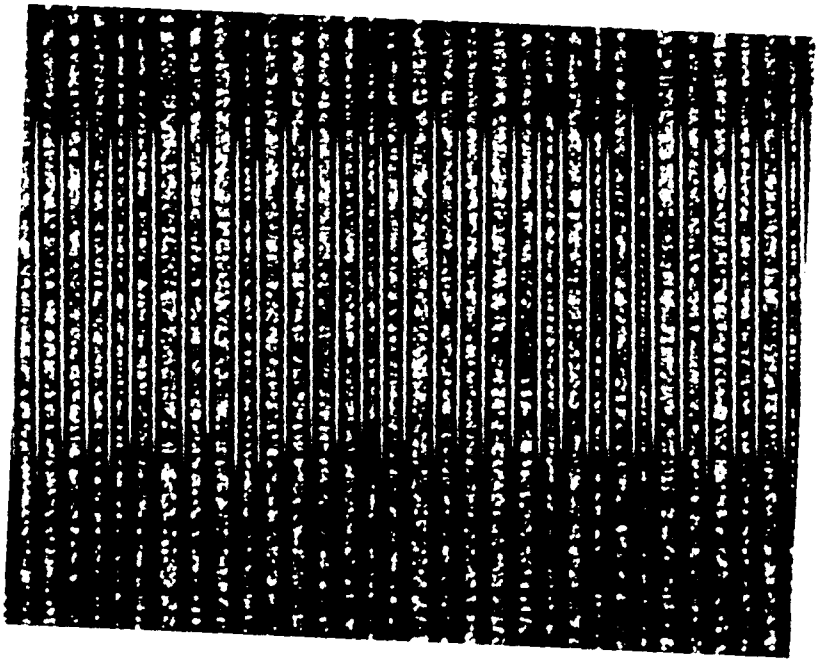

Figure 46 - Top view of wire-wound mandrel

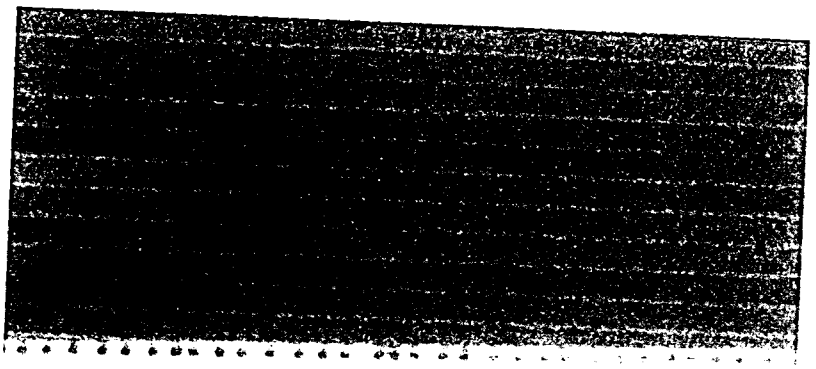

Figure 47 - Profile view of wire-wound mandrel

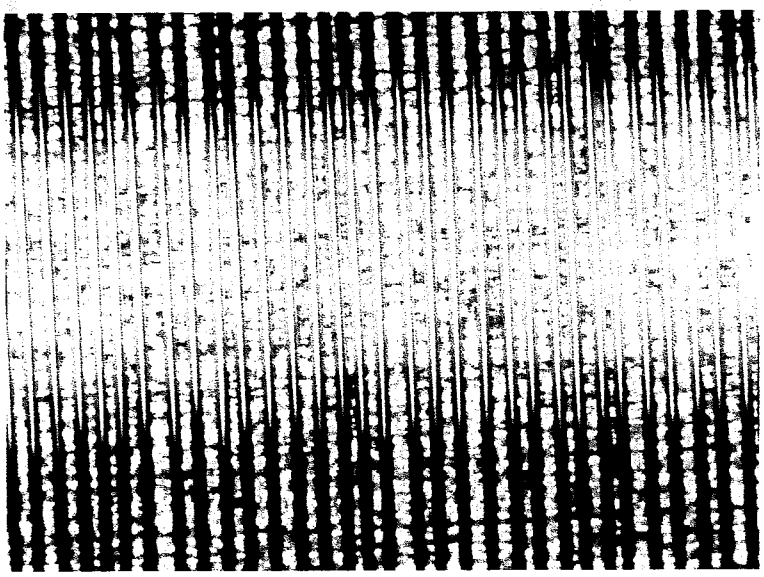

Figure 46 - Top view of wire-wound mandrel

Figure 47 - Profile view of wire-wound mandrel

The thermocouple wire was wound onto the mandrel using a winding jig and an engine lathe. The winding jig is shown below in Figure 48. The winding jig operates as follows: the spool of wire (A) is hung from a hook (B) attached to the tool holder (C). The wire on the spool is fed through a brass guide tube (D) and into a loop of Teflon tubing (E). The Teflon tubing acts as a tensioner on the wire; the tension is controlled by adjusting the diameter of the loop. The Teflon tubing takes the wire into a hypodermic needle (F), the tip of which is placed very close to the rotating mandrel.

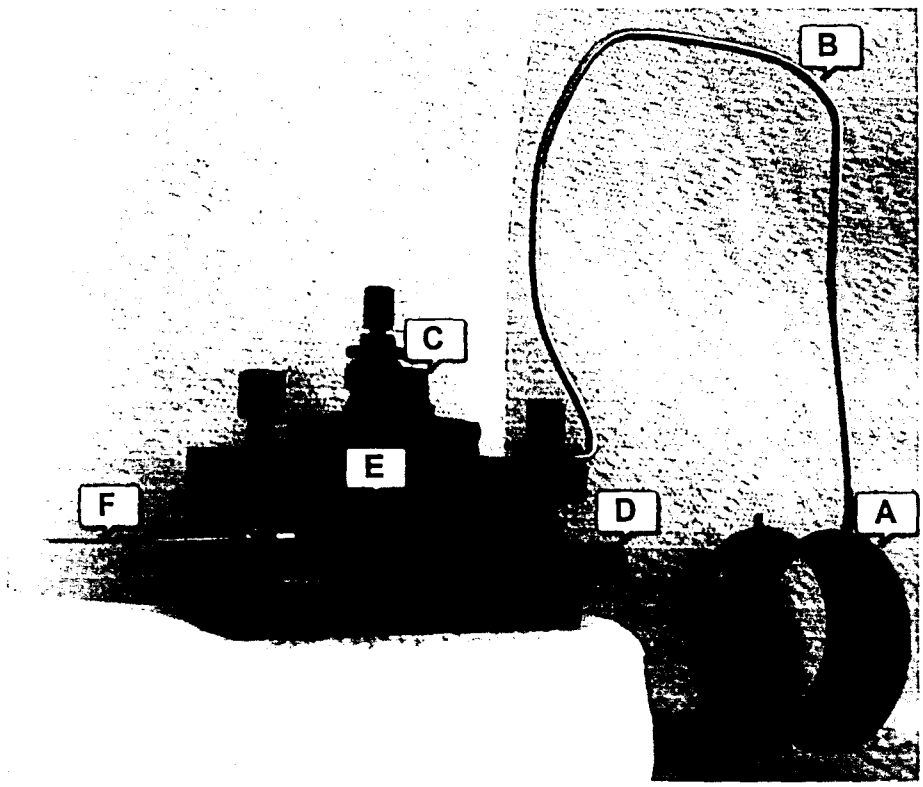

Figure 48 - Photo of mandrel winding tool

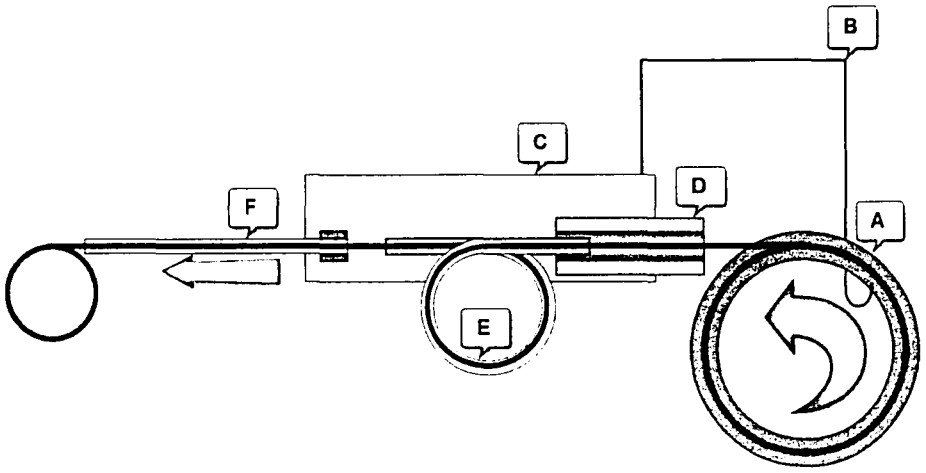

Figure 49 - Block diagram of mandrel winding tool

The engine lathe was run at the lowest possible speed, 56 rpm, to ensure as regular a winding as possible. The irregularity in the spacing of the windings seen in Figure 46 and Figure 47 is attributed to wear on the feed mechanism of the lathe. A photograph of the mandrel during the winding process is shown in Figure 50. The mandrel is identified by the letter (G).

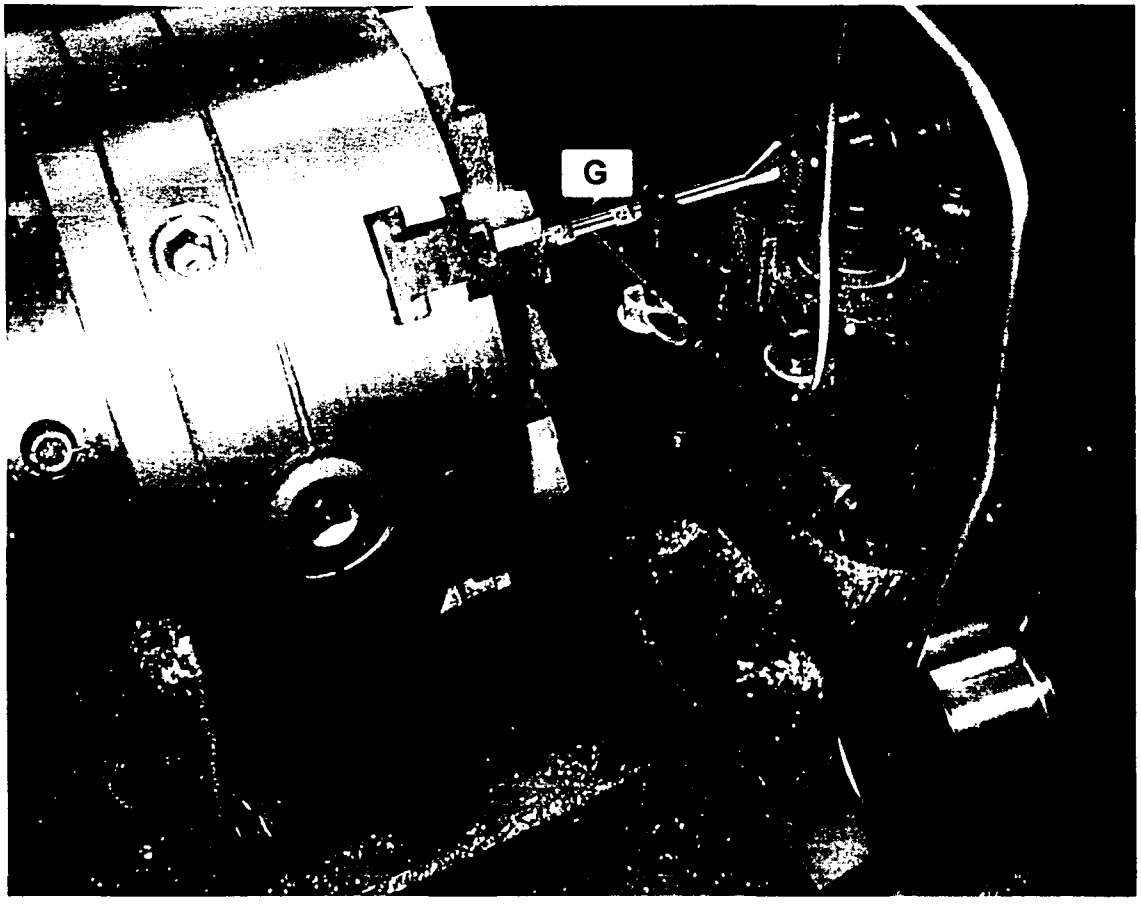

Figure 50 - Photo of mandrel during winding

5.1.2 Substrate information

3" Diameter silicon wafers spin coated with Clariant AZ 4620 resist were used as the substrate to be embossed. The resist was spun at 1000 rpm for 60 seconds yielding a thickness of 30um. based on information provided in the data sheet by the manufacturer.

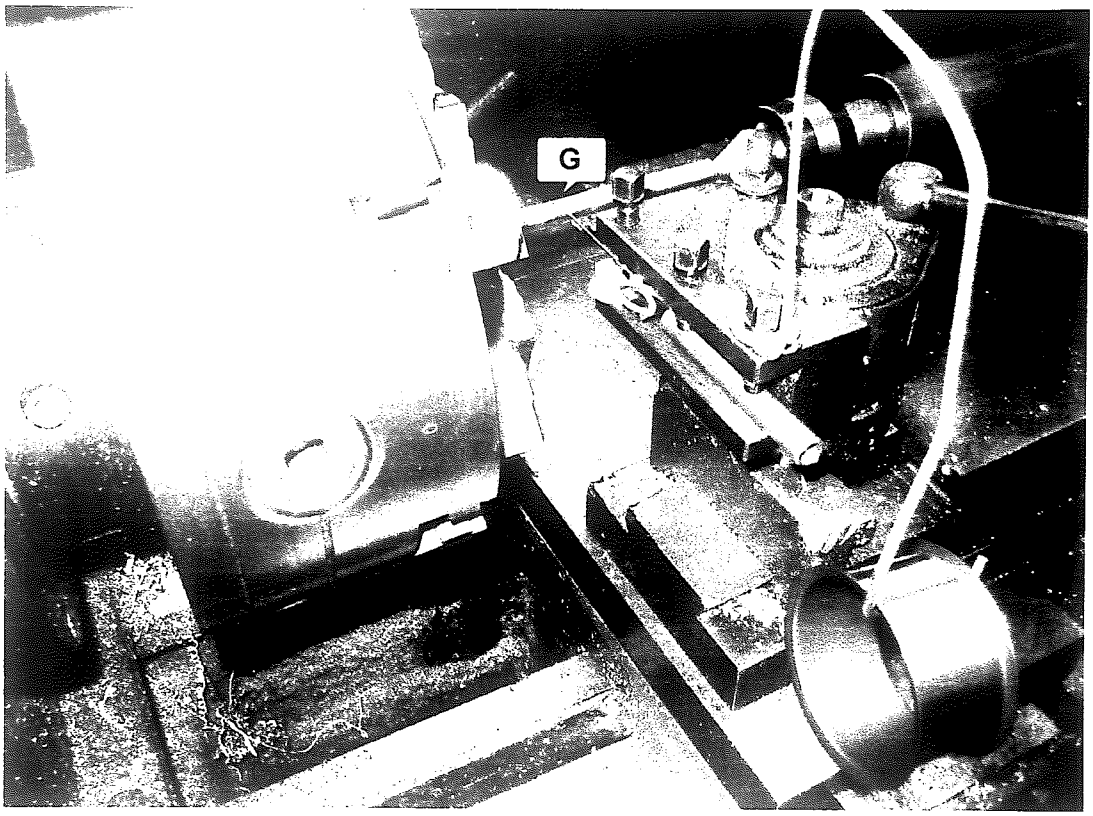

Figure 50 - Photo of mandrel during winding

5.1.2 Substrate information

3" Diameter silicon wafers spin coated with Clariant AZ 4620 resist were used as the substrate to be embossed. The resist was spun at 1000 rpm for 60 seconds yielding a thickness of 30um. based on information provided in the data sheet by the manufacturer.

Note that it is critical to avoid a post-spin bake, which caused large cracks in the surface of the resist after embossing.

The coated wafer was then manually cleaved into rectangular chunks approximately ½" wide and 1.5" long for embossing.

5.1.3 Embossing methodology

Embossing was performed in a Bridgeport milling machine. Figure 51 shows the embossing fixture and samples placed in the milling machine. The simple three axis adjustability and automatic feed were found to be a considerable aid to the embossing process. A conceptual diagram of the embossing fixturing is shown in Figure 52 and a photograph of the same is shown in Figure 53.

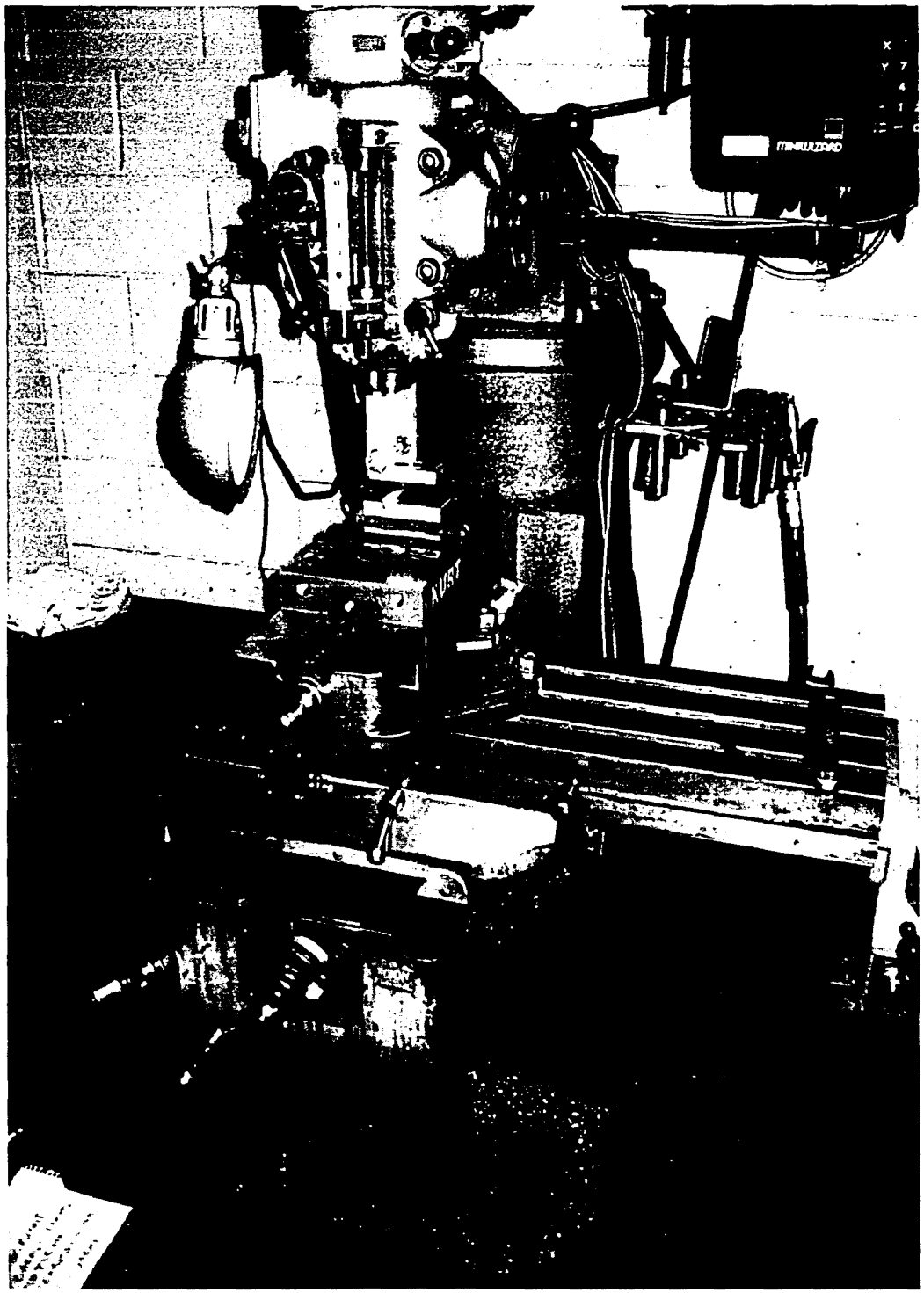

Figure 51 - Photo of Bridgeport milling machine used for mechanical embossing

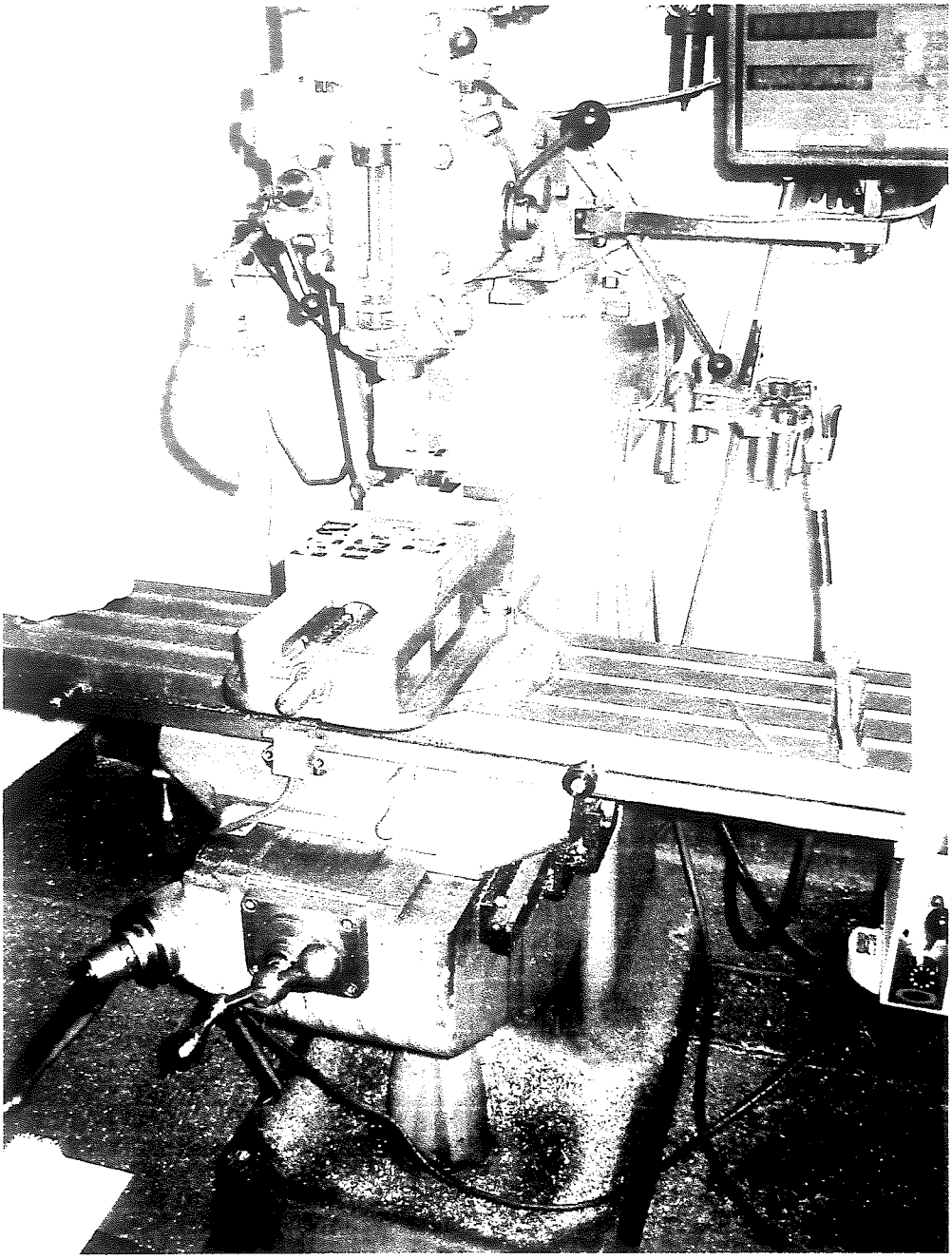

Figure 51 - Photo of Bridgeport milling machine used for mechanical embossing

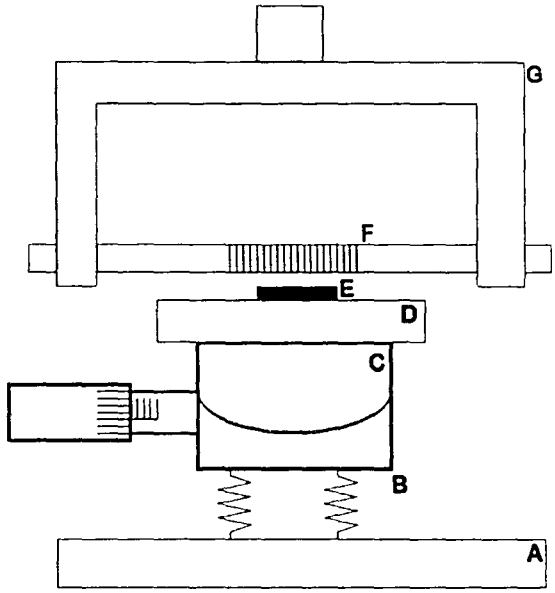

Figure 52 - Conceptual diagram of embossing fixturing

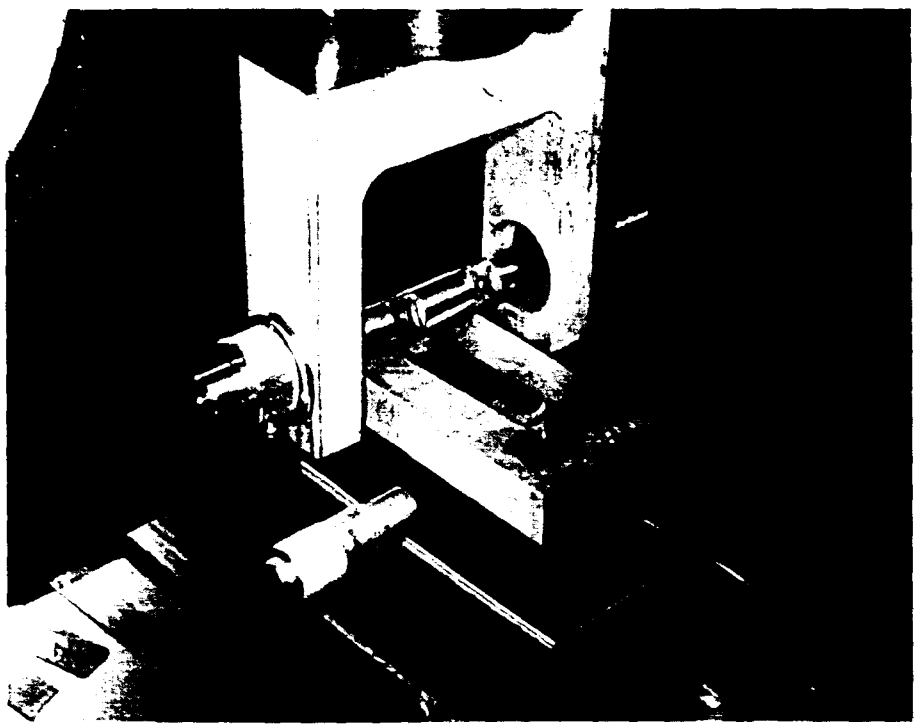

Figure 53 - Photo of embossing fixturing

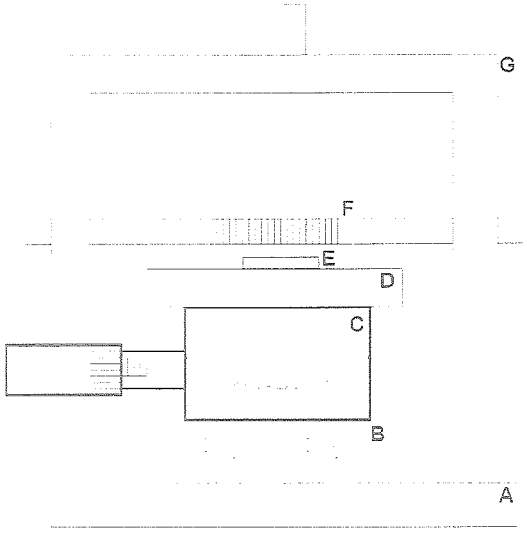

Figure 52 - Conceptual diagram of embossing fixturing

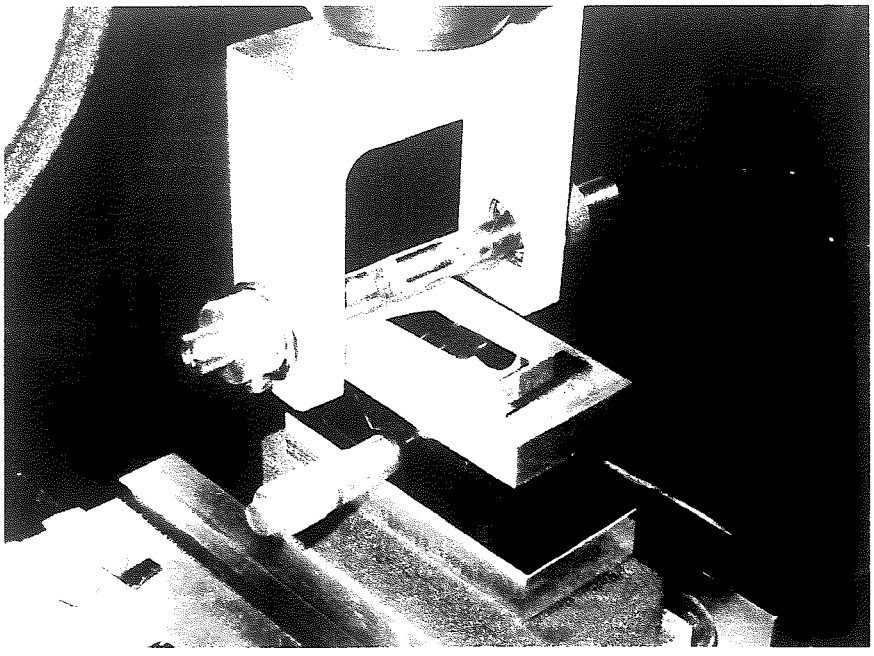

Figure 53 - Photo of embossing fixturing

The embossing fixturing is comprised of several components, with the assistance of Dr. Walter Brown. The base of the fixturing (A) is clamped in the vice jaws of the Bridgeport. The black foam spring (B) gives mechanical compliance in the vertical direction during the embossing process. The goniometer (C) allows the top plate (D) and the embossing specimen (E) to be adjusted parallel to the mandrel (F). The mandrel is held in the drill chuck of the Bridgeport using a yoke (G). The mandrel is supported by ball bearings to minimize friction.

The embossing sequence begins by placing the sample on the top plate. The yoke is then lowered until the mandrel contacts the sample, as determined by eye using a 10x magnification. Once first contact is achieved the mandrel is lowered an additional 0.050", compressing the black foam and achieving a force suitable for embossing but not sufficient to remove the resist from the substrate. The automatic feed on the Bridgeport table is then engaged at the lowest speed, approximately 0.001" per second until the end of the substrate is reached. A number of embossed samples are shown in Figure 54. A microscopic view of an embossed sample is shown as Figure 55. Note that the narrow lines are the indentations of the wire into the resist. It is also interesting to note the presence of a bubble where the resist as become unadhered from the silicon substrate.

Figure 54 - Samples after embossing

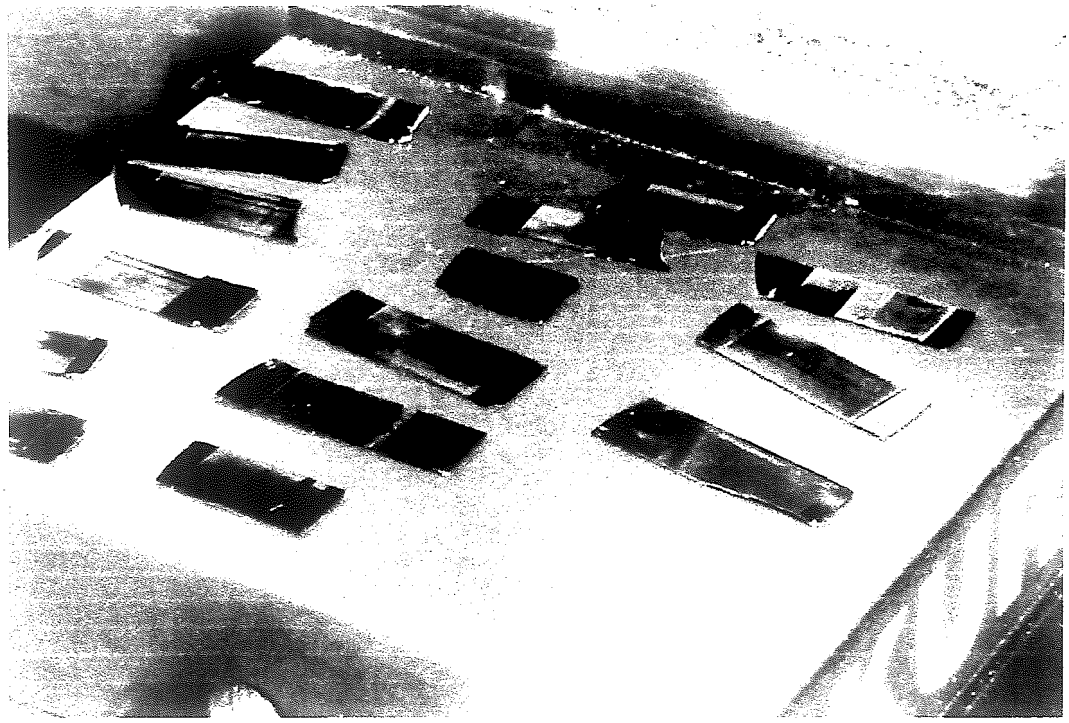

Figure 54 - Samples after embossing

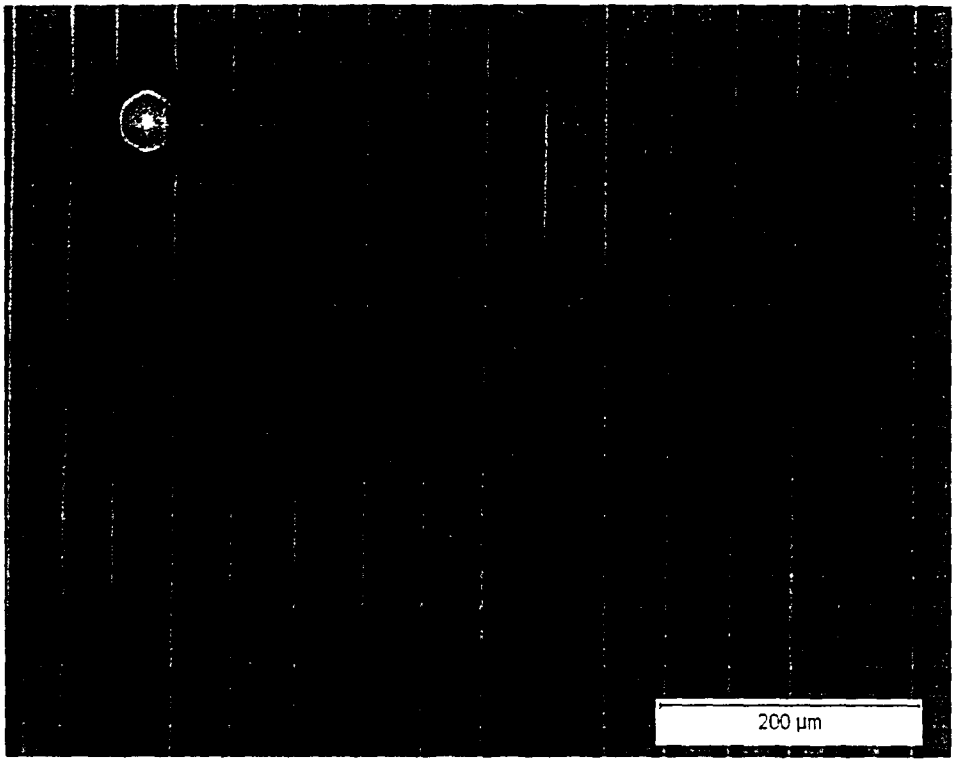

Figure 55 - Microscopic view of embossed sample

5.1.4 Metal deposition and imaging of embossed structures

After embossing, samples were partially covered with a silicon mask, and placed into a thermal evaporation chamber. This is illustrated in Figure 56 below. The substrate is shown as A, the embossed resist as B and the mask as item C. The opening in the mask through which the metal will be deposited is shown as D. A uniform coat of metal is illustrated schematically in Figure 57.

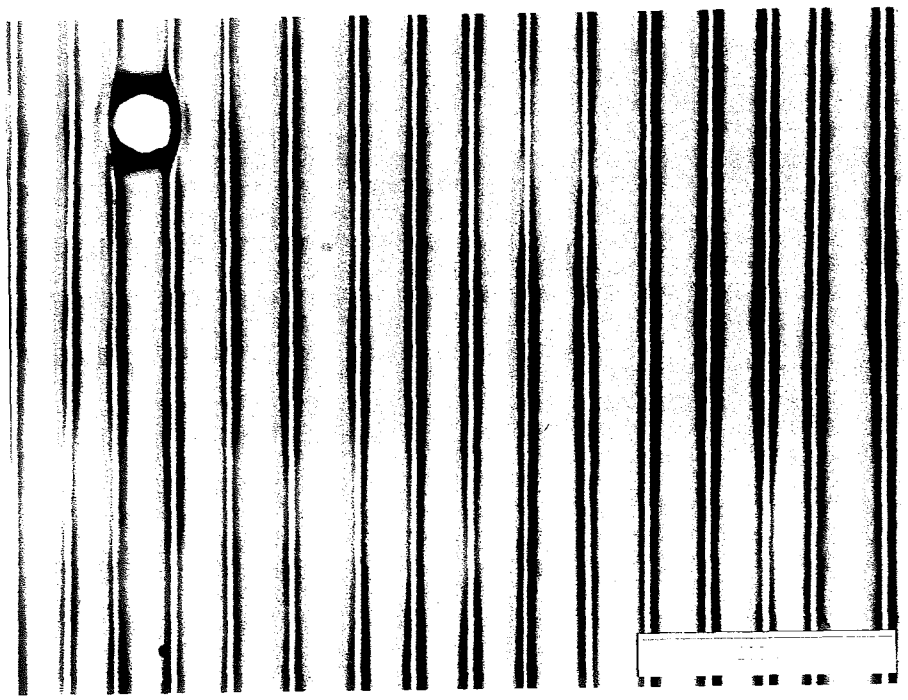

Figure 55 - Microscopic view of embossed sample

5.1.4 Metal deposition and imaging of embossed structures

After embossing, samples were partially covered with a silicon mask, and placed into a thermal evaporation chamber. This is illustrated in Figure 56 below. The substrate is shown as A, the embossed resist as B and the mask as item C. The opening in the mask through which the metal will be deposited is shown as D. A uniform coat of metal is illustrated schematically in Figure 57.

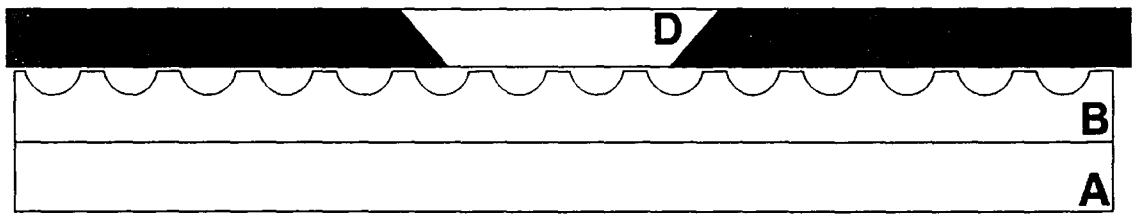

Figure 56 - Mask on top of corrugations

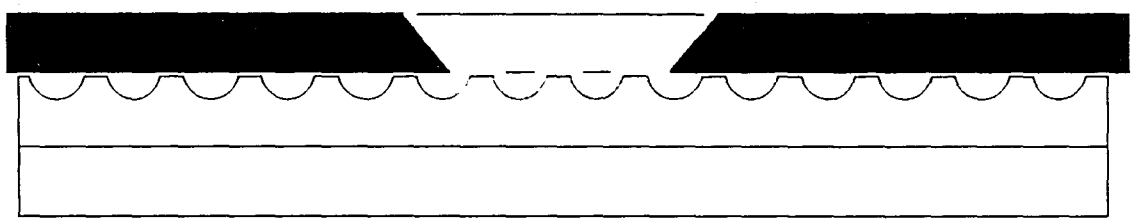

Figure 57 - After metal deposition

Two mask opening sizes were used in the deposition, 2mm x 12mm and 3mm x 12mm. The evaporator was loaded with a charge of 50 grams of 99.995% pure copper and substrates selectively covered with masks as shown in Figure 56. The chamber was then pumped to a vacuum of less than 5 x 10^{-7} torr. The copper was evaporated by passing a current of 450A through the tungsten boat holding the copper slugs.After deposition, samples were available for cross-sections and feature study, or for removal from the substrate for mechanical testing. A part after deposition is shown in Figure 58 as seen through an optical microscope. The band across the top of the picture is the resist

that was covered with the silicon mask during deposition. The copper film is clearly seen occupying the bottom 90% of the photo.

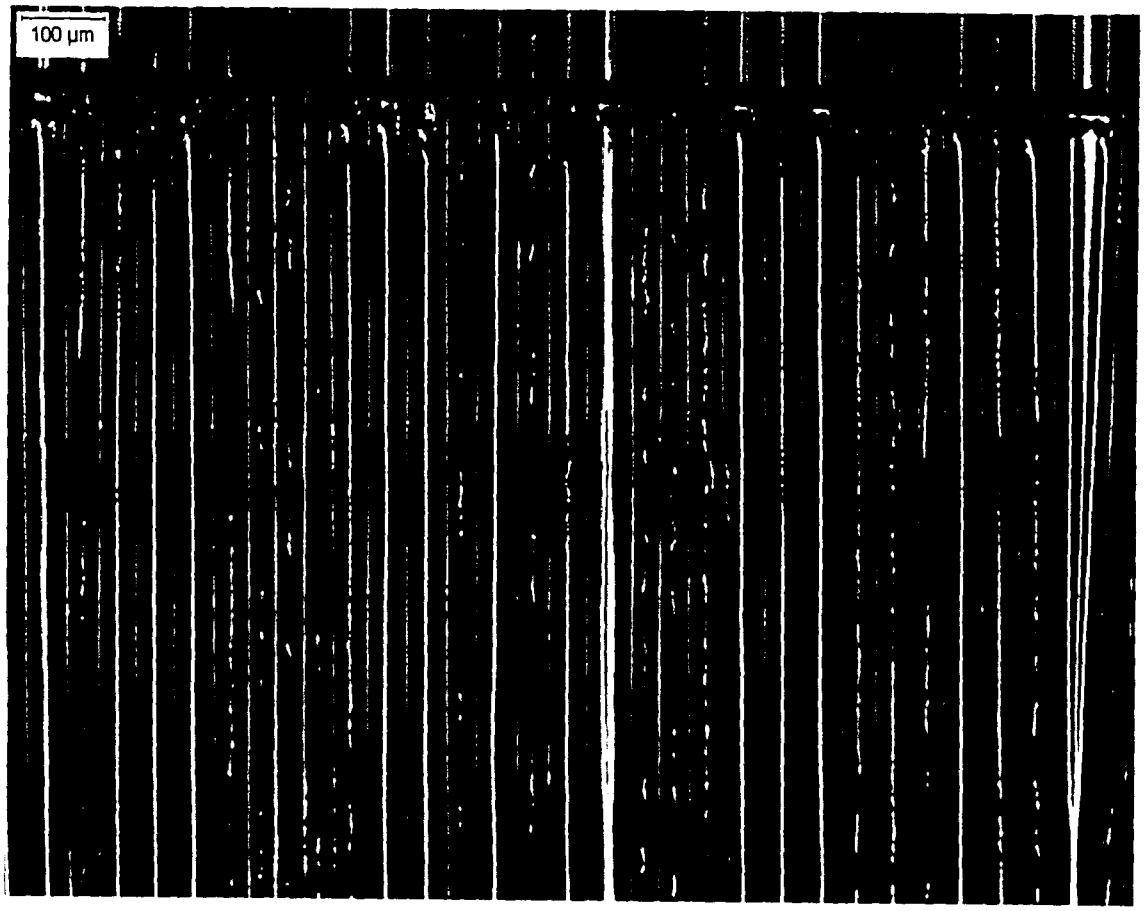

Figure 58 - Optical micrograph of embossed sample after deposition

The cross-section of a representative part is shown below in Figure 59. This part was cut with a diamond saw, and then mounted in Buehler Epoxide® and polished at 340, 420, 600, 800, 1200, and 2400 grit, followed by 6um diamond and 1um diamond.

The resulting structure is somewhat regular, but far from perfect. The white band along the bottom of the optical micrograph is the silicon substrate, and above that is the

that was covered with the silicon mask during deposition. The copper film is clearly seen occupying the bottom 90% of the photo.

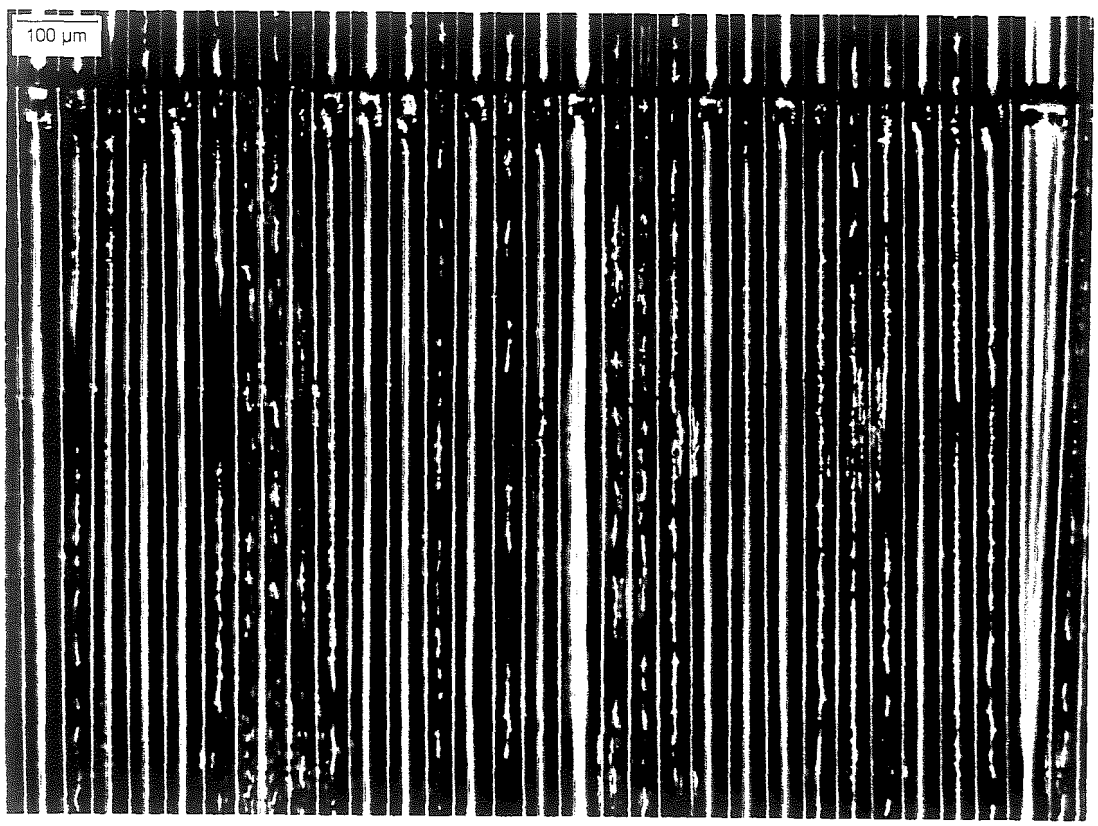

Figure 58 - Optical micrograph of embossed sample after deposition

The cross-section of a representative part is shown below in Figure 59. This part was cut with a diamond saw, and then mounted in Buehler Epoxide® and polished at 340, 420, 600, 800, 1200, and 2400 grit, followed by 6um diamond and 1um diamond.

The resulting structure is somewhat regular, but far from perfect. The white band along the bottom of the optical micrograph is the silicon substrate, and above that is the

darker layer of resist. The copper film is seen as a white wavy band, and the epoxide mount is the black region above the copper.

Figure 59 – Cross-section of embossed structure

The information in this micrograph was traced in Adobe Illustrator and then exported to dxf format, which allowed feature sizes to be directly measured in AutoCAD. Figure 60 shows the exported micrograph data (in black) and the trace performed in AutoCAD (in red.). According to the cad export, the structures had an average pitch of 35-50um and a height of 8-16um.

Figure 60 - Micrograph data imported to CAD

The cross-section optical micrograph shows the topology of the copper film well, but only hints at what the surface of the film might look like. SEM provides more

insight, and in this case clearly shows cracking on the top surface of an embossed specimen (Figure 61 and Figure 62). While mechanical embossing may be a low cost, low tech way to create corrugated parts, the irregularity of the topology and the presence of surface cracks indicate that a more refined method is required to achieve suitable results.

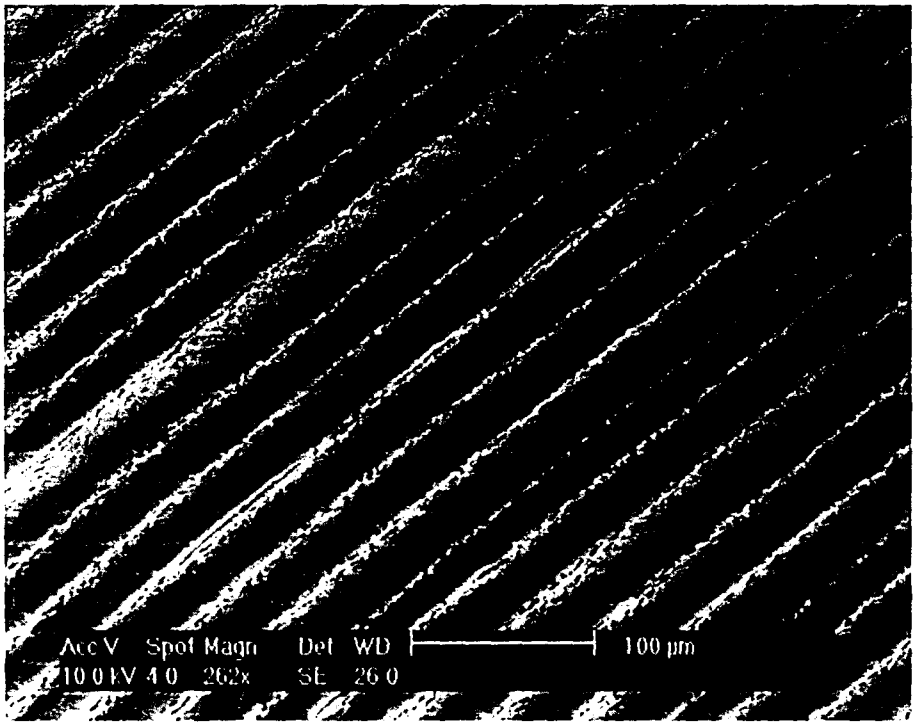

Figure 61 – Lower mag SEM Image of embossed structure

insight, and in this case clearly shows cracking on the top surface of an embossed specimen (Figure 61 and Figure 62). While mechanical embossing may be a low cost, low tech way to create corrugated parts, the irregularity of the topology and the presence of surface cracks indicate that a more refined method is required to achieve suitable results.

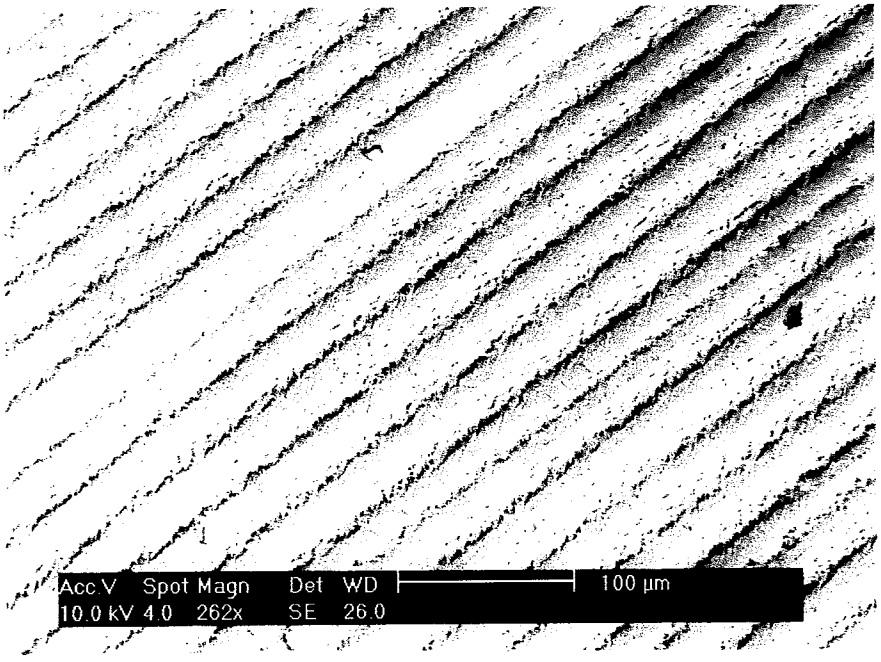

Figure 61 – Lower mag SEM Image of embossed structure

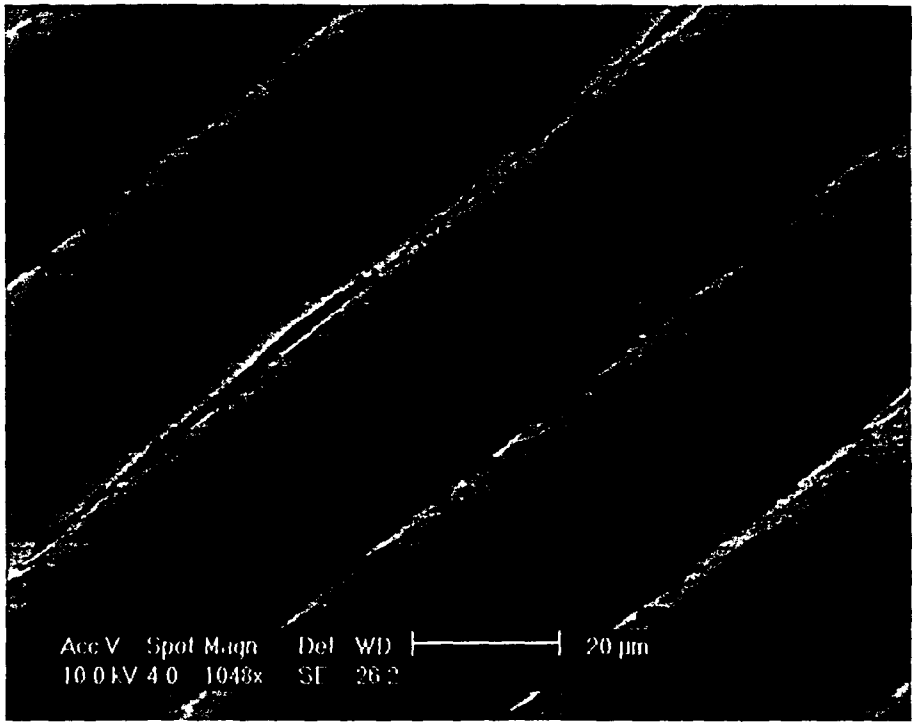

Figure 62 - Higher mag SEM image of embossed structure

5.2 Using grayscale lithography to create 3D structures

Grayscale lithography has previously been used to create microlenses in a quartz substrate[33]. The lens shown below as Figure 63 has a height of 2.7um and a diameter at the base of 90um. This device was fabricated using a Heidelberg Instruments DWL 66 pattern generator. This system modulates a 442nm laser source to achieve 31 different intensity levels, where level 1 is barely exposed, and level 31 is a full power exposure. The greater the intensity of the laser source, the deeper the penetration of the exposure in the resist so that 3D structures can be achieved.

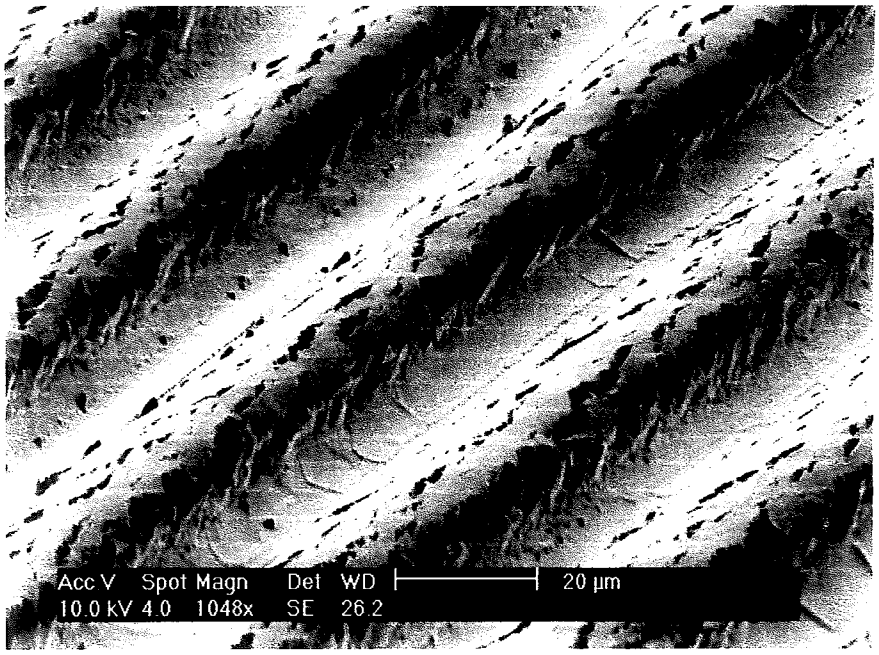

Figure 62 - Higher mag SEM image of embossed structure

5.2 Using grayscale lithography to create 3D structures

Grayscale lithography has previously been used to create microlenses in a quartz substrate[33]. The lens shown below as Figure 63 has a height of 2.7um and a diameter at the base of 90um. This device was fabricated using a Heidelberg Instruments DWL 66 pattern generator. This system modulates a 442nm laser source to achieve 31 different intensity levels, where level 1 is barely exposed, and level 31 is a full power exposure. The greater the intensity of the laser source, the deeper the penetration of the exposure in the resist so that 3D structures can be achieved.

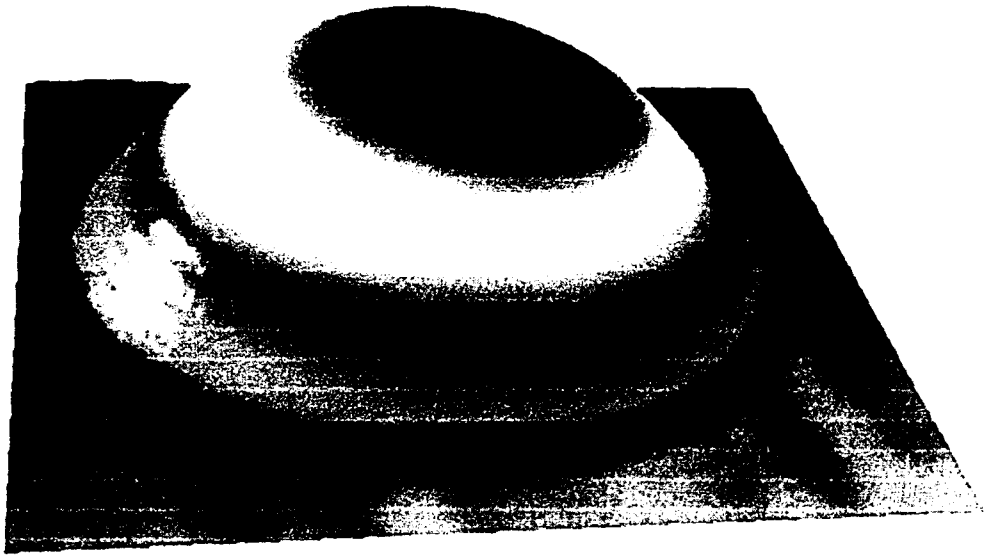

Figure 63 - Lens fabricated with grayscale lithography[33]

As will be demonstrated, the author used the Heidelberg DWL 66 tool available at the Penn State University Nanofab to create corrugated patterns in resist similar to those achieved by mechanical embossing.

5.2.1 Grayscale substrate information

Test grade silicon wafers 0.017"-0.020" thick were used as a substrate. These wafers were coated with a Shipley 220-7 resist on a programmable resist spinner. No adhesion promoter was used. The resist was statically deposited on the substrate, and then the substrate was accelerated at a rate of 100 rpm/sec to 1000 rpm and held at that velocity for 40 seconds. The wafer was decelerated at a rate of 100 rpm / second and then soft baked to the following schedule on three hotplates:

Step No.	Hotplate No.	Temp.	Time
1	Hotplate 1	90°C	1 minute
2	Hotplate 2	100°C	1 minute
3	Hotplate 3	110°C	2 minutes
4	Hotplate 2	100°C	1 minute
5	Hotplate 1	90°C	1 minute

Table 2 - Shipley 220-7 softbake schedule

This process resulted in resist thickness consistently in excess of 27um and occasionally in excess of 30um as measured on the Alpha-Step 500 surface profile tool also located in the Penn State Nanofab Facility.

5.2.2 Mask design and greyscale resist fabrication.

The response of the exposed and developed resist is not linear with the amount of exposure. The purpose of the first mask was to create a long series of "steps" used to understand the response of the resist. A picture of the mask, the developed resist and the profile of the structure is shown below in Figure 64.

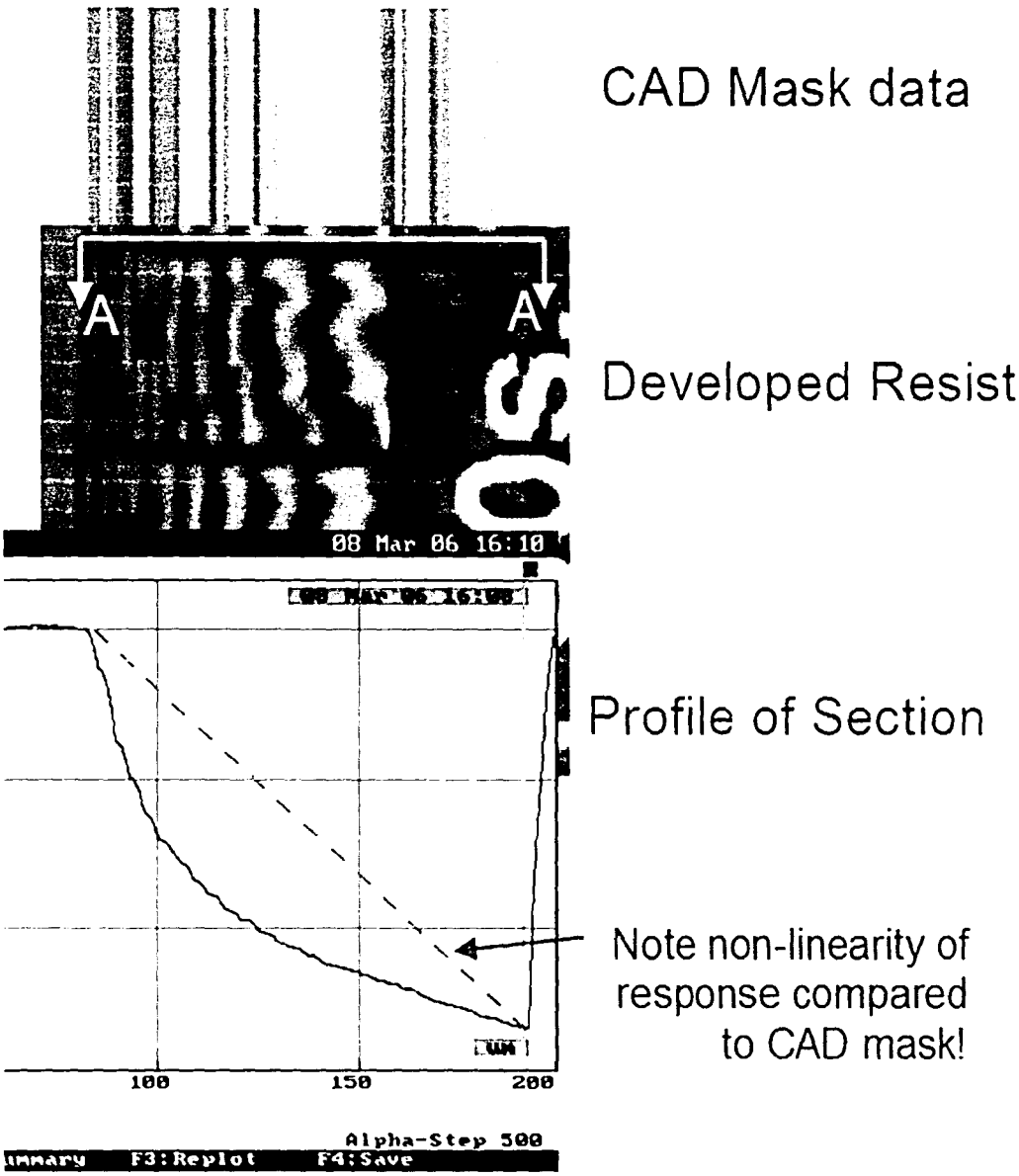

Figure 64 - Comparison of mask to profile

The contrast between the regular steps in the mask and the final structure is plain to see. This behavior was taken into account in the final mask design, a portion of which is shown below as Figure 65. The mask was generated in AutoCAD, and is relatively simple to lay out. This mask is designed to yield a topology with a broad flat top and base, and relatively steep sloping sidewalls. The mask structure in its entirety as a series

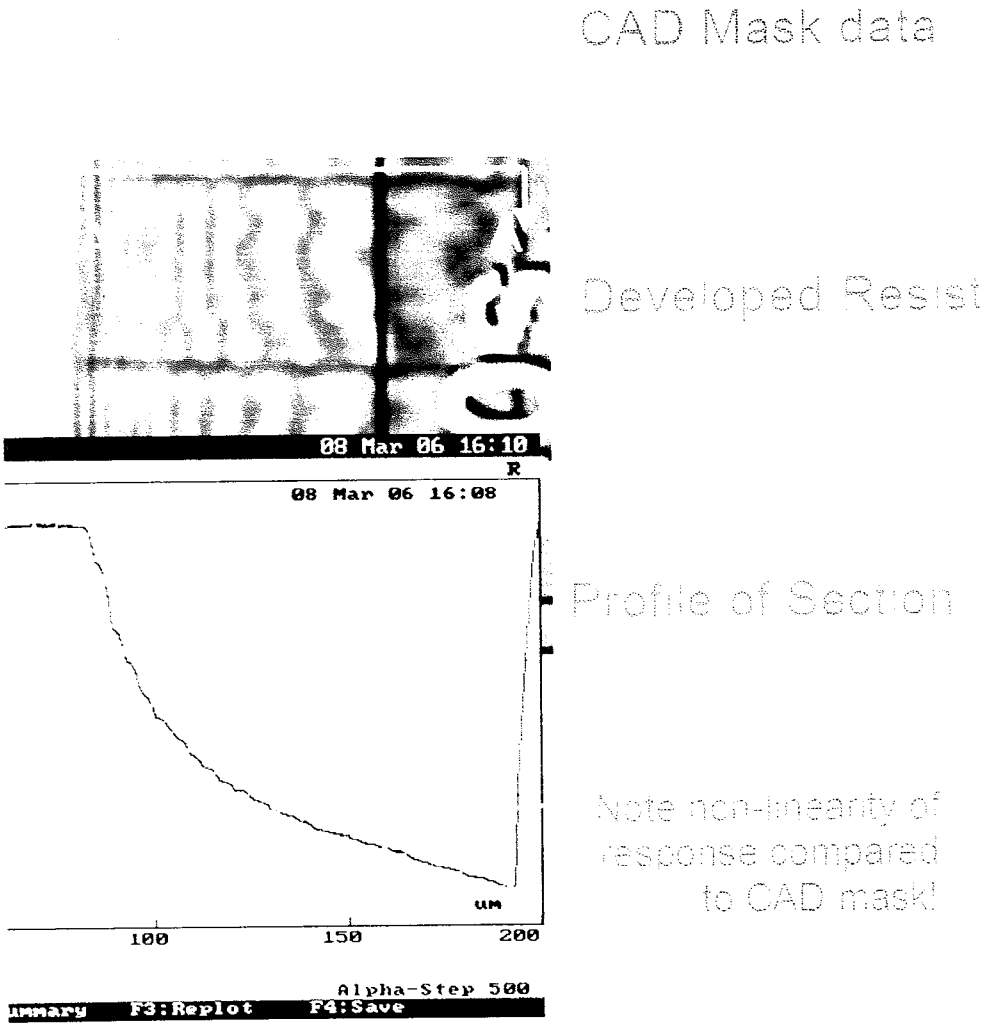

Figure 64 - Comparison of mask to profile

The contrast between the regular steps in the mask and the final structure is plain to see. This behavior was taken into account in the final mask design, a portion of which is shown below as Figure 65. The mask was generated in AutoCAD, and is relatively simple to lay out. This mask is designed to yield a topology with a broad flat top and base, and relatively steep sloping sidewalls. The mask structure in its entirety as a series

of repetitions is shown as Figure 66. The area of the structure to be written is 5mm x 15mm, considerably larger than the size of the openings in the silicon deposition masks.

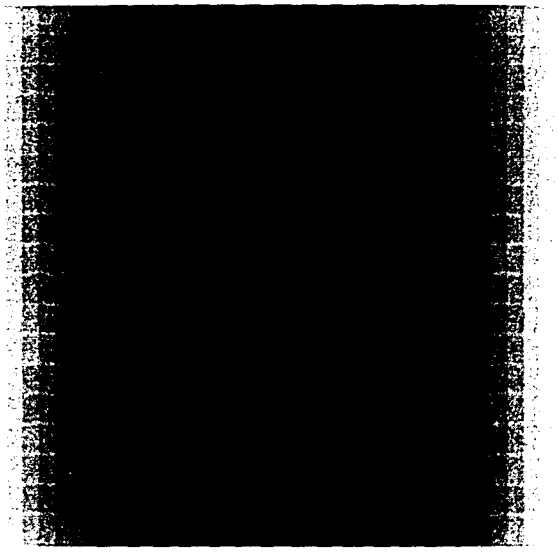

Figure 65 - Mask information for Nanofab structures

of repetitions is shown as Figure 66. The area of the structure to be written is 5mm x 15mm, considerably larger than the size of the openings in the silicon deposition masks.

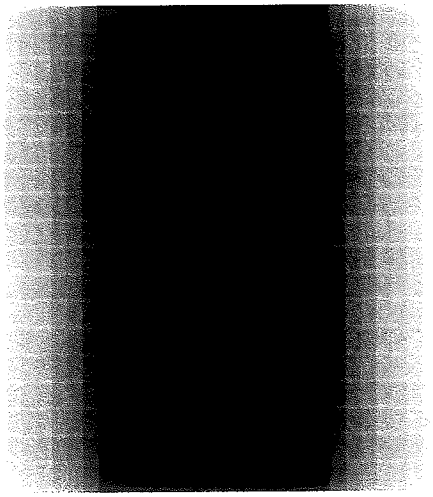

Figure 65 - Mask information for Nanofab structures

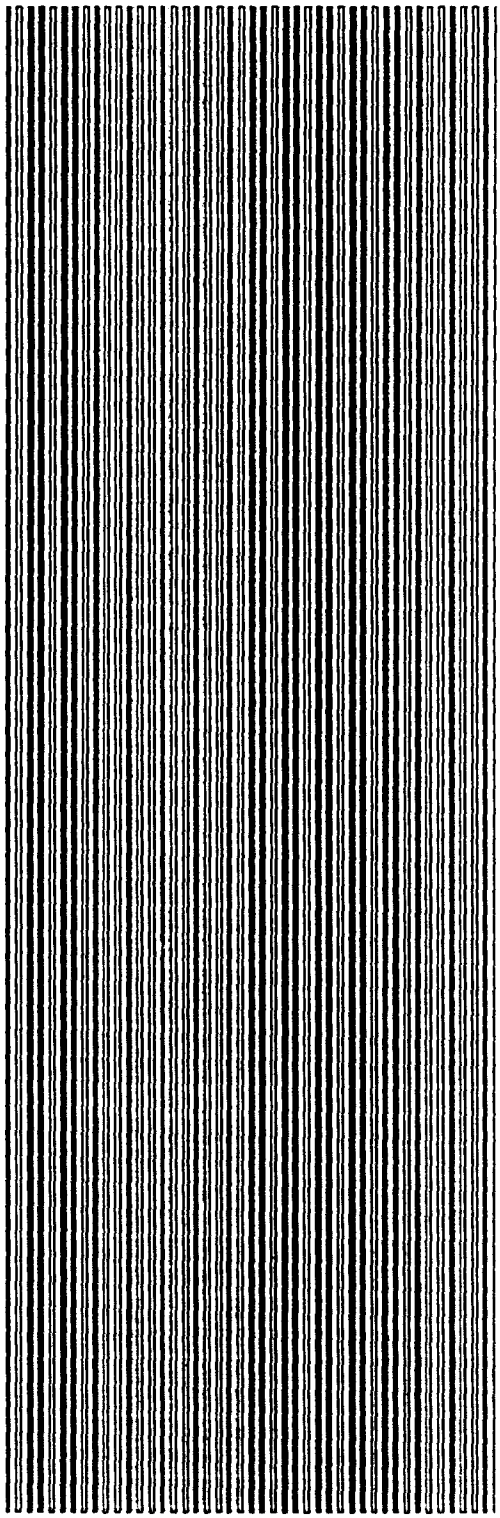

Figure 66 - Entire CAD mask

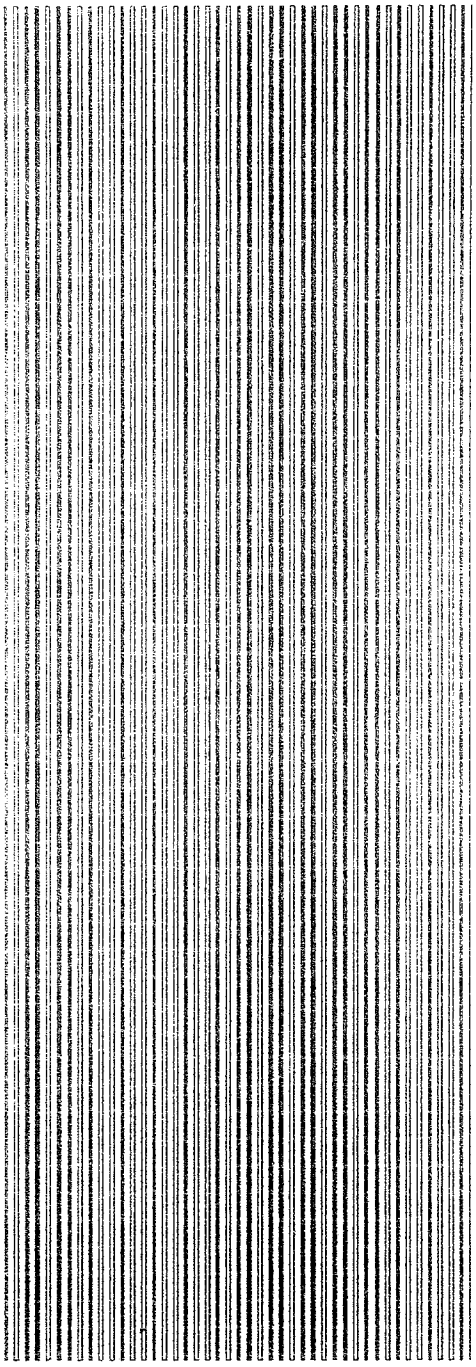

Figure 66 - Entire CAD mask

After the mask was written into the resist using the Heidelberg DWL 66 tool at the Penn State Nanofabrication Facility, the wafers were developed in MF-CD-26 for 4 minutes.

5.2.3 Metal deposition and imaging of grayscale structures

The metal deposition for the grayscale substrates was carried out in the same manner as the deposition for the embossed substrates. A silicon mask was set in contact with the corrugated substrate, and copper was thermally evaporated onto the substrate through the opening in the mask. Following deposition, samples were reserved for cross sectioning or mechanical testing.

All of the cross section samples were cut with a diamond saw, potted in a Buehler Epoxide mount, and prepared on an Apropol automatic polisher according to the schedule in Table 3. Specimens were examined with a light optical microscope.

Step No. (-)	Grit (-)	Wheel speed (RPM)	Time (sec.)	Pressure (PSI)
1	340	300	45	40
2	420	300	60	40
3	600	300	60	40
4	800	300	60	40
5	1200	300	60	40
6	2400	300	60	40
7	6um diamond	150	60	43
8	1um diamond	150	60	43

Table 3 - Polishing steps for XC sample preparation

Cross sectional views of one of the samples fabricated are shown as Figure 67 and Figure 68. In Figure 67, the white section at the bottom of the mount is the silicon wafer, the dark band immediately above the silicon is the patterned photoresist. On top of the resist is a thin band of copper, and above the copper is the epoxy mount material.

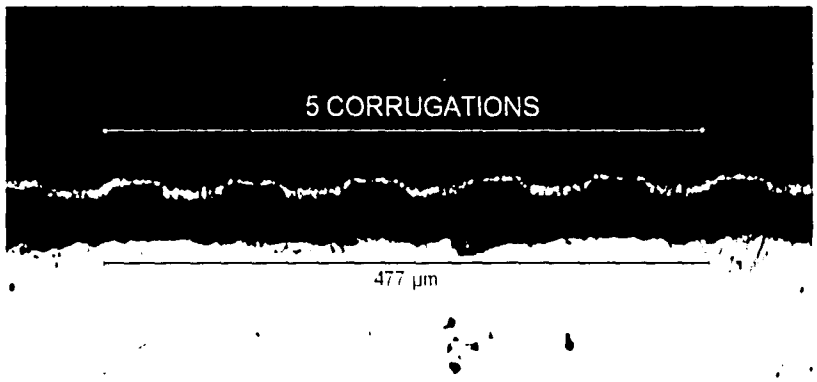

Figure 67 - Cross section of corrugated structure fabricated by the author.

Cross sectional views of one of the samples fabricated are shown as Figure 67 and Figure 68. In Figure 67, the white section at the bottom of the mount is the silicon wafer, the dark band immediately above the silicon is the patterned photoresist. On top of the resist is a thin band of copper, and above the copper is the epoxy mount material.

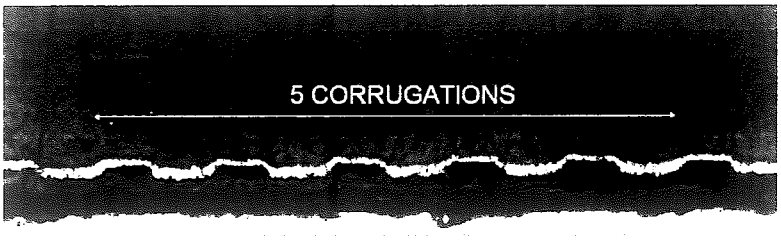

Figure 67 - Cross section of corrugated structure fabricated by the author.

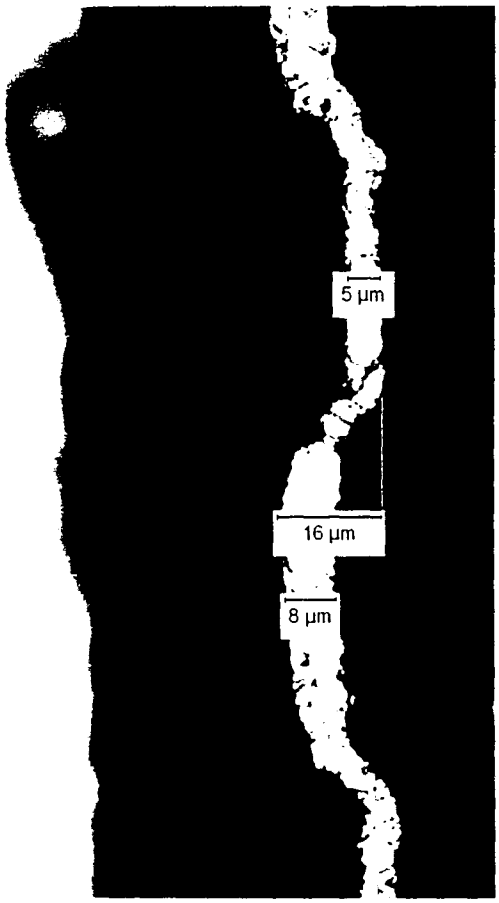

Figure 68 - Cross section of corrugated structure fabricated by the author.

A cross section of one of the samples fabricated at Penn State is shown as Figure 67 and Figure 68. Examination with a calibrated light optical microscope reveals that the structure has a pitch of 95.4um, a step height of 16um, and material thicknesses at the plateau and valley of 5um and 8um respectively. An SEM image of a sample fabricated from the same wafer gives a better feel for the topology of the structure along the axis of the corrugations. Figure 69 shows the edge of a sample: the copper is visible in white, the bare resist in black.

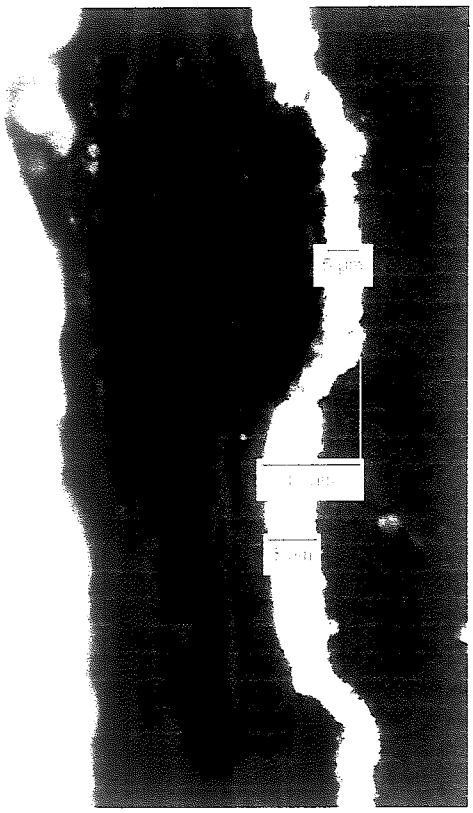

Figure 68 - Cross section of corrugated structure fabricated by the author.

A cross section of one of the samples fabricated at Penn State is shown as Figure 67 and Figure 68. Examination with a calibrated light optical microscope reveals that the structure has a pitch of 95.4um, a step height of 16um, and material thicknesses at the plateau and valley of 5um and 8um respectively. An SEM image of a sample fabricated from the same wafer gives a better feel for the topology of the structure along the axis of the corrugations. Figure 69 shows the edge of a sample: the copper is visible in white, the bare resist in black.

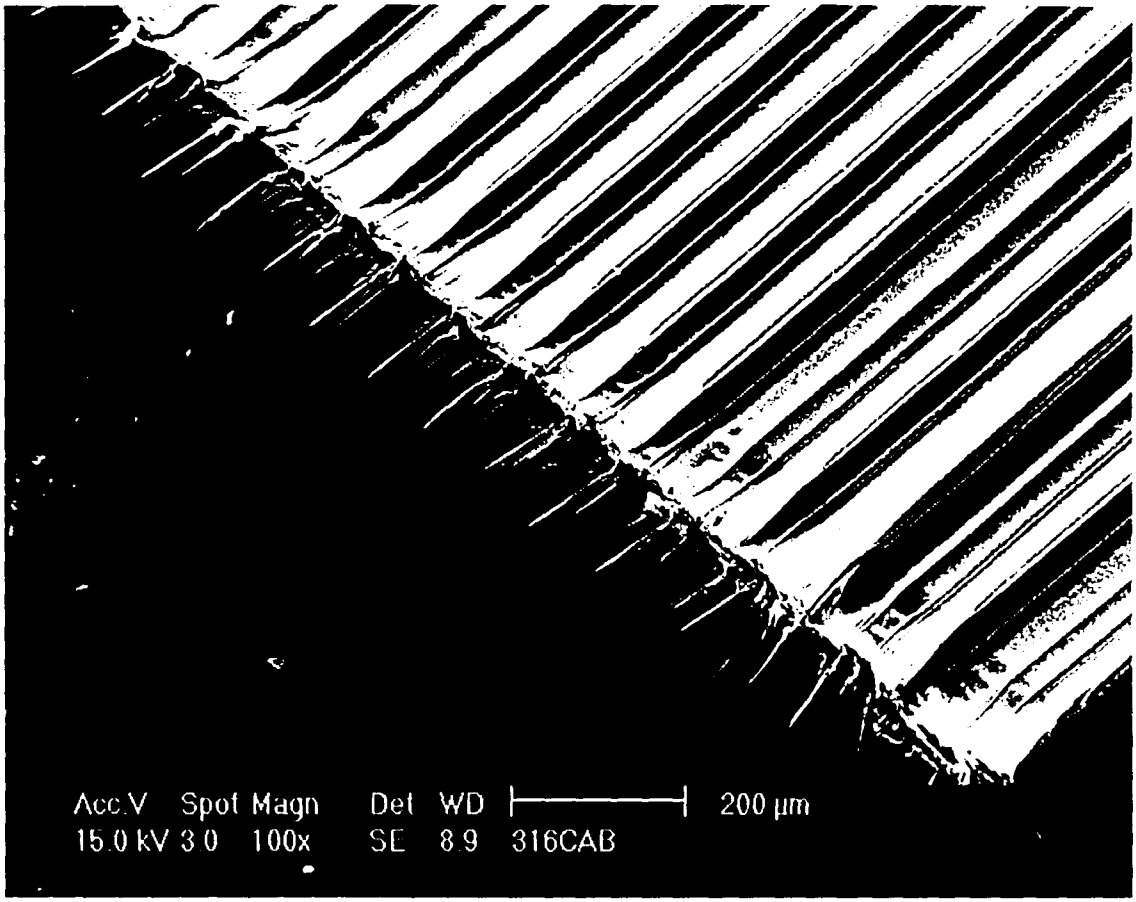

Figure 69 - SEM image of corrugated structure fabricated by the author.

In addition to the substrates created by the author, Heidelberg Instuments Mikrotechnik GmbH. of Heidelberg, Germany provided a number of substrates with a slightly different topology. This topology is visible in Figure 70 and Figure 71. Heidelberg provided wafers with a thick coat of patterned, developed resist. The resist used was AZ 4562 and was spun on to a thickness of 30um. After exposure, the parts were developed for 20 minutes.

Metal deposition was performed at Lehigh University in a thermal evaporator.

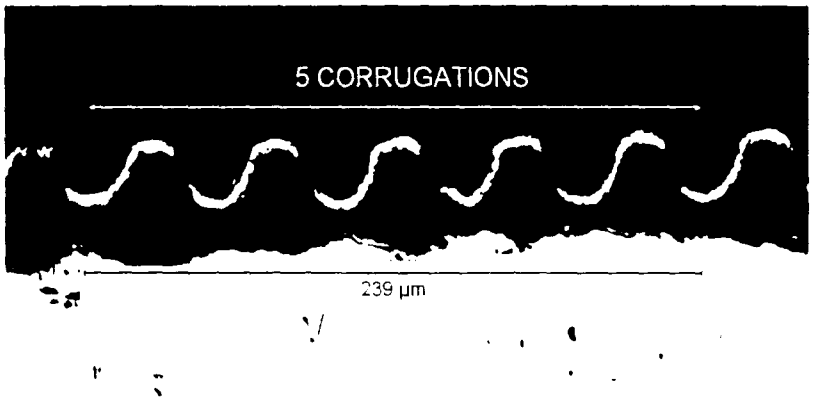

Figure 70 - Cross section of corrugated structure created by Heidelberg Instruments.

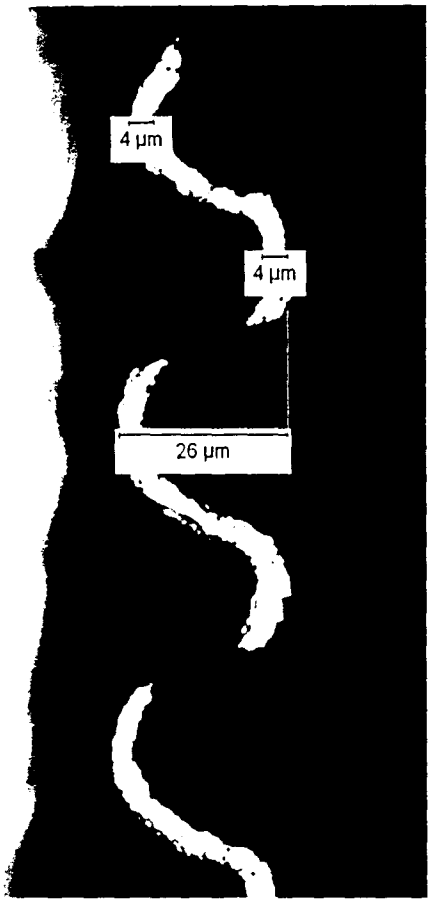

Figure 71 - Cross section of corrugated structure created by Heidelberg Instruments.

Examination of the Heidelberg substrates with a calibrated light optical microscope reveals that the structure has a pitch of 47.8um, a height of 26um, and uniform material thickness of 4um. Figure 70 and Figure 71 show breaks in the cross-section, but this is simply an artifact of metallographic sample preparation. The epoxy mount is smeared obscuring the metal hidden beneath it.

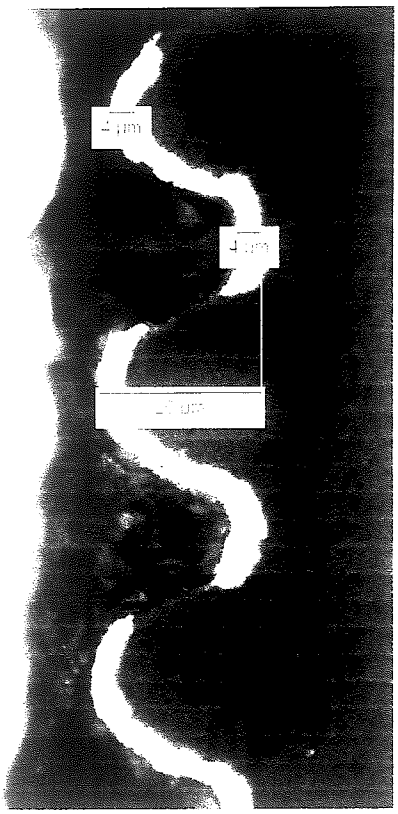

Figure 71 - Cross section of corrugated structure created by Heidelberg Instruments.

Examination of the Heidelberg substrates with a calibrated light optical microscope reveals that the structure has a pitch of 47.8um, a height of 26um, and uniform material thickness of 4um. Figure 70 and Figure 71 show breaks in the cross-section, but this is simply an artifact of metallographic sample preparation. The epoxy mount is smeared obscuring the metal hidden beneath it.

An SEM image of a sample from the same wafer gives a sense of variations in the topology along the axis of the corrugations. The grayscale exposure of the resist added a series of transverse "ridges" to the structure. Such features can be removed by adding an "extra pixel" to the CAD mask during the conversion process, which forces the laser to overwrite just a bit of the pattern, and adds uniformity to the exposure.

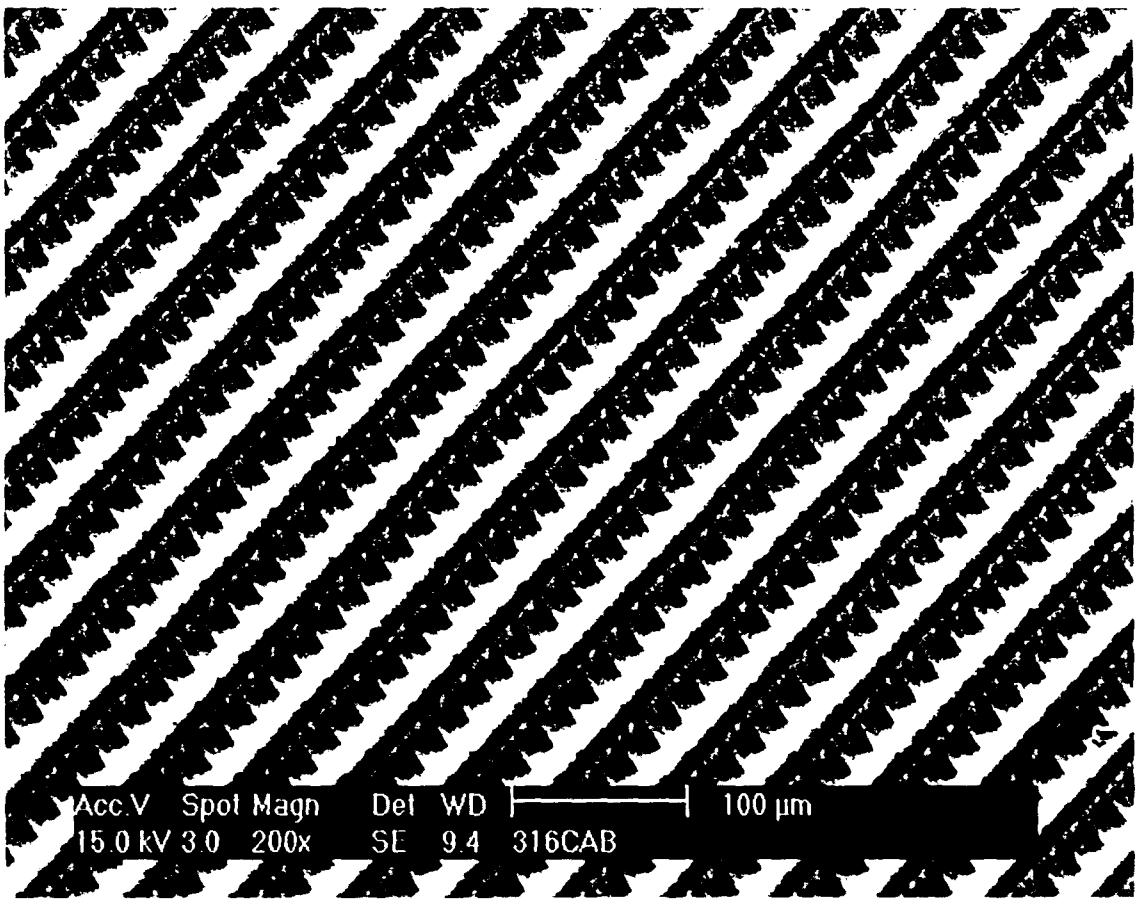

Figure 72 - SEM image of a Heidelberg sample

5.3 Testing results of corrugated thin film structures

It is necessary to establish the mechanical robustness of these corrugated structures to determine their potential to replace thick LIGA components. Although the corrugated structure is intended to be loaded along its length, a cantilever beam bend test should be less sensitive to mounting variations than a buckling load test[34]. Testing the corrugated structures as cantilever beams gives information about the area moment of inertia of the corrugated structures (the effect of shape upon the stiffness of the beam) which can then be used to predict buckling load behavior.

5.3.1 Design of testing apparatus

A mechanical testing apparatus was designed and fabricated in the machine shop in Whitaker Lab. The Solidworks CAD model of the testing fixture is shown below as Figure 73.

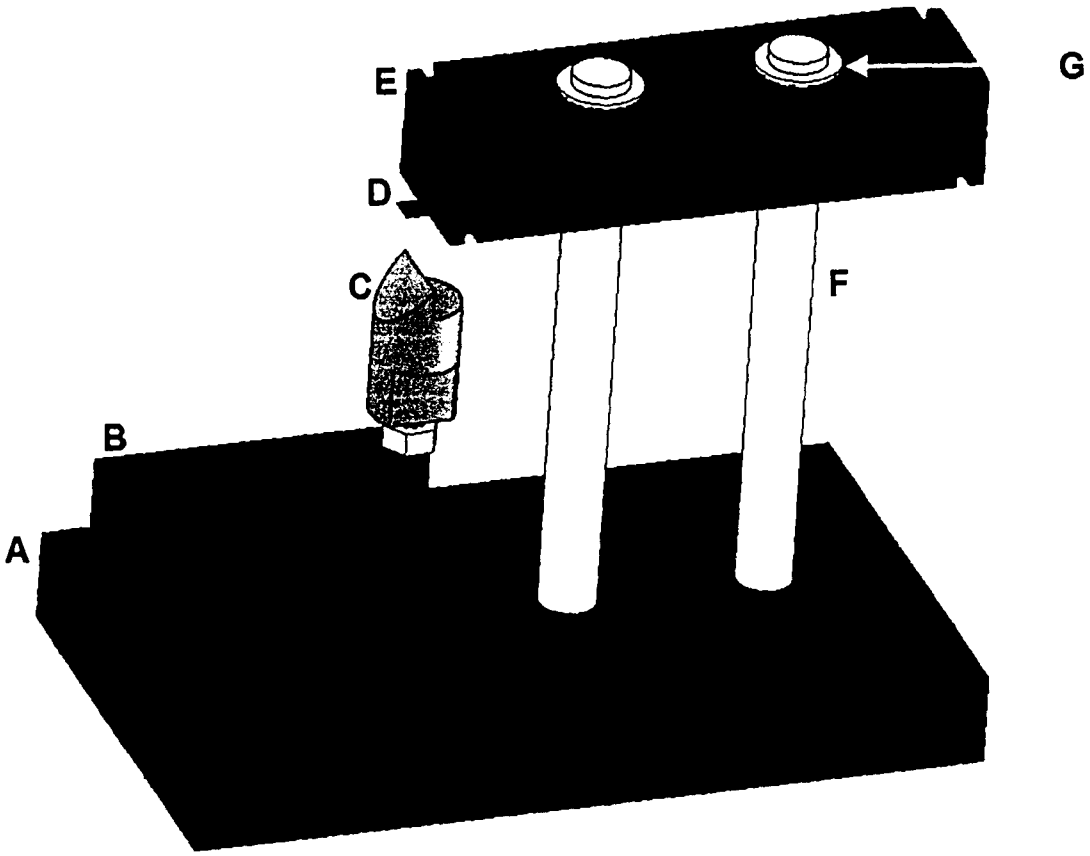

Figure 73 - CAD model of mechanical testing apparatus

The sample (D) is mounted to the testing beam (E) with paraffin wax. The aluminum testing beam moves up and down on steel dowel pins (F) and rides on top of compression springs (not shown). Bronze bushings (G) were added to the aluminum testing beam to minimize friction and guarantee locational accuracy of the testing beam from run to run. As the testing beam and sample are moved downwards on the dowel pins, the sample will touch the knife edged platen (C), which is attached to a 10 gram load cell (B), model GS0-10 from Transducer Techniques, Temecula, CA. The load cell and dowel pins are both mounted in an aluminum base plate (A). The micrometer head

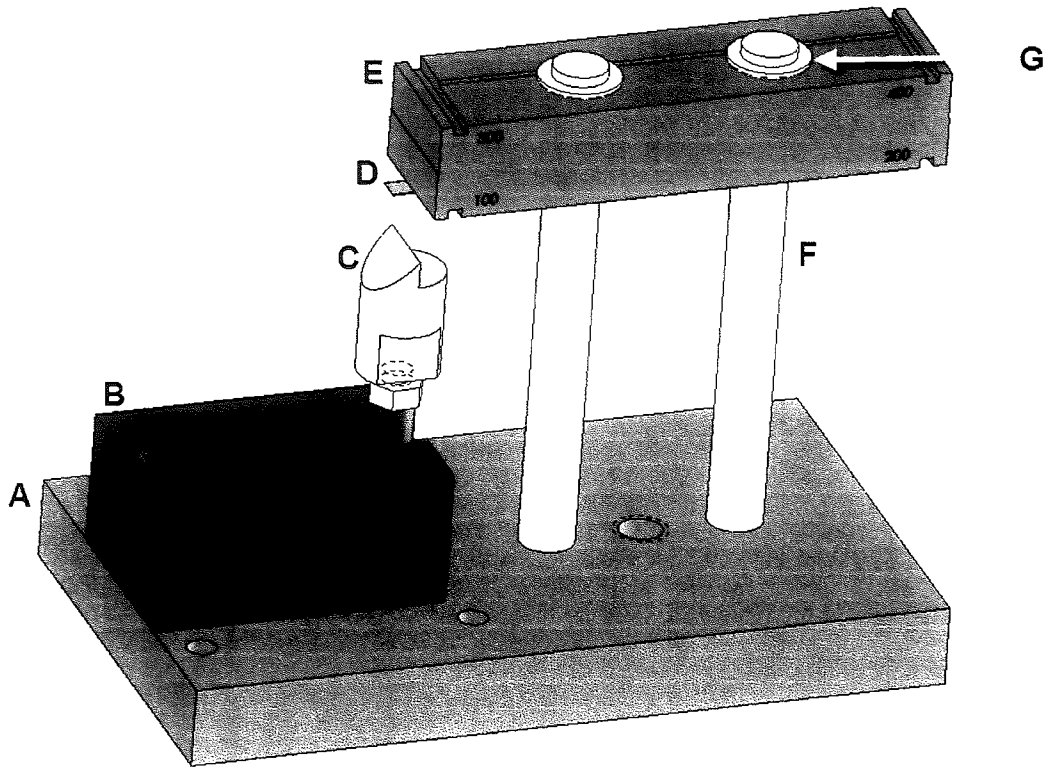

Figure 73 - CAD model of mechanical testing apparatus

The sample (D) is mounted to the testing beam (E) with paraffin wax. The aluminum testing beam moves up and down on steel dowel pins (F) and rides on top of compression springs (not shown). Bronze bushings (G) were added to the aluminum testing beam to minimize friction and guarantee locational accuracy of the testing beam from run to run. As the testing beam and sample are moved downwards on the dowel pins, the sample will touch the knife edged platen (C), which is attached to a 10 gram load cell (B), model GS0-10 from Transducer Techniques, Temecula, CA. The load cell and dowel pins are both mounted in an aluminum base plate (A). The micrometer head

that drives the testing beam is better seen in Figure 74, a photograph of the testing apparatus. This picture also shows the compression springs that hold the testing beam against the micrometer head. The micrometer head is manufactured by Mitutoyo, and features readings as low as 1um, a 2.5mm range and a non-rotating head.

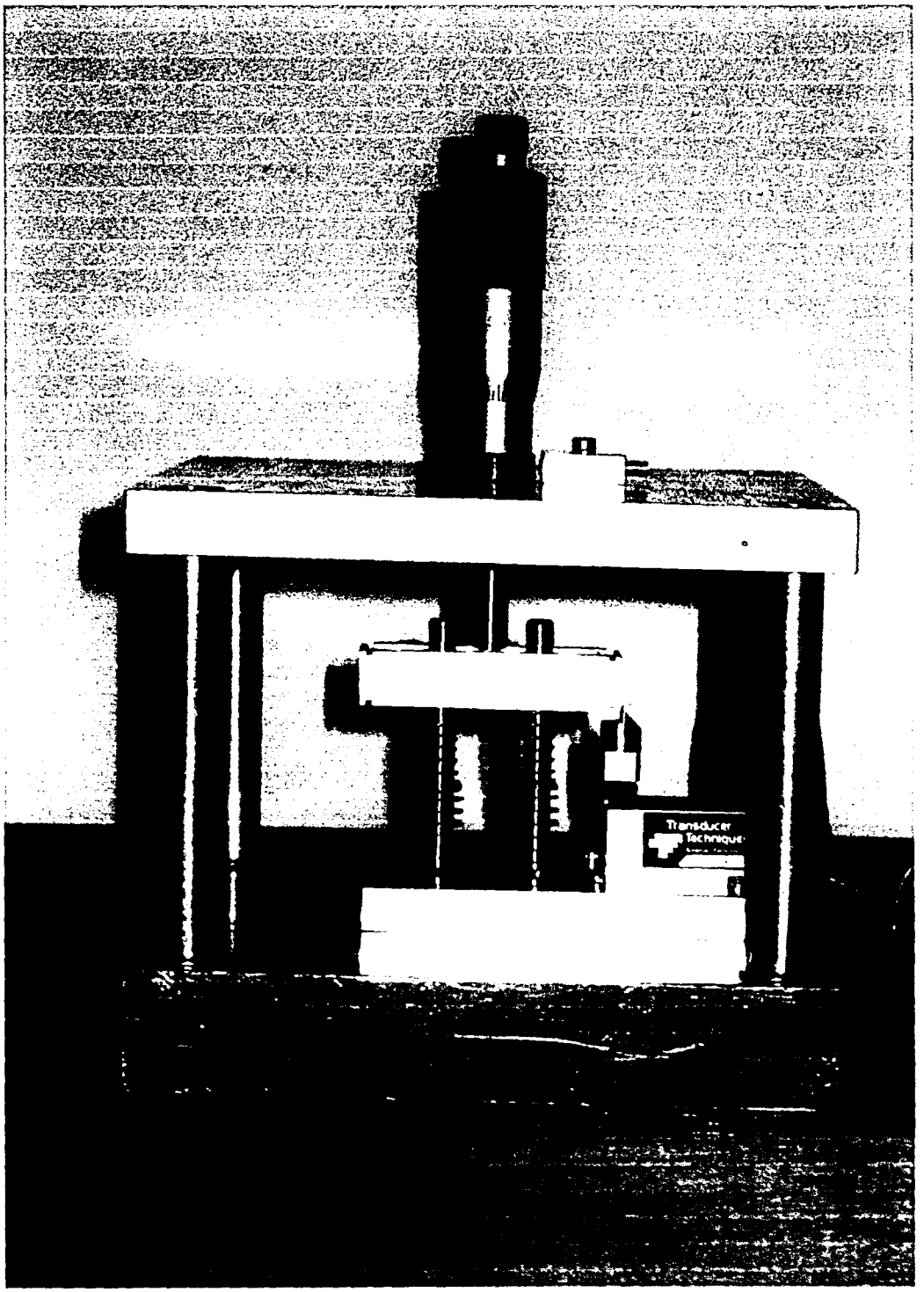

Figure 74 - Photograph of mechanical testing apparatus

The entire testing configuration is shown below as Figure 75. The output voltage from the load cell is sent through a TM0-2 signal conditioner, also manufactured by Transducer Techniques, and is ultimately read on a Fluke digital multimeter, model 8060 A. The calibration data and procedure for this experimental setup is included as Appendix A. Based on experimental data gathered in the course of this study, this setup can resolve loads as small as 20uN.

The length of the beam tested is determined by the experimental setup. The distance between the end of the movable beam and the load cell platen was found to be 400um as measured on a Nikon measuring microscope model MM-60.

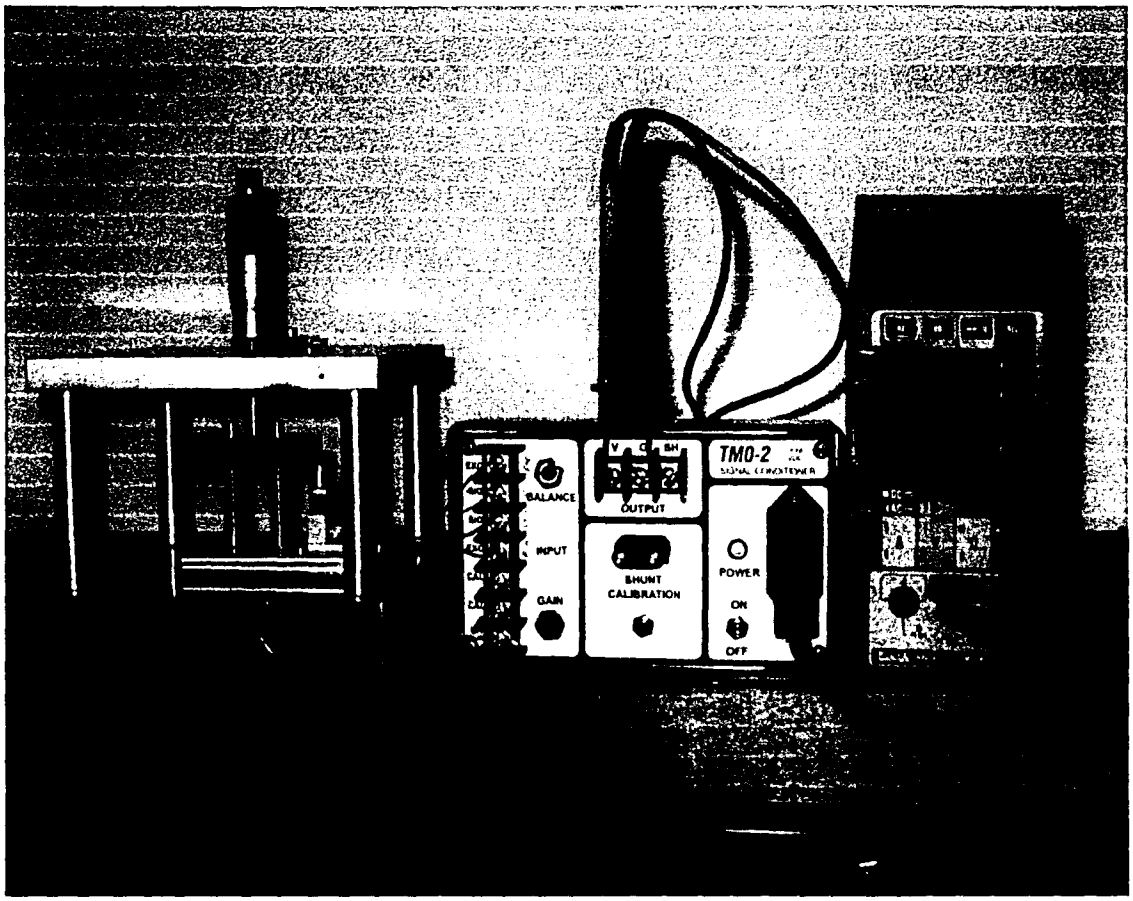

Figure 75 - Mechanical testing apparatus and meters

A closer view of a specimen under test is shown in Figure 76. In this picture the sample is the small dark parallelogram near the center of the picture. It is shown deflected by the knife edge of the platen.

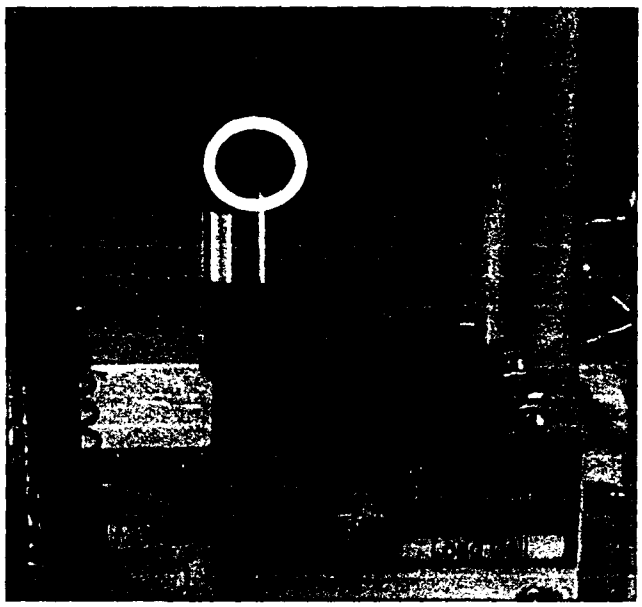

Figure 76 - Photo of a sample under test

5.3.2 Testing procedure

Data was collected as follows. After the specimen has been affixed to the testing beam with wax, and the testing beam assembled to the apparatus, the voltage at zero load was recorded in a spreadsheet. The micrometer is then adjusted in 25um increments, while the researcher monitors the output voltage for a change. The height of the micrometer in the reading before a change was noted is taken as the zero displacement point. The micrometer is then adjusted in 10um increments and the output voltage recorded into a spreadsheet after a 2 minute settling interval. The output voltage recorded can then be converted to a reading in grams using the calibration data for the load cell. The load in grams can be converted to a load in mN, and constructing a plot of displacement versus load is easily constructed. Such a plot is shown as Figure 77. This

plot is shown with axes of displacement versus load per unit width, as different specimens are different width due to the variety of metal deposition masks.

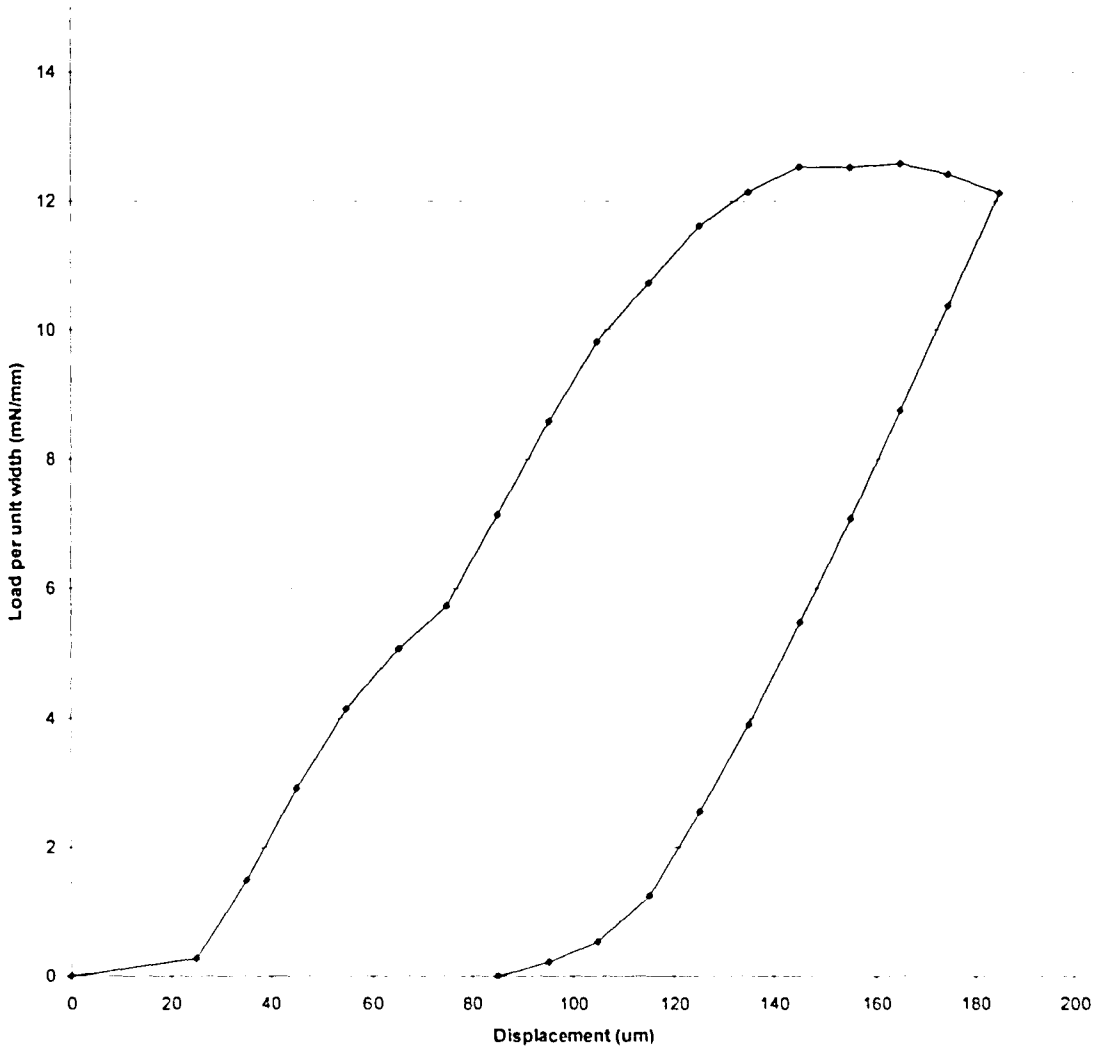

Figure 77 - Plot of Displacement vs. Load per unit width for Sample 5 on Wafer 4

The elastic response of the beam can be calculated from the linear sections of the load versus displacement plot. Using the voltage response from the load cell when under

no load, voltage response is zeroed. The calibration information from the load cell is used to convert the voltage signal to grams, which can then be readily converted to a load response in mN. Because the samples under test are of different width, the load is parameterized as a function of width. The sample width is measured on a Nikon measuring microscope, model MM-60. The load information is then used to calculate the area moment of inertia for the cantilever beam, using the formula[35]:

$$d = \frac{Pl^3}{3EI}$$

Where

d = Beam deflection

P = Load

l = Beam length

E = Elastic Modulus of Material

I = Cross-sectional Moment of Inertia

This equation is easily rearranged to solve for the moment of inertia.

$$I = \frac{l^3}{3E}\left(\frac{\Delta P}{\Delta d}\right)$$

Where $\frac{\Delta P}{\Delta d}$ is the slope of the load-displacement curve in the linear region during unloading.

The modulus of elasticity for copper has been obtained from reputable sources and is taken to be 130 GPa[36]. The load, deflection and beam length are directly measurable from the experimental apparatus as has been previously outlined.

These calculations have been placed into a spreadsheet, and the raw data is converted to modulus of elasticity automatically. The calculated elastic moduli in the linear regions of the curve are used to give an average response. These linear regions are shown in yellow in the example below.

Sample Name	Sample05	
Data taken	28-Mar-06	
Sample width	0.739	(mm)
Data interval after adjust	2.000	(minutes)
Beam Length	0.4000	(mm)
Modulus of Elasticity	130.0000	(GPa)
Calibration	9.2080	(grams / volt)
Zero Point	0.7000	(mm)
Average Moment of Inertia	2.38E-20	(m^4/mm)

Raw Data		Refined Data						
Dial Reading	Voltage Reading	Normalized Displacement	Zeroed Voltage Response	Zeroed Load Response	Zeroed Force Response	Force per unit width	Moment of Inertia	Moment of Inertia per unit width
2.500	0.4259	-1800	0.0000	0.00000	0.0000	0	-	-
1.000	0.4259	-300	0.0000	0.00000	0.0000	0	0	0
0.950	0.4259	-250	0.0000	0.00000	0.0000	0	0	0
0.900	0.4259	-200	0.0000	0.00000	0.0000	0	0	0
0.875	0.4259	-175	0.0000	0.00000	0.0000	0	0	0
0.850	0.4259	-150	0.0000	0.00000	0.0000	0	0	0
0.825	0.4259	-125	0.0000	0.00000	0.0000	0	0	0
0.800	0.4259	-100	0.0000	0.00000	0.0000	0	0	0
0.775	0.4259	-75	0.0000	0.00000	0.0000	0	0	0
0.750	0.4259	-50	0.0000	0.00000	0.0000	0	0	0
0.725	0.4259	-25	0.0000	0.00000	0.0000	0	0	0
0.700	0.4259	0	0.0000	0.00000	0.0000	0	0	0
0.675	0.4281	25	0.0022	0.02026	0.1985	0.268639	1.3E-21	1.76E-21
0.665	0.4381	35	0.0122	0.11234	1.1009	1.489727	1.48E-20	2E-20
0.655	0.4498	45	0.0239	0.22007	2.1567	2.9184	1.73E-20	2.34E-20
0.645	0.4598	55	0.0339	0.31215	3.0591	4.139488	1.48E-20	2E-20
0.635	0.4674	65	0.0415	0.38213	3.7449	5.067515	1.13E-20	1.52E-20
0.625	0.4728	75	0.0469	0.43186	4.2322	5.726903	8E-21	1.08E-20
0.615	0.4844	85	0.0585	0.53867	5.2789	7.143365	1.72E-20	2.32E-20
0.605	0.4963	95	0.0704	0.64824	6.3528	8.596459	1.76E-20	2.38E-20
0.595	0.5063	105	0.0804	0.74032	7.2552	9.817547	1.48E-20	2E-20
0.585	0.5138	115	0.0879	0.80938	7.9320	10.73336	1.11E-20	1.5E-20
0.575	0.5210	125	0.0951	0.87568	8.5817	11.61255	1.07E-20	1.44E-20
0.565	0.5254	135	0.0995	0.91620	8.9787	12.14983	6.52E-21	8.82E-21
0.555	0.5285	145	0.1026	0.94474	9.2585	12.52836	4.59E-21	6.21E-21
0.545	0.5285	155	0.1026	0.94474	9.2585	12.52836	0	0
0.535	0.5289	165	0.1030	0.94842	9.2946	12.57721	5.92E-22	8.02E-22
0.525	0.5276	175	0.1017	0.93645	9.1772	12.41846	-1.93E-21	-2.6E-21
0.515	0.5252	185	0.0993	0.91435	8.9607	12.1254	-3.55E-21	-4.81E-21
0.525	0.5109	175	0.0850	0.78268	7.6703	10.37925	2.12E-20	2.87E-20
0.535	0.4976	165	0.0717	0.66021	6.4701	8.755201	1.97E-20	2.67E-20
0.545	0.4839	155	0.0580	0.53406	5.2338	7.08231	2.03E-20	2.75E-20
0.555	0.4707	145	0.0448	0.41252	4.0427	5.470474	1.95E-20	2.65E-20
0.565	0.4578	135	0.0319	0.29374	2.8786	3.895271	1.91E-20	2.58E-20
0.575	0.4468	125	0.0209	0.19245	1.8860	2.552074	1.63E-20	2.2E-20
0.585	0.4361	115	0.0102	0.09392	0.9204	1.24551	1.58E-20	2.14E-20
0.595	0.4303	105	0.0044	0.04052	0.3970	0.537279	8.59E-21	1.16E-20
0.605	0.4277	95	0.0018	0.01657	0.1624	0.219796	3.85E-21	5.21E-21
0.615	0.4259	85	0.0000	0.00000	0.0000	0	2.67E-21	3.61E-21

These calculations have been placed into a spreadsheet, and the raw data is converted to modulus of elasticity automatically. The calculated elastic moduli in the linear regions of the curve are used to give an average response. These linear regions are shown in yellow in the example below.

Sample Name	Sample05	
Data taken	28-Mar-06	
Sample width	0 739	(mm)
Data interval after adjust	2 000	(minutes)
Beam Length	0 4000	(mm)
Modulus of Elasticity	130 0000	(GPa)
Calibration	9.2080	(grams / volt)
Zero Point	0 7000	(mm)
Average Moment of Inertia	2 38E-20	(m^4/mm)

Raw Data

Dial Reading (mm)	Voltage Reading (volts)
2.500	0.4259
1.000	0.4259
0.950	0.4259
0.900	0.4259
0.875	0.4259
0.850	0.4259
0.825	0.4259
0.800	0.4259
0.775	0.4259
0.750	0.4259
0.725	0.4259
0.700	0.4259
0.675	0.4281
0.665	0.4381
0.655	0.4498
0.645	0.4598
0.635	0.4674
0.625	0.4728
0.615	0.4844
0.605	0.4963
0.595	0.5063
0.585	0.5138
0.575	0.5210
0.565	0.5254
0.555	0.5285
0.545	0.5285
0.535	0.5289
0.525	0.5276
0.515	0.5252
0.525	0.5109
0.535	0.4976
0.545	0.4839
0.555	0.4707
0.565	0.4578
0.575	0.4468
0.585	0.4361
0.595	0.4303
0.605	0.4277
0.615	0.4259

Refined Data

Normalized Displacement (um)	Zeroed Voltage Response (volts)	Zeroed Load Response (g)	Zeroed Force Response (mN)	Force per unit width (mN/mm)	Moment of Inertia (m^4)	Moment of Inertia per unit width (m^4/mm)
-1800	0.0000	0.00000	0.0000	0	-	-
-300	0.0000	0.00000	0.0000	0	0	0
-250	0.0000	0.00000	0.0000	0	0	0
-200	0.0000	0.00000	0.0000	0	0	0
-175	0.0000	0.00000	0.0000	0	0	0
-150	0.0000	0.00000	0.0000	0	0	0
-125	0.0000	0.00000	0.0000	0	0	0
-100	0.0000	0.00000	0.0000	0	0	0
-75	0.0000	0.00000	0.0000	0	0	0
-50	0.0000	0.00000	0.0000	0	0	0
-25	0.0000	0.00000	0.0000	0	0	0
0	0.0000	0.00000	0.0000	0	0	0
25	0.0022	0.02026	0.1985	0.268639	1.3E-21	1.76E-21
35	0.0122	0.11234	1.1009	1.489727	1.48E-20	2E-20
45	0.0239	0.22007	2.1567	2.9184	1.73E-20	2.34E-20
55	0.0339	0.31215	3.0591	4.139488	1.48E-20	2E-20
65	0.0415	0.38213	3.7449	5.067515	1.13E-20	1.52E-20
75	0.0469	0.43186	4.2322	5.726903	8E-21	1.08E-20
85	0.0585	0.53867	5.2789	7.143365	1.72E-20	2.32E-20
95	0.0704	0.64824	6.3528	8.596459	1.76E-20	2.38E-20
105	0.0804	0.74032	7.2552	9.817547	1.48E-20	2E-20
115	0.0879	0.80938	7.9320	10.73336	1.11E-20	1.5E-20
125	0.0951	0.87568	8.5817	11.61255	1.07E-20	1.44E-20
135	0.0995	0.91620	8.9787	12.14983	6.52E-21	8.82E-21
145	0.1026	0.94474	9.2585	12.52836	4.59E-21	6.21E-21
155	0.1026	0.94474	9.2585	12.52836	0	0
165	0.1030	0.94842	9.2946	12.57721	5.92E-22	8.02E-22
175	0.1017	0.93645	9.1772	12.41846	-1.93E-21	-2.6E-21
185	0.0993	0.91435	8.9607	12.1254	-3.55E-21	-4.81E-21
175	0.0850	0.78268	7.6703	10.37925	2.12E-20	2.87E-20
165	0.0717	0.66021	6.4701	8.755201	1.97E-20	2.67E-20
155	0.0580	0.53406	5.2338	7.08231	2.03E-20	2.75E-20
145	0.0448	0.41252	4.0427	5.470474	1.95E-20	2.65E-20
135	0.0319	0.29374	2.8786	3.895271	1.91E-20	2.58E-20
125	0.0209	0.19245	1.8860	2.552074	1.63E-20	2.2E-20
115	0.0102	0.09392	0.9204	1.24551	1.58E-20	2.14E-20
105	0.0044	0.04052	0.3970	0.537279	8.59E-21	1.16E-20
95	0.0018	0.01657	0.1624	0.219796	3.85E-21	5.21E-21
85	0.0000	0.00000	0.0000	0	2.67E-21	3.61E-21

5.4 Results

Table 4 below shows the elastic modulus calculated for the samples tested. The wafers fabricated at Penn State are given arabic numeral identification, while Heidelberg assigned roman numerals to the wafers that were delivered to Lehigh University. All samples with the same wafer number were fabricated concurrently. Furthermore, the samples highlighted in Table 4 are related; they were deposited with copper in the same run and may be considered a head to head comparison of the two different structures. It is unclear how the film thicknesses can be different between the two wafers, since they were deposited simultaneously but the differences are readily apparent in the cross-section photographs (Figure 68 andFigure 71.) On wafer 5, two different film thicknesses were observed, as seen in Figure 68. The thickness of the metal film at the top plateau of the corrugation measured 5um, and the thickness at the bottom trough measured 8um. In Table 4, this is designated as "5 / 8".

Wafer	Sample No.	Moment of Inertia per unit width	Fabrication	Film Thickness	Corrugation Height	Corrugation pitch
(-)	(-)	(m^4/mm $x10^{-20}$)	(-)	(um)	(um)	(um)
4	3	2.17	PSU	4	18	91.6
4	5	2.38	PSU	4	18	91.6
4	6	2.99	PSU	4	18	91.6
5	1	0.08	PSU	5 / 8	16	95.4
5	2	0.21	PSU	5 / 8	16	95.4
5	3	0.17	PSU	5 / 8	16	95.4
IV	1	0.92	Heidelberg	4	26	47.8
IV	2	0.43	Heidelberg	4	26	47.8
IV	3	0.79	Heidelberg	4	26	47.8
IV	4	1.17	Heidelberg	4	26	47.8
IV	5	0.63	Heidelberg	4	26	47.8

Table 4 - Area moment of inertia for samples tested

5.4 Results

Table 4 below shows the elastic modulus calculated for the samples tested. The wafers fabricated at Penn State are given arabic numeral identification, while Heidelberg assigned roman numerals to the wafers that were delivered to Lehigh University. All samples with the same wafer number were fabricated concurrently. Furthermore, the samples highlighted in Table 4 are related; they were deposited with copper in the same run and may be considered a head to head comparison of the two different structures. It is unclear how the film thicknesses can be different between the two wafers, since they were deposited simultaneously but the differences are readily apparent in the cross-section photographs (Figure 68 andFigure 71.) On wafer 5, two different film thicknesses were observed, as seen in Figure 68. The thickness of the metal film at the top plateau of the corrugation measured 5um, and the thickness at the bottom trough measured 8um. In Table 4, this is designated as "5 / 8".

Wafer	Sample No.	Moment of Inertia per unit width	Fabrication	Film Thickness	Corrugation Height	Corrugation pitch
(-)	(-)	(m^4/mm x10^{-20})	(-)	(um)	(um)	(um)
4	3	2.17	PSU	4	18	91.6
4	5	2.38	PSU	4	18	91.6
4	6	2.99	PSU	4	18	91.6
5	1	0.08	PSU	5 / 8	16	95.4
5	2	0.21	PSU	5 / 8	16	95.4
5	3	0.17	PSU	5 / 8	16	95.4
IV	1	0.92	Heidelberg	4	26	47.8
IV	2	0.43	Heidelberg	4	26	47.8
IV	3	0.79	Heidelberg	4	26	47.8
IV	4	1.17	Heidelberg	4	26	47.8
IV	5	0.63	Heidelberg	4	26	47.8

Table 4 - Area moment of inertia for samples tested

5.5 Analysis and discussion

As expected the stiffness of these structures is still significantly lower than that of a LIGA-made IPMA beam. A common cross-section of such a beam as used in the IPMA is 75um wide x 75 um tall. Using the formula for the area moment of inertia, I, for a rectangular cross section[37], I = (base) (height)^3 / 12, the section stiffness will be 2.64 x 10^{-18} m^4. The difference in stiffness between this LIGA structure and a corrugated sample of 1mm unit width is at best two orders of magnitude.

However, the measured stiffness of some uncorrugated structures is unexpectedly lower than the theoretical stiffness of an un-corrugated flat film 4um tall and 1mm wide. The section stiffness of such a beam would be I = (base) (height)^3 / 12, or (1 x 10^{-3} m) (4 x 10^{-6} m)^3 / 12 , yielding 0.53 x 10^{-20} m^4. This calculated value is in the same range as the measured stiffness of the corrugated parts: 3.0 x 10^{-20} m^4/mm to 0.1 x 10^{-20} m^4/mm. It was not possible to test an uncorrugated thin film directly; the flat thin films exhibited a strong tendency to curl up when removed from their substrates and could not be successfully mounted to the testing apparatus.

Furthermore, closed form calculations used to calculate the stiffness of corrugated films[38] gives the stiffness of the Penn State and Heidelberg parts as 14.7 x 10^{-20} m^4/mm and 34.3 x 10^{-20} m^4/mm respectively. These calculated area moments of inertia are about one order of magnitude greater than measured values reported in Table 4. The large

discrepancy between measured and theoretical data merited a closer look at the testing methodology.

Samples of known cross-sectional shape were tested and compared with theory. Cantilever beam tests of 50um diameter wires of Au, Ag and Ni, as well as 125um diameter fibers of fused silica yielded interesting results. The metal wires consistently yielded an area moment of inertia of approximately 3 times lower than the theoretical area moment of inertia. For the silica fiber the measured area moment of inertia for the silica fiber was approximately 5 times lower than the theoretical.

The large discrepancy between the measured data and the theoretical values for both corrugated structures and fibers of known cross sectional shape indicate that cantilever beam bend testing does not give accurate results. It is suspected that the mounting of the cantilever specimens is critical. If too much paraffin was used to mount corrugated samples, the paraffin had a strong tendency to wick, filling in the corrugations and artificially stiffening the structures. Samples exhibiting any paraffin wicking in the cantilevered section were discarded from the study.

To prevent wicking problems, a very small amount of paraffin was used to hold samples to the testing apparatus. It is possible that the stiffness of the paraffin mount was low enough to influence the testing results.

Attempts to replace the paraffin mounting technique with an epoxy based mounting method were unsuccessful. The epoxy had a strong tendency to form a 100-200um meniscus at the base of the tested sample, dramatically increasing the stiffness of the sample. This data was also discarded from the study.

It is worth noting that if the measured data for the corrugated structures is off by the same amount as the metal wire and glass fiber data, then the experimental results are in the same order of magnitude as the closed form solution.

The correction factor suggested by the wire and fiber data is 3x to 5x that of the measured data. Stiffness in the range of $2.5x10^{-20}$ m^4/mm was measured for the parts from wafer 4 (fabricated at Penn State), multiplying these values by a factor of four yields $10.0x10^{-20}$ m^4/mm which is in the same order of magnitude as the 14.7×10^{-20} m^4/mm value given by the closed form solution. This is not to imply that this particular 3x to 5x correction factor is required to interpret the experimental data. The correlation between a wire and a plate is not necessarily the same. The salient point is that the correction takes the data in the proper direction.

Chapter 6
Conclusions, Suggestions for Further Research and References Cited

6.1 Summary

In this work, a characterization of the force and displacement capabilities of the IPMA has been presented, along with a sequence of steps to reproduce this device. The device operating limits have been identified and the capabilities of the IPMA have been found to exceed other similar MEMS-based devices used to perform optical alignments. Several potential improvements to the device have been identified. Substantial progress has been made in developing one of the suggested improvements: replacement of the LIGA structural elements with corrugated thin films.

The first steps in characterizing corrugated thin film structures have been completed. Visually the structures appear robust, but testing data does not correlate well with predictions from theory. Results from testing metal and glass fibers of known cross-section, indicate that the measured data is three to five times lower than the section stiffness predicted by theory.

6.2 Suggestions for further research

There are two critical areas for further development of these devices: one in testing and one in design. It is clear that the method for mounting and testing corrugated

structures requires revision. A three-point or four-point bend test will eliminate the need for a paraffin mount and any associated errors.

Further development efforts should be made to add linerboards to these corrugated structures. Linerboards are flat horizontal boards that tie the corrugations together from above and below. The presence of linerboards is known to significantly increase the stiffness of corrugated structures, and is needed to prove their merit as structural elements in MEMS applications.

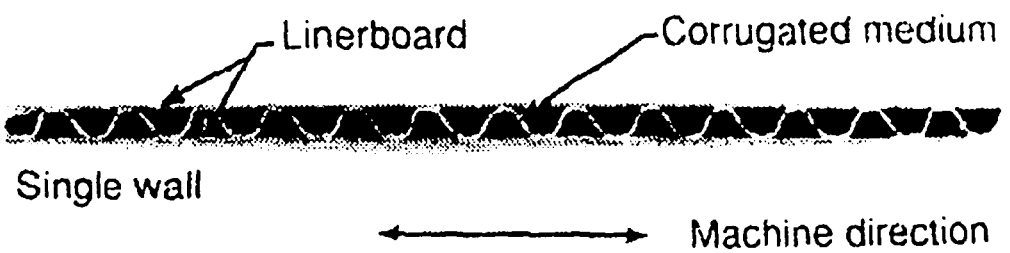

Figure 78 – Linerboards

A process sequence for creating corrugated structures with linerboards is presented below as Figure 79. A planar layer of resist is first deposited on a silicon wafer, followed by a metal deposition, creating the bottom linerboard. On top of the metal, a thick layer of resist is added and then exposed to a grayscale source. This resist is then uniformly etched to expose the underlying metal in what will be the valleys of the corrugations. Metal deposition follows, creating corrugated structures. A final layer of

resist is spun on the wafer, and hard baked. This top layer of resist is then polished to reveal the metal on the tops of the corrugations. A final metal deposition creates the top linerboard. Finally the entire wafer is soaked in solvent, dissolving the resist and freeing the corrugated section for testing.

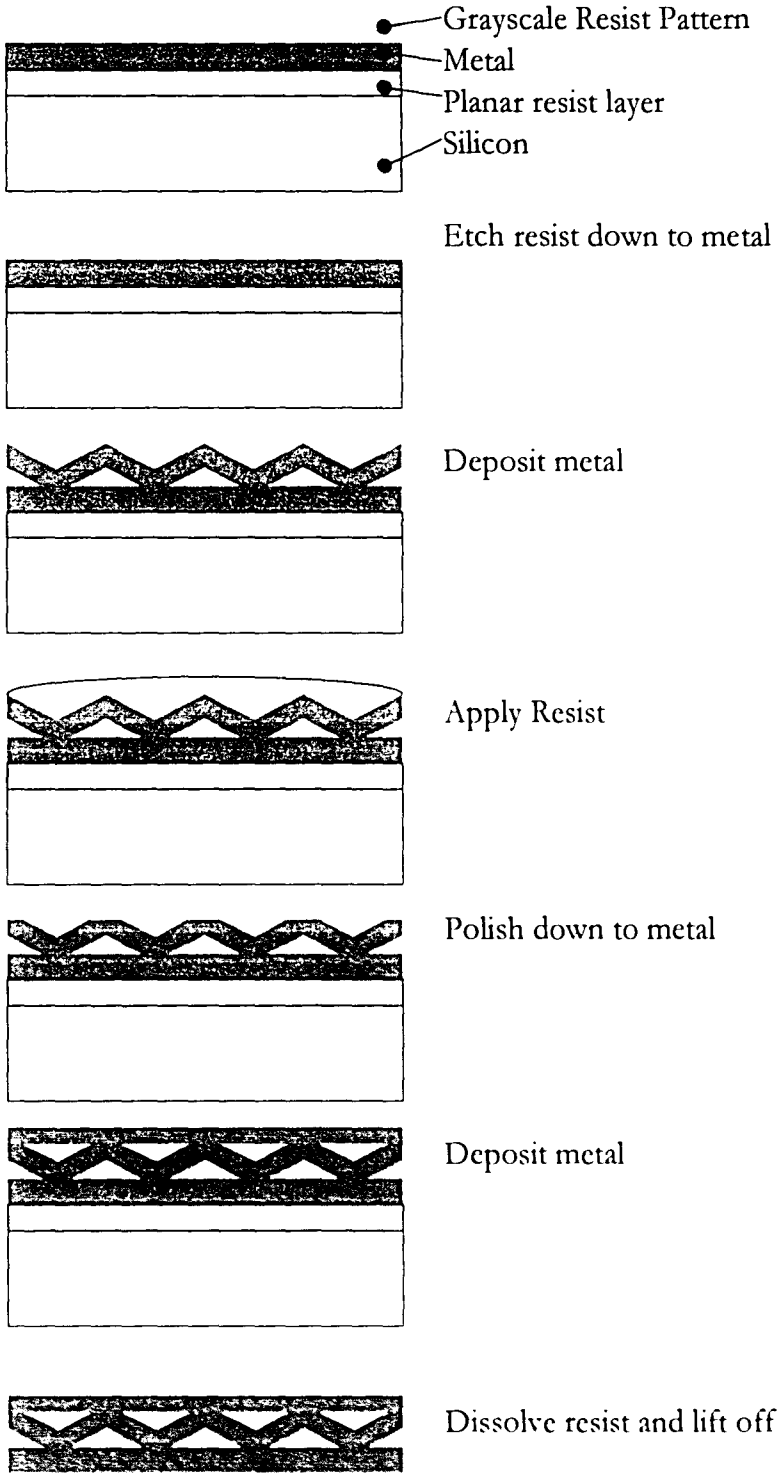

Figure 79 - Process sequence for linerboards

6.3 References Cited

[1] Issacson, Benjamin Franklin: an American life, Simon & Schuster, New York. 2003.

[2] Kulicke and Soffa Maxμm ultra wirebonding machine specifications. http://www.kns.com/pdfs/Maxum_ultra.pdf (accessed 10 Feb. 2006)

[3] http://www.kns.com/Templates/ShowPage.asp?TMID=108&FID=123&PID=4944 (accessed 10 Feb. 2006)

[4] Joyce and DeLoach, "Alignment of Gaussian Beams", Applied Optics, vol. **23,** p 4187, 1984

[5] Fischer, Zech and Peters," A Reusable Fiber-Chip Coupling Method for Optical-Communication Transmitter Modules," TechOnLine Publication Date: Jan. 25, 2002

[6] He, Yuan, Ngo, Bu, and Tao," Low-cost and efficient coupling technique using reflowed sol-gel microlens," *Optics Express*, vol. **14**, p 1621-1627, 2003.

[7] Hockaday, "Method and Apparatus for positioning an optical fiber," Patent US 5 080 458, 1992.

[8] Jebens, et. al., "Microactuators for aligning optical fiber," Sensors *and Actuators A: Physical,* vol. **20**, p 65-73. 1989.

[9] Kikuya, et. al., "Alignment of optical axes by using electrostatic force," *Optics Letters*, vol. **18**, no. 11, p 864, 1993

[10] Kikuya et. al., "Micro alignment machine for optical coupling," in *Proceedings. IEEE. Micro Electro Mechanical Systems. An Investigation of Micro Structures, Sensors, Actuators, Machines and Systems.* Fort Lauderdale, FL, USA: IEEE, 1993, p 36.

[11] Nagoka, "Fabrication of micro-pipes and their applications to single-mode fiber switching and splicing," *IEICE transactions on Electronics,* vol. **E80-C**. no. 2, p 280, 1997.

[12] Gerlach et. al., "Automatic adjustment of monomode optical waveguides by a microsystem," *Journal of Micromechanics and Microengineering,* vol. 7. no. 3, p 227, 1997.

[13] Haake, Wood, et. al., "Microsystems for three axis active fiber alignment," in *1998 IEEE/LEOS Summer Topical Meeting. Digest. Broadband Optical Networks and Technologies: An emerging reality. Optical MEMS. Smart Pixels. Organic Optics and Optoelectronics.* Monterey, CA: IEEE, 1998, p 53-6.

[14] Haake et. al., "Microactuator for precisely aligning an optical fiber and an associated fabrication method," Patent US 5 870 518, 1997.

[15] Syms, et. al., "Scalable electrothermal MEMS actuator for optical fibre alignment," *Journal of Micromechanics and Microengineering,* vol. **14**, no. 12, p 1633, 2004.

[16] Field, et. al., "Micromachined 1 x 2 optical fiber switch," Sensors and Actuators, A: Physical, vol. **53**, no. 1-3, p 311, 1996.

[17] Kopka, et. al., "Coupled U-Shaped cantilever actuators for 1*4 and 2*2 optical fibre switches," *Journal of Micromechanics and Microengineering 10th Micromechanics Europe Workshop (MME'99), 27-28 Sept. 1999*, vol. **10**, no. 2, p 260-4, 2000.

[18] Jebens, et. al., "Microactuators for aligning optical fiber," *Sensors and Actuators A (Physical),* vol. **18**, no. 11, p 864, 1993.

[19] Gerlach, et. al., "Automatic adjustment of monomode optical waveguides by a microsystem," *Journal of Micromechanics and Microengineering,* vol. **7**, no. 3, p 227, 1997.

[20] Kim, et. al., "Integration of a microlens on a micro XY-stage," *Proceedings of the SPIE – The International Society for Optical Engineering*, vol. **3892**, p 109, 1999.

[21] Fan, et. al., "Self-assembled microactuated XYZ stages for optical scanning and alignment," in *Digest of Technical Papers, Transducers 97. 1997 International Conference on Solid State Sensors and Actuators,* vol. **1**. Chicago, IL: IEEE, 1997. p 319-22.

[22] Fan, et. al., "MEMS actuators and micropositioners for integrated micro-optics," *Proceedings of the SPIE – The International Society for Optical Engineering,* vol. **3289**, p 152, 1998.

[23] Grade, et. al., "Advanced, vibration resistant comb-drive actuators for use in a tunable laser source," *Sensors and Actuators A: Physical,* vol. **114**, no. 2-3, p 413, 2004.

[24] Lin, et. al., "Microactuated micro-XYZ stages for free space micro-optical bench," in *Proceedings IEEE. The Tenth Annual International Workshop on Micro Electro Mechanical Systems. An Investigation of Micro Structures, Sensors, Actuators, Machines and Robots.* Nagoya, Japan: IEEE, 1997. p 43.

[25] Ishikawa, et. al.,"An integrated micro-optical system for VCSEL-to-fiber active alignment," *Sensors and Actuators, A: Physical,* vol. **103**, no 1-2, p 109-15, 2003.

[26] Solgaard, et. al., "Optoelectronic packaging using silicon surface-micromachined alignment mirrors," *IEEE Photonics Technology Letters,* vol. 7, no. 1, p41, 1995.

[27] Zhang, et. al., "Thermal based angle fixing for micromirrors," in *Transducers '03. 12th International Conference on Solid-State Sensors, Actuators and Microsystems. Digest of Technical Papers,* vol. **2**. Boston, MA: IEEE, 2003, p 1470.

[28] Syms, et. al., "Robust latching MEMS translation stages for micro-optical systems," *Journal of Micromechanics and Microengineering,* vol. **14**, no. 5, p 667, 2004.

[29] Haasl, "Assembly of Microsystems for Optical and Fluidic Applications," Ph. D. dissertation, Royal Institute of Technology (KTH), Stockholm, Sweden. 2005. (With additional data to "Table 1 - Overview of MEMS optical alignment technologies" by J. T. Iceman, this work.)

[30] Haake, Wood and Dhuler, *SPIE Proceedings*, vol. **20**, p 3276, 1998.

[31] Personal correspondence between the author and the MEMS exchange of Reston, VA. 2005.

[32] Weisong Wang, W. L. Brown. Unpublished work.

[33] Helton, "Laser Direct Write Grayscale Photolithography," *2005 NNIN REU Research Acccomplishments,* Cornell University, p 46, 2005.

[34] H. Neid, Lehigh University, personal communication.

[35] Norton, Design of Machinery: An Introduction to the Synthesis and Analysis of Mechanisms and Machines 2nd Ed'n, McGraw-Hill, New York, New York, 1992.

[36] http://www.wikipedia.com accessed 15 March, 2006.

[37] Ashby, Materials Selection in Mechanical Design, Pergamon Press, Oxford, England. 1993.

[38] Mehmet Sahin, Murat Ozturk and Herman Nied, Lehigh University. Unpublished work.

Appendix A
Load Cell Calibration

The load cell used to measure the deflection of the corrugated thin films was calibrated using the calibration data from the manufacturer and a known load. The procedure follows.

First the output from the Transducer Techniques TM0-2 signal conditioner was balanced to read zero volts as measured with a Fluke Model 8060A multimeter with no load on the Transducer Techniques GS0-10 load cell. This was accomplished by adjusting the balance screw on the face of the signal conditioner until 0.000 volts was displayed on the multimeter. Jumper wires were then attached across the signal conditioner to activate the calibration circuit, as described in the operation manual.

The fixturing for the deflection measurement was used as the known load. Using an OHAUS Model AR0640 scale, the mass of the fixturing was established to be 4.9015 grams. This load was then attached to the load cell, and the output voltage changed with the gain adjustment screw until the reading on the multimeter was in agreement with the calibration data. A sample calculation is shown below.

Calibration data: 0.5430 volts at a 5.000 gram load, and 1.0861 volts at a 10 gram load. Based on a linear interpolation, the voltage response off the signal conditioner for the 4.0915 gram load of the fixturing should be 0.4443 volts. The gain adjustment screw was turned until this voltage was achieved.

Calibration information and procedures from the manufacturer and are included below in Figures 80 through 83.

Transducer Techniques®
Order Online !

Tech Support
(800) 344-3965
(951) 719-3965
Fax (951) 719-3900
E-mail: ttu@ttloadcells.com

CERTIFICATE OF CALIBRATION

SERIAL NUMBER	186240	DATE OF CALIBRATION	02/10/2006
SENSOR MODEL	GS0-10	DATE OF RECALIBRATION	02/10/2007
JOB NUMBER	51070		
TECHNICIAN	RDM		

COMPRESSION LOAD GRAMS	MV/V INC	MV/V DEC
0	0.0000	0.0000
5	0.5430	0.5434
10	1.0861	

NON-LINEARITY	0.00	PCT FS
NON-REPEATABILITY	-0.05	PCT FS
HYSTERESIS	0.04	PCT FS

SHUNT CALIBRATION

PCT LOAD	LOAD GRAMS	SIGNAL MV/V	SHUNT K OHMS	SHUNT PINS
46.50	4.65	0.5051	174.825	(-E -S)
93.00	9.30	1.0101	87.325	(-E -S)

DPM-2 SCALE FACTOR 0.0028

CALIBRATION COMPUTED FROM THREE (3) RUNS INCREASING AND DECREASING
TRACEABLE TO NIST TEST # 185302
CALIBRATION PERFORMED AT 10 VDC
MAXIMUM BRIDGE EXCITATION 12 VDC

WIRING		
PIN	COLOR	CODE
N/A	RED	+EXCITATION
N/A	BLK	-EXCITATION
N/A	GRN	+SIGNAL
N/A	WHT	-SIGNAL
N/A	SHD	GROUND

42420 Rio Nedo, Temecula, CA 92590 (951) 719-3965 Fax (951) 719-3977
URL http://www.ttloadcells.com E-mail ttu@ttloadcells.com

Figure 80 - Certificate of Calibration for GS0-10 Load Cell

TM0-2

STAND ALONE / BENCH TOP
AMPLIFIER / CONDITIONER MODULE

OPERATORS MANUAL

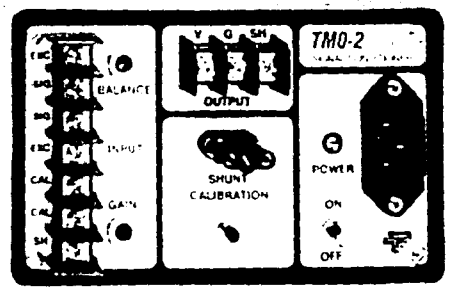

Transducer Techniques

42492 RIO NEDO TEMECULA CA 92590
(909) 719-0935 FAX (909) 719-0930
URL http://www.tmtechnologies.com
E-mail: tt@tmtechnologies.com

Figure 81 - Signal Conditioner

SET UP PROCEDURES

CAUTION: Before proceeding with the Set Up unplug the unit and make sure that output terminals V and G or SH are not shorted. Permanent damage to the unit can result when output is shorted to ground.

METHOD 1: Shunt calibration with TTI transducers.

1. Connect transducer to input terminal block. For 6 wire transducer refer to fig.2 and for 4 wire transducer refer to fig.3. The following table can also be useful.

6 WIRE TRANSDUCER	TM-2	4 WIRE TRANSDUCER	TM-2
RED	EXC	RED	EXC
WHITE	-SIG	WHITE	-SIG
GREEN	SIG	GREEN	SIG
BLACK	-EXC	BLACK	-EXC
BLUE	CAL	SHIELD	SH
BROWN	CAL		
SHIELD	SH		

2. Connect a digital voltmeter to output terminals V and G, positive probe to V. (Set meter's range to 20 VDC or less, according to the number of counts needed for the application. For instance, if a load cell is used to weigh a 1000 pounds object, the most convenient range is 2.000 VDC for a 4.5 digit voltmeter, knowing that TM-2 module has a maximum 10 VDC output.).

3. Turn power switch off. Plug power cord to the unit and to a 115 VAC, 50 to 400 Hz power outlet. Turn power on and verify via power lamp. Allow 15 minute warm up

4. Adjust balance potentiometer until the voltmeter displays zero (or close to zero for more than 4 digits).

5. Refer to the sample certificate of calibration, fig.1, example1 (typical to certificates of calibration supplied with TTI transducers). Multiply the percentage of load value (PCT LOAD) for a 87.325 kohm resistor by the desired full scale voltage output. Note that 10 VDC is the maximum output voltage for a 2 mV/V transducer.

   Example: 10 VDC x 50.2 % = 5.02 VDC.

2

Figure 82 - Calibration Procedure

Method 2: Using a Known load (Dead Weight Calibration).

1. Follow METHOD1, steps 1 through 4.
2. Apply a known load (Dead Weight) to the transducer.
3. Adjust the gain potentiometer to display engineering unit equivalent to known load (Dead Weight).
4. Remove known load (Dead Weight) and readjust balance potentiometer, if necessary.
5. The TM-2 is Calibrated and ready to be used.

Fig. 2

[4 Wire Config.]

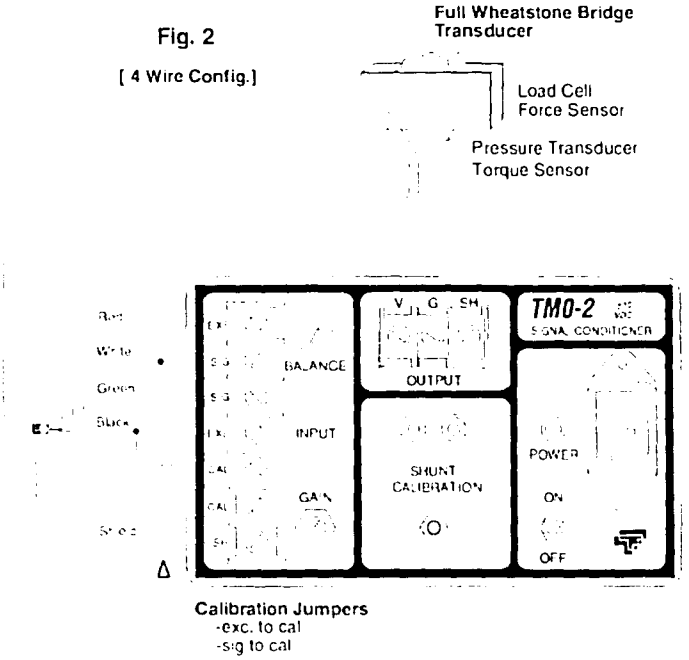

4

Figure 83 - Calibration Procedure (cont.)

Vita

Jason Todd Iceman was born April 27, 1973. He holds a Bachelor of Mechanical Engineering Degree from the University of Delaware, 1995. He is a veteran design engineer with over ten years of experience in research, manufacturing, and product design and development in both domestic and international locations. Mr. Iceman's past employers include AMP Incorporated, Lucent Technologies, T-Networks, Inc. He has been a technology consultant for several early stage start ups. Mr. Iceman holds one patent, with several patents pending.

He will obtain his Master of Science in Material Science and Engineering degree from Lehigh University in May of 2006. He has accepted a position as the Senior Mechanical Engineer for GlucoLight Corp. of Bethlehem PA, where he will endeavor to create the first non-invasive glucose monitor.

END OF
TITLE